

Simultaneous Measurement of Oscillation Parameters in Beam and Atmospheric Neutrino Data from Tokai-to-Kamioka and Super-Kamiokande Experiments

Daniel Robert Clement Barrow

Magdalen College,
Oxford University

¹⁰ A Dissertation Submitted to Oxford University

¹¹ for the Degree of Doctor of Philosophy

¹²

13 **Simultaneous Measurement of**

14 **Oscillation Parameters in Beam and**

15 **Atmospheric Neutrino Data from**

16 **Tokai-to-Kamioka and**

17 **Super-Kamiokande Experiments**

18 *Abstract*

19 Lorem ipsum dolor sit amet, consectetur adipiscing elit, sed do eiusmod tempor incididunt ut labore et dolore magna aliqua. Nulla aliquet porttitor lacus luctus accumsan tortor posuere. Pulvinar neque laoreet suspendisse interdum. Sem viverra aliquet eget sit. Nunc sed velit dignissim sodales ut eu sem integer vitae. At erat pellentesque adipiscing commodo elit at imperdiet dui accumsan. Fames ac turpis egestas integer eget aliquet nibh. Scelerisque eu ultrices vitae auctor eu augue. Purus non enim praesent elementum facilisis leo vel. Sollicitudin nibh sit amet commodo. Vitae auctor eu augue ut. Vel quam elementum pulvinar etiam. A condimentum vitae sapien pellentesque habitant morbi tristique senectus. Viverra accumsan in nisl nisi scelerisque eu ultrices. Sed viverra ipsum nunc aliquet bibendum enim. Sit amet purus gravida quis. In vitae turpis massa

³² sed elementum tempus egestas sed sed. Vivamus arcu felis bibendum
³³ ut tristique et egestas. Senectus et netus et malesuada fames ac turpis.
³⁴ Ac auctor augue mauris augue.

35 Declaration

36 This dissertation is the result of my own work, except where ex-
37 plicit reference is made to the work of others, and has not been sub-
38 mitted for another qualification to this or any other university. This
39 dissertation does not exceed the word limit for the respective Degree
40 Committee.

41 Daniel Robert Clement Barrow

42 ©The copyright of this thesis rests with the author and is made available under a Creative
43 Commons Attribution Non-Commercial No Derivatives licence. Researchers are free to copy,
44 distribute or transmit the thesis on the condition that they attribute it, that they do not use
45 it for commercial purposes and that they do not alter, transform or build upon it. For any
46 reuse or redistribution, researchers must make clear to others the licence terms of this work.

47

Acknowledgements

48 at pretium nibh ipsum. Eget nunc scelerisque viverra mauris in aliquam. Arcu vitae
49 elementum curabitur vitae nunc sed velit dignissim. Sed arcu non odio euismod lacinia
50 at quis risus sed. Vitae tempus quam pellentesque nec nam aliquam sem et tortor.
51 Viverra aliquet eget sit amet tellus cras adipiscing. Purus sit amet luctus venenatis
52 lectus magna. In aliquam sem fringilla ut morbi tincidunt augue. Fermentum dui
53 faucibus in ornare. Aliquam malesuada bibendum arcu vitae elementum curabitur
54 vitae nunc sed.

55 Ultricies leo integer malesuada nunc vel risus commodo. Tellus cras adipiscing
56 enim eu turpis egestas pretium. Dictumst quisque sagittis purus sit amet volutpat
57 consequat mauris nunc. Vitae congue mauris rhoncus aenean vel elit scelerisque
58 mauris pellentesque. Vel facilisis volutpat est velit egestas dui id ornare. Suscipit
59 adipiscing bibendum est ultricies. At in tellus integer feugiat scelerisque varius
60 morbi enim. Cras semper auctor neque vitae tempus. Commodo sed egestas egestas
61 fringilla phasellus faucibus. Cras pulvinar mattis nunc sed blandit. Pretium viverra
62 suspendisse potenti nullam ac tortor vitae. Purus sit amet volutpat consequat. Orci
63 sagittis eu volutpat odio facilisis mauris. Sit amet massa vitae tortor condimentum
64 lacinia quis. Commodo sed egestas egestas fringilla phasellus. Sed libero enim sed
65 faucibus turpis. Vitae tempus quam pellentesque nec.

66 Blandit massa enim nec dui. Viverra tellus in hac habitasse platea dictumst vestibulu-
67 lum. Bibendum enim facilisis gravida neque convallis. Sagittis nisl rhoncus mattis
68 rhoncus urna neque. Nisl rhoncus mattis rhoncus urna neque. Ac tortor vitae purus
69 faucibus ornare. Aenean sed adipiscing diam donec adipiscing tristique risus. Sapien
70 nec sagittis aliquam malesuada bibendum. Et leo duis ut diam quam nulla. Tellus
71 rutrum tellus pellentesque eu tincidunt tortor aliquam nulla facilisi. Fermentum leo

⁷² vel orci porta non pulvinar neque. Eget sit amet tellus cras adipiscing enim eu. Sed
⁷³ viverra tellus in hac habitasse platea dictumst vestibulum.

⁷⁴ Sit amet consectetur adipiscing elit. At varius vel pharetra vel turpis nunc eget
⁷⁵ lorem. Elit scelerisque mauris pellentesque pulvinar pellentesque habitant morbi
⁷⁶ tristique senectus. Odio euismod lacinia at quis risus sed vulputate odio. Vitae suscipit
⁷⁷ tellus mauris a diam maecenas sed enim ut. Dignissim convallis aenean et tortor at
⁷⁸ risus viverra. Diam sollicitudin tempor id eu. Erat velit scelerisque in dictum. Blandit
⁷⁹ cursus risus at ultrices. Ac tortor vitae purus faucibus ornare suspendisse sed.

Contents

1	Introduction	1
2	Neutrino Oscillation Physics	2
2.1	Discovery of Neutrinos	3
2.2	Theory of Neutrino Oscillation	4
2.2.1	Three Flavour Oscillations	5
2.2.2	The MSW Effect	9
2.3	Neutrino Oscillation Measurements	10
2.3.1	Solar Neutrinos	10
2.3.2	Atmospheric Neutrinos	13
2.3.3	Accelerator Neutrinos	16
2.3.4	Reactor Neutrinos	19
2.4	Summary	21
3	T2K and SK Experiment Overview	24
3.1	The Super-Kamiokande Experiment	25
3.1.1	The SK Detector	26
3.1.2	Calibration	29
3.1.3	Data Acquisition and Triggering	33
3.1.4	Cherenkov Radiation	35
3.2	The Tokai to Kamioka Experiment	36
3.2.1	The Neutrino Beam	38
3.2.2	The Near Detector at 280m	42
3.2.2.1	Fine Grained Detectors	44
3.2.2.2	Time Projection Chambers	46

104	3.2.2.3	π^0 Detector	47
105	3.2.2.4	Electromagnetic Calorimeter	48
106	3.2.2.5	Side Muon Range Detector	49
107	3.2.3	The Interactive Neutrino GRID	50
108	4	Bayesian Statistics and Markov Chain Monte Carlo Techniques	52
109	4.1	Bayesian Statistics	53
110	4.2	Monte Carlo Simulation	55
111	4.2.1	Markov Chain Monte Carlo	56
112	4.2.2	Metropolis-Hastings Algorithm	59
113	4.2.3	MCMC Optimisation	60
114	4.3	Understanding the MCMC Results	64
115	4.3.1	Marginalisation	64
116	4.3.2	Parameter Estimation and Credible Intervals	66
117	4.3.3	Bayesian Model Comparisons	67
118	4.3.4	Comparison of MCMC Output to Expectation	69
119	5	Simulation, Reconstruction, and Event Reduction	71
120	5.1	Simulation	71
121	5.2	Event Reconstruction at SK	76
122	5.3	Event Reduction at SK	87
123	6	Sample Selections and Systematics	92
124	6.1	Systematic Uncertainties	92
125	6.1.1	Beam Flux	92
126	6.1.2	Atmospheric Flux	94
127	6.1.3	Neutrino Interaction	96

¹²⁸	7 Oscillation Probability Calculation	97
¹²⁹	7.1 Overview	98
¹³⁰	7.2 Treatment of Fast Oscillations	106
¹³¹	7.3 Calculation Engine	112
¹³²	7.4 Matter Density Profile	115
¹³³	7.5 Production Height Averaging	121
¹³⁴	Bibliography	125
¹³⁵	List of Figures	136
¹³⁶	List of Tables	144

¹³⁸ **Chapter 1**

¹³⁹ **Introduction**

¹⁴⁰ **Chapter 2**

¹⁴¹ **Neutrino Oscillation Physics**

¹⁴² When first proposed, neutrinos were expected to be massless fermions that only in-
¹⁴³ teract through weak and gravitational forces. This meant they were very difficult to
¹⁴⁴ detect as they can pass through significant amounts of matter without interacting. De-
¹⁴⁵ spite this, experimental neutrino physics has developed with many different detection
¹⁴⁶ techniques and neutrino sources being used today. In direct tension with **the** standard
¹⁴⁷ model physics, neutrinos have been determined to oscillate between different lepton
¹⁴⁸ flavours, requiring them to have mass.

¹⁴⁹ **The observation techniques which lead to the discovery of the neutrino are doc-**
¹⁵⁰ **umented in section 2.1.** The theory underpinning neutrino oscillation is described
¹⁵¹ in section 2.2. **This section and** includes the approximations which can be made to
¹⁵² simplify the understanding of neutrino oscillation in **a the** two-flavour approxima-
¹⁵³ **tion as well as how the medium in which neutrinos propagate can manipulate the**
¹⁵⁴ **oscillation probability. The past Past**, current, and future neutrino experiments are
¹⁵⁵ detailed in section 2.3, including the reactor, atmospheric, and long-baseline accelerator
¹⁵⁶ neutrino sources that have been used to successfully constrain oscillation **parameters**
¹⁵⁷ **determination. Finally, the current state of oscillation parameter measurements are**
¹⁵⁸ **summarised in section 2.4.**

¹⁵⁹ 2.1 Discovery of Neutrinos

¹⁶⁰ At the start of the 20th century, the electrons emitted from the β -decay of the nucleus
¹⁶¹ were found to have a continuous energy spectrum [1,2]. This observation seemingly
¹⁶² broke the energy conservation invoked within that period's nuclear models. Postulated
¹⁶³ in 1930 by Pauli as the solution to this problem, the neutrino (originally termed
¹⁶⁴ "neutron") was theorized to be an electrically neutral spin-1/2 fermion with a mass
¹⁶⁵ of the same order of magnitude as the electron [3]. This neutrino was to be emitted
¹⁶⁶ with the electron in β -decay to alleviate the apparent breaking of energy conservation.
¹⁶⁷ As a predecessor of **the today's** weak interaction model, Fermi's theory of β -decay
¹⁶⁸ developed the understanding by coupling the four constituent particles; electron,
¹⁶⁹ proton, neutron, and neutrino, into a consistent model [4].

¹⁷⁰ Whilst Pauli was not convinced of the ability to detect neutrinos, **the first obser-**
¹⁷¹ **vations of the particle were made in the mid-1950s when neutrinos from a reactor**
¹⁷² **were observed via the inverse β -decay (IBD) process, $\bar{\nu}_e + p \rightarrow n + e^+$ [5,6]. The**
¹⁷³ **detector consisted of two parts: a neutrino interaction medium and a liquid scintillator.**
¹⁷⁴ **The interaction medium was built from two water tanks. These were loaded with**
¹⁷⁵ **cadmium chloride to allow increased efficiency of neutron capture. The positron**
¹⁷⁶ **emitted from IBD annihilates, $e^+ + e^- \rightarrow 2\gamma$, generating a prompt signal and the**
¹⁷⁷ **neutron is captured on the cadmium via $n + ^{108}Cd \rightarrow ^{109^*}Cd \rightarrow ^{109}Cd + \gamma$, producing**
¹⁷⁸ **a delayed signal. **The experiment observed an increase in the neutrino event rate****
¹⁷⁹ ****when the reactor was operating compared to when it was switched off, in much the****
¹⁸⁰ ****same way as modern reactor neutrino experiments operate. An increase in the coinci-****
¹⁸¹ ****dence rate was observed when the reactor was operating which was interpreted****
¹⁸² ****as interactions from neutrinos generated in the reactor.****

After the discovery of the ν_e , the natural question of how many flavours of neutrino exist was asked. In 1962, a measurement of the ν_μ was conducted at the Brookhaven National Laboratory [7]. A proton beam was directed at a beryllium target, generating a π -dominated beam which then decayed via $\pi^\pm \rightarrow \mu^\pm + (\nu_\mu, \bar{\nu}_\mu)$, and the subsequent interactions of the ν_μ were observed. **As the subsequent interaction of the neutrino generates muons rather than electrons, it was determined the ν_μ was fundamentally different from ν_e .** The final observation to be made was that of the ν_τ from the DONUT experiment [8]. Three neutrinos seem the obvious solution as it mirrors the known number of charged lepton (as they form weak isospin doublets) but there could be evidence of more. Several neutrino experiments have found anomalous results [9, 10] which could be attributed to sterile neutrinos. **However, however cosmological observations indicate the number of neutrino species $N_{eff} = 2.99 \pm 0.17$ [11], as measured from the cosmic microwave background power spectrum, and Stanford Linear Accelerator found the number of active neutrino flavours to be $N_\nu 2.9840 \pm 0.0082$ [12] from measurements of the Z-decay width.**

2.2 Theory of Neutrino Oscillation

As direct evidence of beyond Standard Model physics, a neutrino generated with lepton flavour α can change into a different lepton flavour β after propagating some distance. This phenomenon is called neutrino oscillation and requires that neutrinos must have a non-zero mass (as seen in subsection 2.2.1). This **observation** is direct evidence of beyond standard model physics. This behaviour has been characterised by the Pontecorvo-Maki-Nakagawa-Sakata (PMNS) [13–15] mixing matrix which describes how the flavour and mass of neutrinos are associated. This is analogous to the Cabibbo-Kobayashi-Maskawa (CKM) [16] matrix measured in quark physics.

²⁰⁸ 2.2.1 Three Flavour Oscillations

²⁰⁹ The PMNS parameterisation defines three flavour eigenstates, ν_e , ν_μ and ν_τ (indexed
²¹⁰ ν_α), which are **assigned based upon eigenstates of** the weak interaction **flavour states**
²¹¹ and three mass eigenstates, ν_1 , ν_2 and ν_3 (indexed ν_i). Each mass eigenstate is the
²¹² superposition of all three flavour states,

$$|\nu_i\rangle = \sum_{\alpha} U_{\alpha i} |\nu_{\alpha}\rangle. \quad (2.1)$$

²¹³ **Where** U is the PMNS matrix which **is unitary and connects correlates** the mass
²¹⁴ and flavour eigenstates.

²¹⁵ **Neutrinos interact with leptons of the same weak flavour eigenstate rather than**
²¹⁶ **mass eigenstate. The weak interaction couples to flavour eigenstates so neutrinos**
²¹⁷ **interact with leptons of the same flavour.** The propagation of a neutrino flavour
²¹⁸ eigenstate, in a vacuum, can be re-written as a plane-wave solution to the time-
²¹⁹ dependent Schrödinger equation,

$$|\nu_{\alpha}(t)\rangle = \sum_i U_{\alpha i}^{*} |\nu_i\rangle e^{-i\phi_i}. \quad (2.2)$$

²²⁰ The probability of observing a neutrino of flavour eigenstate β from one which
²²¹ originated as flavour α can be calculated as,

$$P(\nu_\alpha \rightarrow \nu_\beta) = |\langle \nu_\beta | \nu_\alpha(t) \rangle|^2 = \sum_{i,j} U_{\alpha i}^* U_{\beta i} U_{\alpha j} U_{\beta j}^* e^{-i(\phi_j - \phi_i)} \quad (2.3)$$

²²² The ϕ_i term can be expressed in terms of the energy, E_i , and magnitude of the
²²³ three momenta, p_i , of the neutrino, $\phi_i = E_i t - p_i x$ (t and x being time and position
²²⁴ coordinates). Therefore,

$$\phi_j - \phi_i = E_j t - E_i t - p_j x + p_i x. \quad (2.4)$$

²²⁵ For a relativistic particle, $E_i \gg m_i$,

$$p_i = \sqrt{E_i^2 - m_i^2} \approx E_i - \frac{m_i^2}{2E_i}. \quad (2.5)$$

²²⁶ Making the approximations that neutrinos are relativistic, the mass eigenstates
²²⁷ were created with the same energy and that $x = L$, where L is the distance traveled by
²²⁸ the neutrino, Equation 2.4 then becomes

$$\phi_j - \phi_i = \frac{\Delta m_{ij}^2 L}{2E}, \quad (2.6)$$

²²⁹ where $\Delta m_{ij}^2 = m_i^2 - m_j^2$. This, **teamed combined** with further use of unitarity
²³⁰ relations results in Equation 2.3 becoming

$$P(\nu_\alpha \rightarrow \nu_\beta) = \delta_{\alpha\beta} - 4 \sum_{i>j} \Re \left(U_{\alpha i}^* U_{\beta i} U_{\alpha j} U_{\beta j}^* \right) \sin^2 \left(\frac{\Delta m_{ij}^2 L}{4E} \right) \quad (2.7)$$

$$+ (-) 2 \sum_{i>j} \Im \left(U_{\alpha i}^* U_{\beta i} U_{\alpha j} U_{\beta j}^* \right) \sin \left(\frac{\Delta m_{ij}^2 L}{2E} \right).$$

²³¹ Where $\delta_{\alpha\beta}$ is the Kronecker delta function and the negative sign **on the last term** is
²³² included for the oscillation probability of antineutrinos.

²³³ Typically, the PMNS matrix is parameterised into three mixing angles, a charge
²³⁴ parity (CP) violating phase δ_{CP} , and two Majorana phases $\alpha_{1,2}$,

$$U = \underbrace{\begin{pmatrix} 1 & 0 & 0 \\ 0 & c_{23} & s_{23} \\ 0 & -s_{23} & c_{23} \end{pmatrix}}_{\text{Atmospheric, Accelerator}} \underbrace{\begin{pmatrix} c_{13} & 0 & s_{13}e^{-i\delta_{CP}} \\ 0 & 1 & 0 \\ -s_{13}e^{-i\delta_{CP}} & 0 & c_{13} \end{pmatrix}}_{\text{Reactor, Accelerator}} \underbrace{\begin{pmatrix} c_{12} & s_{12} & 0 \\ -s_{12} & c_{12} & 0 \\ 0 & 0 & 1 \end{pmatrix}}_{\text{Reactor, Solar}} \underbrace{\begin{pmatrix} e^{i\alpha_1/2} & 0 & 0 \\ 0 & e^{i\alpha_2/2} & 0 \\ 0 & 0 & 1 \end{pmatrix}}_{\text{Majorana}}. \quad (2.8)$$

²³⁵ Where $s_{ij} = \sin(\theta_{ij})$ and $c_{ij} = \cos(\theta_{ij})$. The oscillation parameters are often
²³⁶ grouped; (1,2) as “solar”, (2,3) as “atmospheric” and (1,3) as “reactor”. Many
²³⁷ neutrino experiments aim to measure the PMNS parameters from a wide array of
²³⁸ origins, as is the purpose of this thesis.

²³⁹ The Majorana phase, $\alpha_{1,2}$, **containing matrix** included within **the fourth matrix**
²⁴⁰ **in** Equation 2.8 is only included for completeness. For an oscillation analysis ex-
²⁴¹ periment, **any term in this oscillation probability calculation containing this phase**
²⁴² **disappears any terms containing this phase disappear** due to taking the expectation

243 value of the PMNS matrix. Measurements of these phases are typically performed
244 by experiments searching for neutrino-less double β -decay [17].

245 A two flavour approximation can be attained obtained when one assumes the third
246 mass eigenstate is degenerate with another. As discussed in section 2.3, it is found
247 that $\Delta m_{21}^2 \ll |\Delta m_{31}^2|$. This results in the two flavour approximation being reasonable
248 for understanding the features of the oscillation. In this two flavour case, the mixing
249 matrix becomes,

$$U_{2\text{ Flav.}} = \begin{pmatrix} \cos(\theta) & \sin(\theta) \\ -\sin(\theta) & \cos(\theta) \end{pmatrix}. \quad (2.9)$$

250 This culminates in the oscillation probability,

$$\begin{aligned} P(\nu_\alpha \rightarrow \nu_\alpha) &= 1 - \sin^2(2\theta) \sin^2\left(\frac{\Delta m^2 L}{4E}\right), \\ P(\nu_\alpha \rightarrow \nu_\beta) &= \sin^2(2\theta) \sin^2\left(\frac{\Delta m^2 L}{4E}\right). \end{aligned} \quad (2.10)$$

251 For Where $\alpha \neq \beta$. For a fixed neutrino energy, the oscillation probability is a sinu-
252 soidal function depending upon the distance over which the neutrino propagates. The
253 frequency and amplitude of oscillation are dependent upon the ratio of the $\Delta m^2/4E$
254 and $\sin^2 2\theta$, respectively. The oscillation probabilities presented thus far assume
255 $c = 1$, where c is the speed of light in vacuum. In more familiar units, the maxi-
256 mum oscillation probability for a fixed value of θ is given at $L[\text{km}] / E[\text{GeV}] \sim 1.27/\Delta m^2$.
257 It is this calculation that determines the best L/E value for a given experiment to be
258 designed around for measurements of a specific value of Δm^2 .

²⁵⁹ 2.2.2 The MSW Effect

²⁶⁰ The theory of neutrino oscillation in a vacuum **is has been** described in subsection 2.2.1.
²⁶¹ However, the beam neutrinos and atmospheric neutrinos originating from below the
²⁶² horizon propagate through matter in the Earth. The coherent scattering of neutrinos
²⁶³ from a material target modifies the Hamiltonian of the system. This results in a change
²⁶⁴ in the oscillation probability. Notably, charged current scattering ($\nu_e + e^- \rightarrow \nu_e + e^-$,
²⁶⁵ propagated by a W boson) only affects electron neutrinos **compared to whereas** the
²⁶⁶ neutral current scattering ($\nu_l + l^- \rightarrow \nu_l + l^-$, propagated by a Z^0 boson) interacts
²⁶⁷ through all neutrino flavours equally. In the two-flavour **limit approximation**, the
²⁶⁸ effective mixing parameter becomes

$$\sin^2(2\theta) \rightarrow \sin^2(2\theta_m) = \frac{\sin^2(2\theta)}{(A/\Delta m^2 - \cos(2\theta))^2 + \sin^2(2\theta)}, \quad (2.11)$$

²⁶⁹ where $A = 2\sqrt{2}G_F N_e E$, **with** N_e is the electron density of the medium and G_F is
²⁷⁰ Fermi's constant. It is clear to see that there exists a value of $A = \Delta m^2 \cos(2\theta)$ for
²⁷¹ $\Delta m^2 > 0$ which results in a divergent mixing parameter. This resonance is **due to**
²⁷² **termed** the Mikheyev-Smirnov-Wolfenstein (MSW) effect (or more colloquially, the
²⁷³ matter resonance) which regenerates the electron neutrino component of the neutrino
²⁷⁴ flux [18–20]. The density at which the resonance occurs is given by

$$N_e = \frac{\Delta m^2 \cos(2\theta)}{2\sqrt{2}G_F E}. \quad (2.12)$$

275 At densities lower than this critical value, the oscillation probability will be much
276 closer to that of vacuum oscillation. **For antineutrinos, $N_e \rightarrow -N_e$** [21]. The reso-
277 nance occurring from the MSW effect depends on the sign of Δm^2 . Therefore, any
278 neutrino oscillation experiment which observes neutrinos and antineutrinos which
279 have propagated through matter can have some sensitivity to the ordering of the
280 neutrino mass eigenstates.

281 2.3 Neutrino Oscillation Measurements

282 As evidence of beyond standard model physics, the 2015 Nobel Prize in Physics was
283 awarded to the Super-Kamiokande (SK) [22] and Sudbury Neutrino Observatory
284 (SNO) [23] collaborations for the first definitive observation of solar and atmospheric
285 neutrino oscillation [24]. Since then, the field has seen a wide array of oscillation
286 measurements from a variety of neutrino sources. As seen in subsection 2.2.1, the
287 neutrino oscillation probability is dependent on the ratio of the propagation baseline, L ,
288 to the neutrino energy, E . It is this ratio that determines the type of neutrino oscillation
289 a particular experiment is sensitive to.

290 As illustrated in Figure 2.1, there are many neutrino sources that span a wide
291 range of energies. The least energetic neutrinos are from diffuse supernovae and
292 terrestrial neutrinos at $O(1)$ MeV whereas the most energetic neutrinos originate from
293 atmospheric and galactic neutrinos of $> O(1)$ TeV.

294 2.3.1 Solar Neutrinos

295 Solar neutrinos are emitted from fusion reaction chains at the center of the Sun. The
296 solar neutrino flux, given as a function of neutrino energy for different fusion and

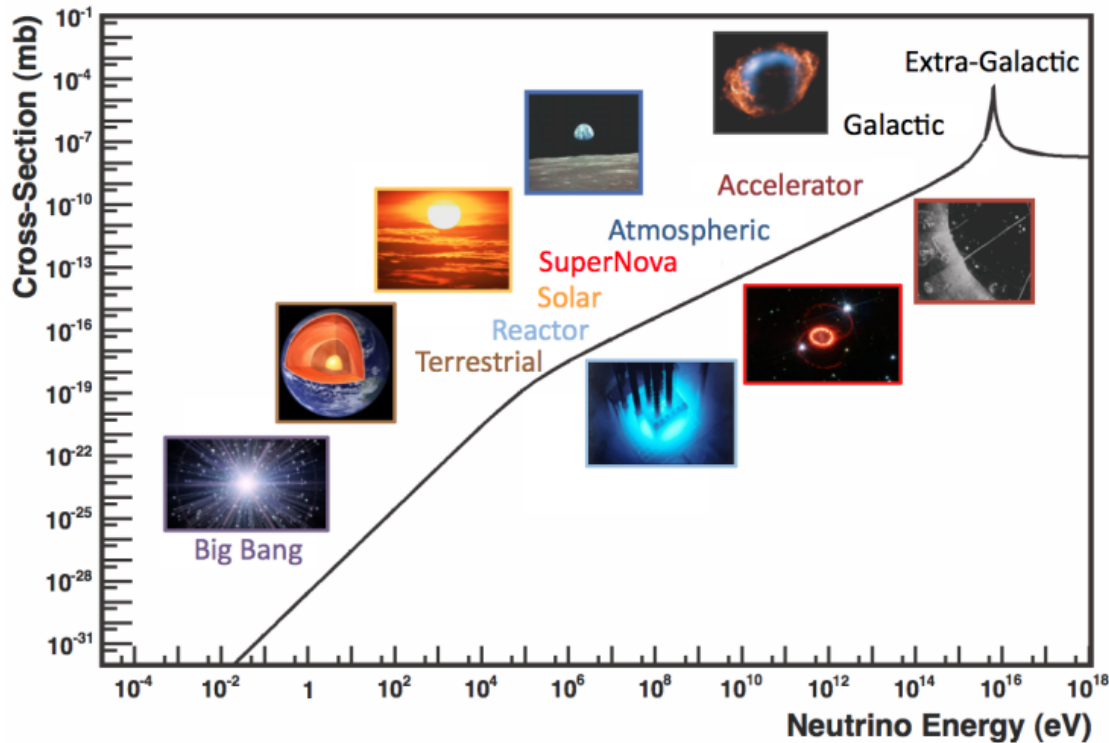


Figure 2.1: The cross-section of neutrinos from various natural and man-made sources as a function of neutrino energy. Taken from [25]

297 decay chains, is illustrated in Figure 2.2. Whilst proton-proton fusion generates the
 298 largest flux of neutrinos, the neutrinos are of low energy and are difficult to reconstruct
 299 due to the IBD interaction threshold of 1.8MeV. Consequently, most experiments focus
 300 on the neutrinos from the decay of 8B (via ${}^8B \rightarrow {}^8Be^* + e^+ + \nu_e$), which are higher
 301 energy.

302 The first measurements of solar neutrinos observed a significant reduction in the
 303 event rate compared to predictions from the Standard Solar Model [27, 28]. The
 304 proposed solution to this “solar neutrino problem” was $\nu_e \leftrightarrow \nu_\mu$ oscillations in a
 305 precursory version of the PMNS model [29]. The Kamiokande [30], Gallex [31] and
 306 Sage [32] experiments confirmed the ~ 0.5 factor deficit of solar neutrinos.

307 The conclusive solution to this problem was determined by the SNO collabora-
 308 tion [33]. Using a deuterium water target to observe 8B neutrinos, the event rate of
 309 charged current (CC), neutral current (NC), and elastic scattering (ES) interactions

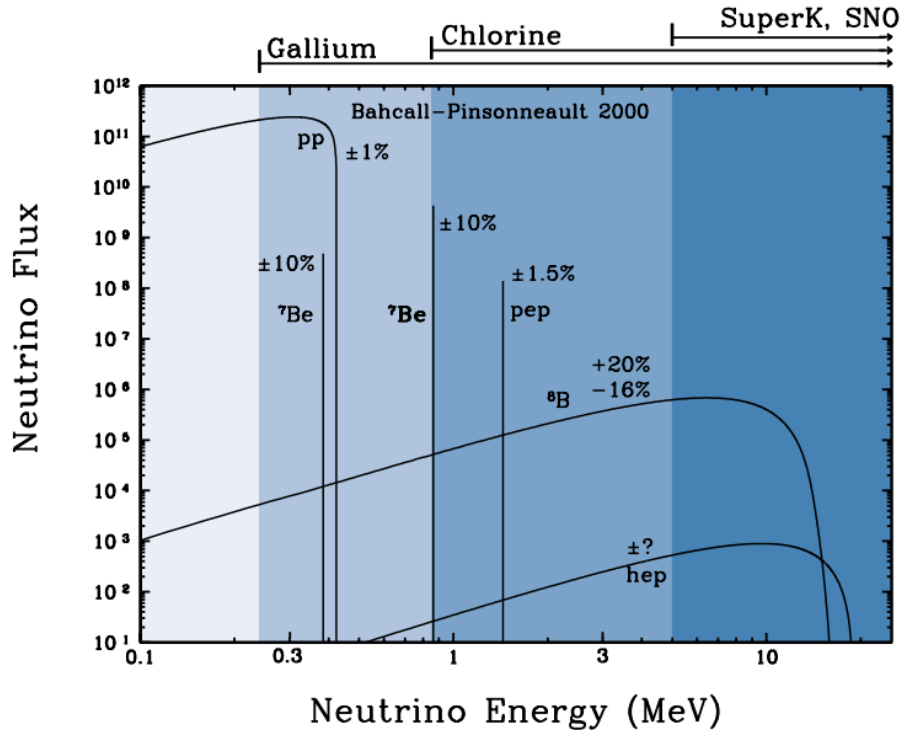
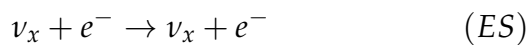
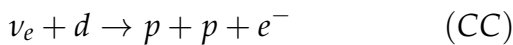


Figure 2.2: The solar neutrino flux as a function of neutrino energy for various fusion reactions and decay chains as predicted by the Standard Solar Model. Taken from [26].

(Given in Equation 2.13) was simultaneously measured. CC events can only occur for electron neutrinos, whereas the **other interaction NC channels are is** agnostic to neutrino flavour (**Although , and** the ES reaction **is more sensitive has a slight excess sensitivity** to electron neutrino interactions). This meant that there were direct measurements of the ν_e and ν_x neutrino flux. It was concluded that the CC and ES interaction rates were consistent with the deficit previously observed. Most importantly, the NC reaction rate was only consistent with the others under the hypothesis of flavour transformation.



³¹⁸ Many experiments have since measured the neutrino flux of different interaction
³¹⁹ chains within the sun [34–36]. The most recent measurement was that of CNO neutrinos
³²⁰ which were recently observed with 5σ significance by the Borexino collaboration.
³²¹ Future neutrino experiments aim to further these spectroscopic measurements of
³²² different fusion chains within the Sun [37–39]. Solar neutrinos act as an irreducible
³²³ background for dark matter experiments like DARWIN but oscillation parameter
³²⁴ measurements can be made [40].

³²⁵ 2.3.2 Atmospheric Neutrinos

³²⁶ The interactions of primary cosmic ray protons in Earth’s upper atmosphere generate
³²⁷ showers of energetic hadrons. These are mostly pions and kaons which when they
³²⁸ decay produce a natural source of neutrinos spanning energies of MeV to TeV [41].
³²⁹ **This** The main decay is via

$$\begin{aligned} \pi^\pm &\rightarrow \mu^\pm + (\nu_\mu, \bar{\nu}_\mu) \\ \mu^\pm &\rightarrow e^\pm + (\nu_e, \bar{\nu}_e) + (\nu_\mu, \bar{\nu}_\mu) \end{aligned} \tag{2.14}$$

³³⁰ such that for a single pion decay, three neutrinos are typically produced. The
³³¹ atmospheric neutrino flux energy spectra as predicted by the Bartol [42], Honda
³³² [43–45], and FLUKA [46] models are illustrated in Figure 2.3. The flux distribution
³³³ peaks at an energy of $O(10)\text{GeV}$. The uncertainties associated with these models
³³⁴ are dominated by the hadronic production of kaon and pions as well as the primary
³³⁵ cosmic flux.

³³⁶ Unlike long-baseline experiments which have a fixed baseline, the distance at-
³³⁷ mospheric neutrinos propagate is dependent upon the zenith angle at which they

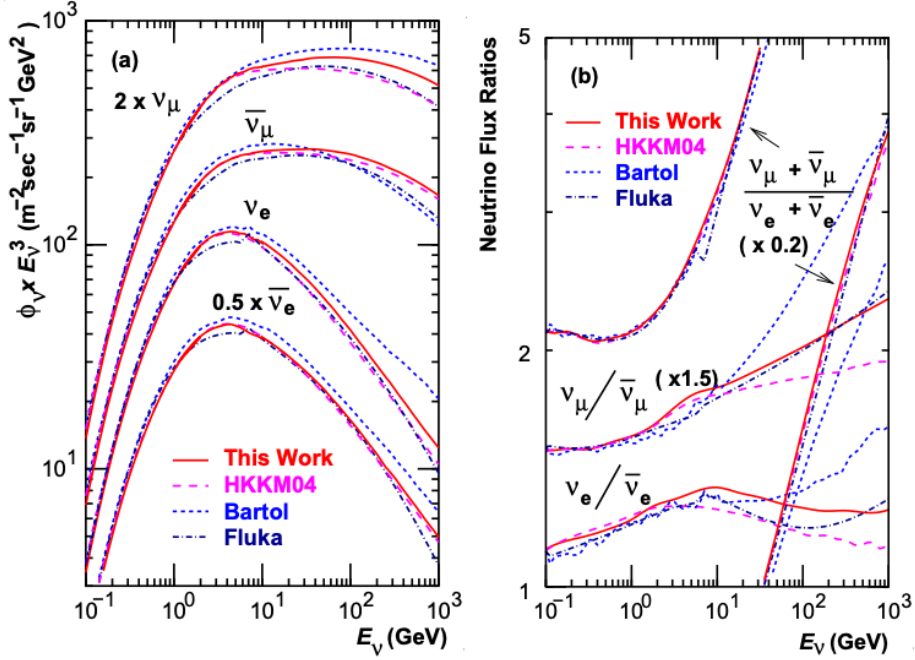


Figure 2.3: Left panel: The atmospheric neutrino flux for different neutrino flavours as a function of neutrino energy as predicted by the 2007 Honda model (“This work”) [43], the 2004 Honda model (“HKKM04”) [44], the Bartol model [42] and the FLUKA model [46]. Right panel: The ratio of the muon to electron neutrino flux as predicted by all the quoted models. Both figures taken from [43].

338 interact. This is illustrated in Figure 2.4. Neutrinos that are generated directly above
 339 the detector ($\cos(\theta) = 1.0$) have a baseline equivalent to the height of the atmosphere
 340 whereas neutrinos that interact directly below the detector ($\cos(\theta) = -1.0$) have to
 341 travel a length equal to the diameter of the Earth. This means atmospheric neutrinos
 342 have a baseline that varies from $O(20)\text{km}$ to $O(6 \times 10^3)\text{km}$. Any neutrino generated
 343 at or below the horizon will be subject to matter effects as they propagate through the
 344 Earth.

345 Figure 2.5 highlights the neutrino flux as a function of the zenith angle for different
 346 slices of neutrino energy. For medium to high-energy neutrinos (and to a lesser degree
 347 for low-energy neutrinos), the flux is approximately symmetric around $\cos(\theta) = 0$.
 348 To the accuracy of this approximation, the systematic uncertainties associated with
 349 atmospheric flux for comparing upward-going and down-going neutrino cancels. This

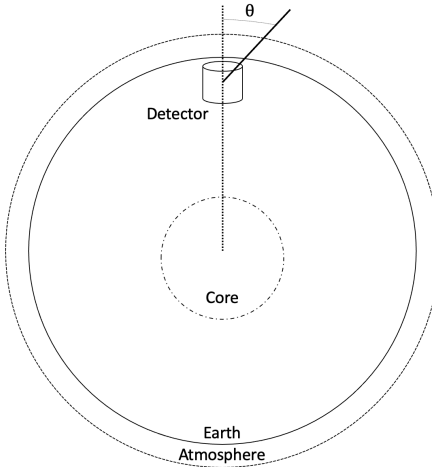


Figure 2.4: A diagram illustrating the definition of zenith angle as used in the Super Kamiokande experiment [47].

350 allows the down-going events, which are mostly insensitive to oscillation probabilities,
 351 to act as an unoscillated prediction (similar to a near detector in an accelerator neutrino
 352 experiment).

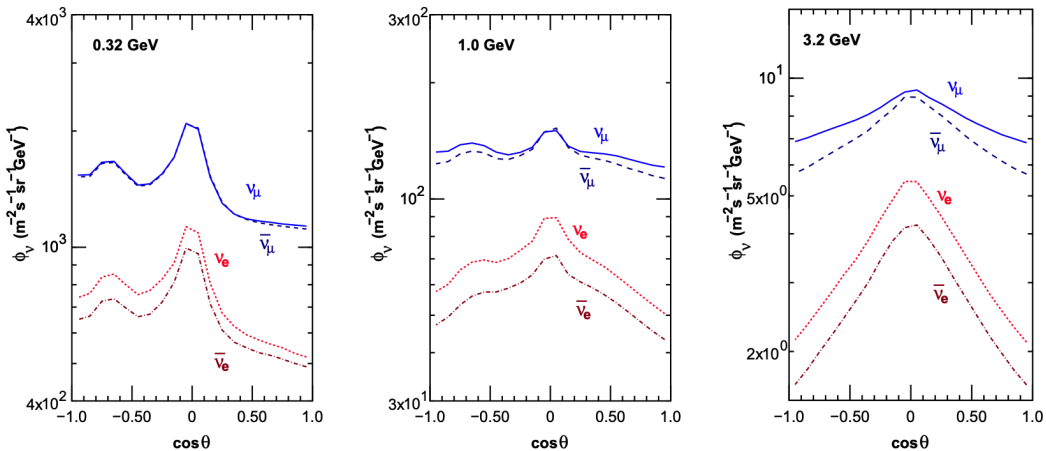


Figure 2.5: Prediction of ν_e , $\bar{\nu}_e$, ν_μ , $\bar{\nu}_\mu$ fluxes as a function of zenith angle as calculated by the HKKM model [45]. The left, middle and right panels represent three values of neutrino energy, 0.32GeV, 1.0GeV and 3.2GeV respectively. Predictions for other models including Bartol [42], Honda [43] and FLUKA [46] are given in [47].

353 Precursory hints of atmospheric neutrinos were observed in the mid-1960s search-
 354 ing for $\nu_\mu^{(-)} + X \rightarrow X^* + \mu^\pm$ [48], although it was called an anomaly at the time of
 355 measurement. This was succeeded with the IMB-3 [49] and Kamiokande [50] experi-

ments which measured the ratio of muon neutrinos compared to electron neutrinos $R(\nu_\mu/\nu_e)$. Both experiments were found to have a consistent deficit of muon neutrinos, with $R(\nu_\mu/\nu_e) = 0.67 \pm 0.17$ and $R(\nu_\mu/\nu_e) = 0.60^{+0.07}_{-0.06} \pm 0.05$. Super-Kamiokande (SK) [47] extended this analysis by fitting oscillation parameters in $P(\nu_\mu \rightarrow \nu_\tau)$ which found best fit parameters $\sin^2(2\theta) > 0.92$ and $1.5 \times 10^{-3} < \Delta m^2 < 3.4 \times 10^{-3} \text{ eV}^2$.

Since then, atmospheric neutrino experiments have been making precision measurements of the $\sin^2(\theta_{23})$ and Δm^2_{32} oscillation parameters. Atmospheric neutrino oscillation is dominated by $P(\nu_\mu \rightarrow \nu_\tau)$, where SK observed a 4.6σ discovery of ν_τ appearance [51]. Figure 2.6 illustrates the current estimates on the atmospheric mixing parameters from a wide range of atmospheric and accelerator neutrino observatories.

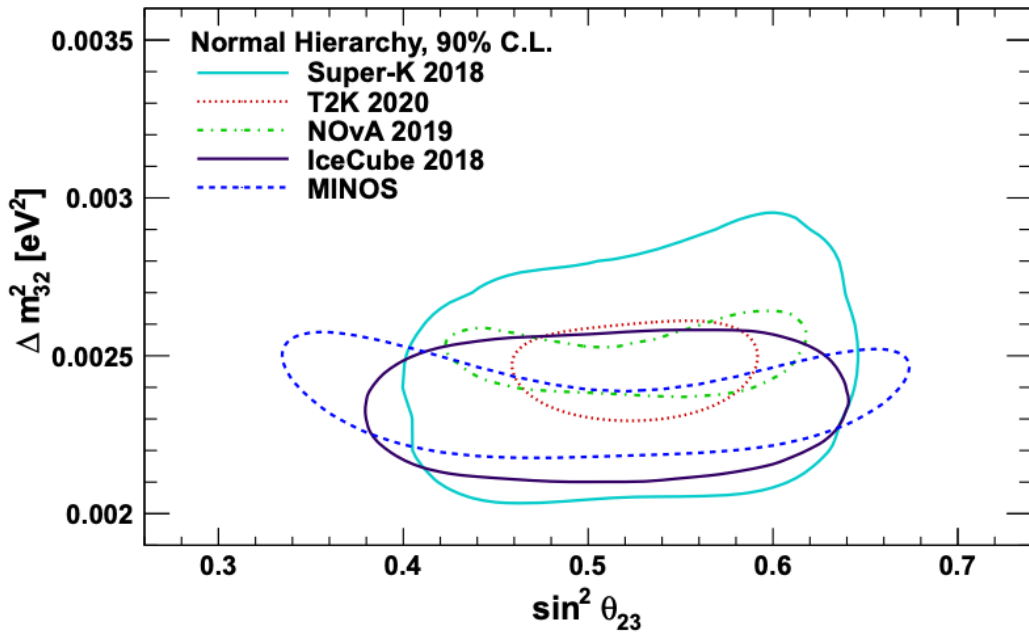


Figure 2.6: Constraints on the atmospheric oscillation parameters, $\sin^2(\theta_{23})$ and Δm^2_{32} , from atmospheric and long baseline experiments: SK [52], T2K [53], NOvA [54], IceCube [55] and MINOS [56]. Figure taken from [57].

³⁶⁶ 2.3.3 Accelerator Neutrinos

³⁶⁷ The concept of using a man-made “neutrino beam” was first realised in 1962 [58].
³⁶⁸ Since then, many experiments have followed which all use the same fundamental
³⁶⁹ concepts. Typically, a proton beam is aimed at a target producing charged mesons that
³⁷⁰ decay to neutrinos. The mesons can be sign-selected by the use of magnetic focusing
³⁷¹ horns to generate a neutrino or antineutrino beam. Pions are the primary meson that
³⁷² decay and depending on the orientation of the magnetic field, a muon (anti-)neutrino
³⁷³ beam is generated via $\pi^+ \rightarrow \mu^+ + \nu_\mu$ or $\pi^- \rightarrow \mu^- + \bar{\nu}_\mu$. The decay of muons and
³⁷⁴ kaons does result in an irreducible intrinsic electron neutrino background. In T2K,
³⁷⁵ this background contamination is $O(< 1\%)$ [59]. There is also an approximately
³⁷⁶ $\sim 5\%$ “wrong-sign” neutrino background of $\bar{\nu}_\mu$ generated via the same decays. **As**
³⁷⁷ **the beam is generated by proton interactions (rather than anti-proton interactions),**
³⁷⁸ **the wrong-sign component in the antineutrino beam is larger when operating in**
³⁷⁹ **neutrino mode.**

³⁸⁰ **The energy of each neutrino in the beam is dependent on the energy of the**
³⁸¹ **initial proton beam. Therefore, tuning the proton energy allows Tuning the proton**
³⁸² **energy in the beam and using beam focusing techniques allows** the neutrino energy
³⁸³ to be set to a value that maximises the disappearance oscillation probability in the L/E
³⁸⁴ term in Equation 2.10. This means that accelerator experiments are typically more
³⁸⁵ sensitive to the mixing parameters as compared to a natural neutrino source. However,
³⁸⁶ the disadvantage compared to atmospheric neutrino experiments is that the baseline
³⁸⁷ has to be shorter due to the lower flux. Consequently, there is typically less sensitivity
³⁸⁸ to matter effects and the ordering of the neutrino mass eigenstates.

³⁸⁹ A neutrino experiment measures

$$R(\vec{x}) = \Phi(E_\nu) \times \sigma(E_\nu) \times \epsilon(\vec{x}) \times P(\nu_\alpha \rightarrow \nu_\beta), \quad (2.15)$$

where $R(\vec{x})$ is the event rate of neutrinos at position \vec{x} , $\Phi(E_\nu)$ is the flux of neutrinos with energy E_ν , $\sigma(E_\nu)$ is the cross-section of the neutrino interaction and $\epsilon(\vec{x})$ is the efficiency **and resolution** of the detector. In order to leverage the most out of an accelerator neutrino experiment, the flux and cross-section systematics need to be constrained. This is typically done via the use of a “near detector”, situated at a baseline of $O(1)$ km. This detector observes the unoscillated neutrino flux and constrains the parameters used within the flux and cross-section model.

The first accelerator experiments to precisely measure oscillation parameters were MINOS [60] and K2K [61]. These experiments confirmed the $\nu_\mu \rightarrow \nu_\mu$ **oscillations** ν_μ **disappearance** seen in atmospheric neutrino experiments by finding consistent **mixing** parameter values for $\sin^2(\theta_{23})$ and Δm_{23}^2 . The current generation of accelerator neutrino experiments, T2K and NO ν A extended this field by observing $\bar{\nu}_\mu \rightarrow \bar{\nu}_e$ and lead the sensitivity to atmospheric mixing parameters as seen in Figure 2.6 [62]. The two experiments differ in their peak neutrino energy, baseline, and detection technique. The NO ν A experiment is situated at a baseline of 810km from the NuMI beamline which delivers 2GeV neutrinos. The T2K neutrino beam is peaked around 0.6GeV and propagates 295km. The NO ν A experiment also uses functionally identical detectors (near and far) which allow the approximate cancellation of detector systematics whereas T2K uses a plastic scintillator technique at the near detector and a water Cherenkov far detector. The future generation experiments DUNE [63] and Hyper-Kamiokande [64] will succeed these experiments as the high-precision era of neutrino oscillation parameter measurements develops.

412 Several anomalous results have been observed in the LSND [9] and MiniBooNE [10]
413 detectors which were designed with purposefully short baselines. Parts of the neu-
414 trino community attributed these results to oscillations induced by a fourth “sterile”
415 neutrino [65] but several searches in other experiments, MicroBooNE [66] and KAR-
416 MEN [67], found no hints of additional neutrino species. The solution to the anomalous
417 results **are is** still being determined.

418 2.3.4 Reactor Neutrinos

419 As illustrated in the first discovery of neutrinos (section 2.1), nuclear reactors are a very
420 useful man-made source of electron antineutrinos. For reactors that use low-enriched
421 uranium ^{235}U as fuel, the antineutrino flux is dominated by the β -decay fission of ^{235}U ,
422 ^{238}U , ^{239}Pu and ^{241}Pu [68] as illustrated in Figure 2.7.

423 Due to their low energy, reactor electron antineutrinos predominantly interact
424 via the inverse β -decay (IBD) interaction. The typical signature contains two signals
425 delayed by $O(200)\mu\text{s}$; firstly the prompt photons from positron annihilation, and
426 secondly the photons emitted ($E_{tot}^\gamma = 2.2\text{MeV}$) from de-excitation after neutron capture
427 on hydrogen. Searching for both signals improves the detector’s ability to distinguish
428 between background and signal events [70]. Recently, SK included gadolinium dopants
429 into the ultra-pure water to increase the energy released from the photon cascade to
430 $\sim 8\text{MeV}$ and reduce the time of the delayed signal to $\sim 28\mu\text{s}$.

431 There are many short baseline experiments ($L \sim O(1)\text{km}$) that have measured the
432 $\sin^2(\theta_{13})$ and Δm_{23}^2 oscillation parameters. Daya Bay [71], RENO [72] and Double
433 Chooz [73] have all provided precise measurements, with the first discovery of a
434 non-zero θ_{13} made by Daya Bay and RENO (and **complimented complemented** by
435 T2K [73]). The constraints on $\sin^2(\theta_{13})$ by the reactor experiments lead the field and

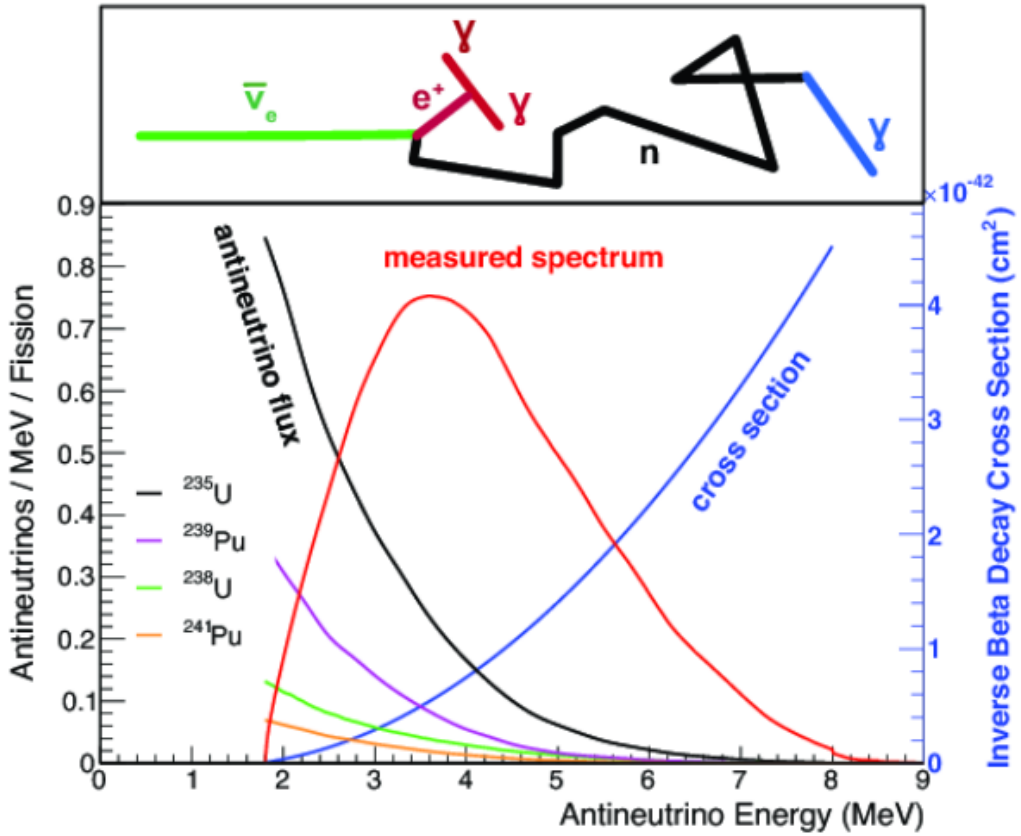


Figure 2.7: Reactor electron antineutrino fluxes for ^{235}U (Black), ^{238}U (Green), ^{239}Pu (Purple), and ^{241}Pu (Orange) isotopes. The inverse β -decay cross-section (Blue) and corresponding measurable neutrino spectrum (Red) are also given. Top panel: Schematic of Inverse β -decay interaction including the eventual capture of the emitted neutron. This capture emits a γ -ray which provides a second signal of the event. Taken from [69].

are often used as external inputs to accelerator neutrino experiments to improve their sensitivity to δ_{CP} and mass hierarchy determination. JUNO-TAO [74], a small collaboration within the larger JUNO experiment, is a next-generation reactor experiment that aims to precisely measure the isotopic antineutrino yields from the different fission chains. Alongside this, it aims to explain the ‘5MeV excess’ [75–77] by conducting a search for sterile neutrinos with a mass scale of around 1eV.

Kamland [78] is the only experiment to have observed reactor neutrinos using a long baseline (flux weighted averaged baseline of $L \sim 180\text{km}$) which allows it to have sensitivity to Δm_{12}^2 . Combined with the SK solar neutrino experiment, the combined

⁴⁴⁵ analysis puts the most stringent constraint on Δm_{12}^2 [79] ~~which is used as a prior~~
⁴⁴⁶ ~~uncertainty within accelerator neutrino experiments.~~

⁴⁴⁷ 2.4 Summary

⁴⁴⁸ Since observing the first evidence of neutrino oscillations in the late 1990's, numerous
⁴⁴⁹ measurements of the mixing parameters have been made. Many experiments use
⁴⁵⁰ neutrinos as a tool for discovery of new physics (diffuse supernova background,
⁴⁵¹ neutrinoless double beta decay and others) so the PMNS parameters are summarised
⁴⁵² in the Particle Data Group (PDG) review tables. The analysis presented in this thesis
⁴⁵³ focuses on the 2020 T2K oscillation analysis presented in [80] where the 2018 PDG
⁴⁵⁴ constraints [81] were used. These constraints are outlined in Table 2.1.

Parameter	2018 Constraint
$\sin^2(\theta_{12})$	0.307 ± 0.013
Δm_{21}^2	$(7.53 \pm 0.18) \times 10^{-5} \text{ eV}^2$
$\sin^2(\theta_{13})$	$(2.12 \pm 0.08) \times 10^{-2}$
$\sin^2(\theta_{23})$ (I.H., Q1)	$0.421^{+0.033}_{-0.025}$
$\sin^2(\theta_{23})$ (I.H., Q2)	$0.592^{+0.023}_{-0.030}$
$\sin^2(\theta_{23})$ (N.H., Q1)	$0.417^{+0.025}_{-0.028}$
$\sin^2(\theta_{23})$ (N.H., Q2)	$0.597^{+0.024}_{-0.030}$
Δm_{32}^2 (I.H.)	$(-2.56 \pm 0.04) \times 10^{-3} \text{ eV}^2$
Δm_{32}^2 (N.H.)	$(2.51 \pm 0.05) \times 10^{-3} \text{ eV}^2$

Table 2.1: The 2018 Particle Data Group constraints of the oscillation parameters taken from [81]. The value of Δm_{23}^2 is given for both normal hierarchy (N.H.) and inverted hierarchy (I.H.) and $\sin^2(\theta_{23})$ is broken down by whether its value is below (Q1) or above (Q2) 0.5.

⁴⁵⁵ The $\sin^2(\theta_{13})$ measurement stems from the electron antineutrino disappearance,
⁴⁵⁶ $P(\bar{\nu}_e \rightarrow \bar{\nu}_e)$, and is take as the average best-fit from the combination of Daya Bay,
⁴⁵⁷ Reno and Double Chooz. It is often used as a prior uncertainty within other neu-

trino oscillation experiments, typically termed the reactor constraint. The $\sin^2(\theta_{12})$ parameter is predominately measured through electron neutrino disappearance, $P(\nu_e \rightarrow \nu_{\mu,\tau})$, in solar neutrino experiments. The long-baseline reactor neutrino experiment Kamland also has sensitivity to this parameter and is used in a joint fit to solar data from SNO and SK, using the reactor constraint. Measurements of $\sin^2(\theta_{23})$ are made by long-baseline and atmospheric neutrino experiments. The PDG value is a joint fit of T2K, NO ν A , MINOS and IceCube DeepCore experiments. The latest T2K-only measurement, provided at Neutrino2020 and is the basis of this thesis, is given as $\sin^2(\theta_{23}) = 0.546^{+0.024}_{-0.046}$ [80]. The PDG constraint on Δm_{12}^2 is provided by the KamLAND experiment using solar and geoneutrino data. This measurement utilised a $\sin^2(\theta_{13})$ constraint from accelerator (T2K, MINOS) and reactor neutrino (Daya Bay, RENO, Double Chooz) experiments. Accelerator measurements make some of the most stringent constraints on Δm_{23}^2 although atmospheric experiments have more sensitivity to the mass hierarchy determination. The PDG performs a joint fit of accelerator and atmospheric data, in both normal and inverted hierarchy separately. The latest T2K-only result is $\Delta m_{32}^2 = 2.49^{+0.058}_{-0.082} \times 10^{-3} \text{ eV}^2$ favouring normal hierarchy [80]. The value of δ_{CP} is largely undetermined. CP-conserving values of 0 and π were rejected with $\sim 2\sigma$ intervals, as published in Nature, although more recent analysis have reduced the rejection intervals to 90%. Since the 2018 PDG publication, there has been a new measurement of $\sin^2(\theta_{13}) = (2.20 \pm 0.07) \times 10^{-2}$ [82], alongside updated Δm_{23}^2 and $\sin^2(\theta_{23})$ measurements.

Throughout this thesis, several sample spectra predictions and contours are presented which require oscillation parameters to be assumed. Table 2.2 defines two sets of oscillation parameters, with “Asimov A” set being close to the preferred values from a previous T2K-only fit [83] and “Asimov B” being CP-conserving and further from maximal θ_{23} mixing.

Parameter	Asimov A	Asimov B
Δm_{12}^2	$7.53 \times 10^{-5} \text{ eV}^2$	
Δm_{32}^2	$2.509 \times 10^{-3} \text{ eV}^2$	
$\sin^2(\theta_{12})$		0.304
$\sin^2(\theta_{13})$		0.0219
$\sin^2(\theta_{23})$	0.528	0.45
δ_{CP}	-1.601	0.0

Table 2.2: Reference values of the neutrino oscillation parameters for two different oscillation parameter sets.

484

Chapter 3

485

T2K and SK Experiment Overview

486 As the successor of the Kamiokande experiment, the Super-Kamiokande (SK) collabora-
487 ration has been leading atmospheric neutrino oscillation analyses for over two decades.
488 The detector has provided some of the strongest constraints on proton decay **limits**
489 and **as well as** the first precise measurements of the Δm_{23}^2 and $\sin^2(\theta_{23})$ neutrino
490 oscillation parameters. **Despite this, the The** ability of the detector to low-energy
491 neutrino events has been significantly improved with the recent gadolinium doping
492 of the ultra-pure water target. **section 2.1 describes the history, detection technique,**
493 **and operation of the SK detector. The history, detection technique, and operation**
494 **of the SK detector is described in section 3.1.**

495 The Tokai-to-Kamioka (T2K) experiment was one of the first long-baseline ex-
496 periments to use both neutrino and antineutrino beams to precisely measure the
497 charge parity violation within the neutrino sector. With the SK detector observing
498 the oscillated neutrino flux, the T2K experiment observed the first hints of a non-zero
499 $\sin^2(\theta_{13})$ measurement and continues to lead the field with the constraints it provides
500 on $\sin^2(\theta_{13})$, $\sin^2(\theta_{23})$, Δm_{23}^2 and δ_{CP} . **section 2.2 documents the The** techniques
501 which T2K uses in generating its neutrino beam as well as the near-detector used
502 to constrain the flux and cross-section parameters **invoked within the systematic**
503 **models used in this analysis are documented in section 3.2.**

⁵⁰⁴ 3.1 The Super-Kamiokande Experiment

⁵⁰⁵ The SK experiment began taking data in 1996 [84] and has had many modifications
⁵⁰⁶ throughout its lifespan. There have been seven defined periods of data taking as
⁵⁰⁷ noted in Table 3.1. Data taking began in SK-I which ran for five years. Between the
⁵⁰⁸ SK-I and SK-II periods, a significant proportion of the PMTs were damaged during
⁵⁰⁹ maintenance. Those that survived were equally distributed throughout the detector
⁵¹⁰ in the SK-II era, which resulted in a reduced photo-coverage. From SK-III onwards,
⁵¹¹ repairs to the detector meant the full suite of PMTs was operational. Before the
⁵¹² start of SK-IV, the data acquisition and electronic systems were upgraded. Between
⁵¹³ SK-IV and SK-V, a significant effort was placed into tank open maintenance and
⁵¹⁴ repair/replacement of defective PMTs, a task for which the author of this thesis was
⁵¹⁵ required. Consequently, the detector conditions were significantly different between
⁵¹⁶ the two operational periods. SK-VI saw the start of the 0.01% gadolinium doped water.
⁵¹⁷ SK-VII, which started during the writing of this thesis, has increased the gadolinium
⁵¹⁸ concentration to 0.03% for continued operation [85].

Period	Start Date	End Date	Live-time (days)
I	April 1996	July 2001	1489.19
II	October 2002	October 2005	798.59
III	July 2006	September 2008	518.08
IV	September 2008	May 2018	3244.4
V	January 2019	July 2020	461.02
VI	July 2020	May 2022	583.3
VII	May 2022	Ongoing	N/A

Table 3.1: The various SK periods and respective live-time. The SK-VI live-time is calculated until 1st April 2022. SK-VII started during the writing of this thesis.

⁵¹⁹ **3.1.1 The SK Detector**

⁵²⁰ The basic structure of the Super-Kamiokande (SK) detector is a cylindrical tank with a
⁵²¹ diameter 39.3m and height 41.1m filled with ultrapure water [86]. A diagram of the
⁵²² significant components of the SK detector is **illustrated given** in Figure 3.1. The SK
⁵²³ detector is situated in the Kamioka mine in Gifu, Japan. The mine is underground with
⁵²⁴ roughly 1km rock overburden (2.7km water equivalent overburden) [87]. At this depth,
⁵²⁵ the rate of cosmic ray muons is significantly decreased to a value of $\sim 2\text{Hz}$. The top of
⁵²⁶ the tank is covered with stainless steel which is designed as a working platform for
⁵²⁷ maintenance, calibration, and location for high voltage and data acquisition electronics.

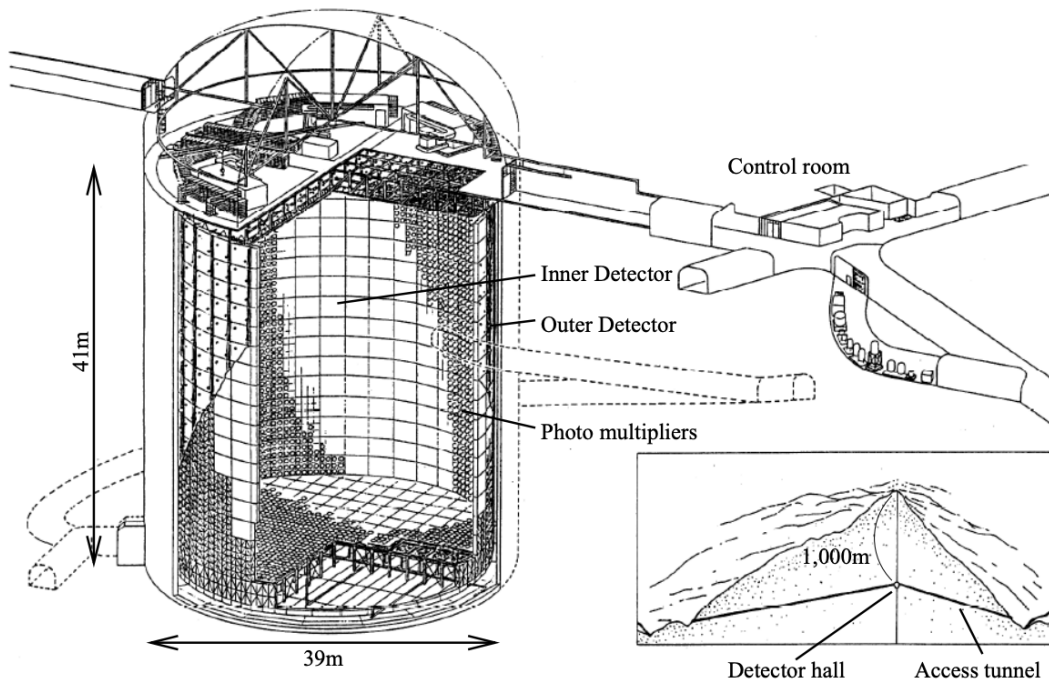


Figure 3.1: A schematic diagram of the Super-Kamiokande Detector. Taken from [88].

⁵²⁸ A smaller cylindrical structure (36.2m diameter, 33.8m height) is situated inside the
⁵²⁹ tank, with an approximate 2m gap between this structure and the outer tank wall. The
⁵³⁰ purpose of this structure is to support the photomultiplier tubes (PMTs). The volume
⁵³¹ inside and outside the support structure is referred to as the inner detector (ID) and

532 outer detector (OD), respectively. In the SK-IV era, the ID and OD are instrumented
533 by 11,129 50cm and 1,885 20cm PMTs respectively [86]. The ID contains a 32kton
534 mass of water. Many analyses performed at SK use a “fiducial volume” defined by the
535 volume of water inside the ID excluding some distance to the ID wall. This reduces the
536 volume of the detector which is sensitive to neutrino events but reduces radioactive
537 backgrounds and allows for better reconstruction performance. The nominal fiducial
538 volume is defined as the area contained inside 2m from the ID wall for a total of
539 22.5kton water [89].

540 The two regions of the detector (ID and OD) are optically separated with opaque
541 black plastic. The purpose of this is to determine whether a track entered or exited
542 the ID. This allows cosmic ray muons and partially contained events to be tagged and
543 separated from neutrino events entirely contained within the ID. This black plastic is
544 also used to cover the area between the ID PMTs to reduce photon reflection from the
545 ID walls. Opposite to this, the OD is lined with a reflective material to allow photons to
546 reflect around inside the OD until collected by one of the PMTs. Furthermore, each OD
547 PMT is backed with $50 \times 50\text{cm}$ plates of wavelength shifting acrylic which increases
548 the efficiency of light collection [87].

549 In the SK-IV data-taking period, the photocathode coverage of the detector, or the
550 fraction of the ID wall instrumented with PMTs, is $\sim 40\%$ [87]. The PMTs have a
551 quantum efficiency (the ratio of detected electrons to incident photons) of $\sim 21\%$ for
552 photons with wavelengths of $360\text{nm} < \lambda < 390\text{nm}$. The proportion of photoelectrons
553 that produce a signal in the dynode of a PMT, termed the collection efficiency, is
554 $> 70\%$ [87]. The PMTs used within SK are most sensitive to photons with wavelength
555 $300\text{nm} \leq \lambda \leq 600\text{nm}$ [87]. One disadvantage of using PMTs as the detection media
556 is that the Earth’s geomagnetic field can modify its response. Therefore, a set of

compensation coils is built around the inner surface of the detector to mitigate this effect [90].

As mentioned, the SK detector is filled with ultrapure water, which in a perfect world would contain no impurities. However, bacteria and organic compounds can significantly degrade the water quality. This decreases the attenuation length, which reduces the total number of photons that hit a PMT. To combat this, a sophisticated water treatment system has been developed [87, 91]. UV lights, mechanical filters, and membrane degasifiers are used to reduce the bacteria, suspended particulates, and radioactive materials from the water. The flow of water within the tank is also critical as it can remove stagnant bacterial growth or build-up of dust on the surfaces within the tank. Gravity drifts impurities in the water towards the bottom of the tank which, if left uncontrolled, can create asymmetric water conditions between the top and bottom of the tank. Typically, the water entering the tank is cooled below the ambient temperature of the tank to control convection and inhibit bacteria growth. Furthermore, the **rate of** dark noise hits within PMTs is sensitive to the PMT temperature [92] so controlling the temperature gradients within the tank is beneficial for stable measurements.

SK-VI is the first phase of the SK experiment to use gadolinium dopants within the ultrapure water [85]. As such, the SK water system had to be replaced to avoid removing the gadolinium concentrate from the ultrapure water [93]. For an inverse β -decay (IBD) interaction in a water target, the emitted neutron is thermally captured on hydrogen. This process releases 2.2MeV γ rays which are difficult to detect **due to as the resulting** Compton scattered electrons ~~from a γ ray of this energy is are~~ very close to the Cherenkov threshold, limiting the number of photons produced. Thermal capture of neutrons on gadolinium generates γ rays with higher energy (8MeV [70]) meaning they are more easily detected. SK-VI has 0.01% Gd loading

583 (0.02% gadolinium sulphate by mass) which causes $\approx 50\%$ of neutrons emitted by IBD
584 to be captured on gadolinium [94, 95]. Whilst predominantly useful for low energy
585 analyses, Gd loading allows better $\nu/\bar{\nu}$ separation for atmospheric neutrino event
586 selections [96]. Efforts are currently in place to increase the gadolinium concentrate
587 to 0.03% for $\approx 75\%$ neutron capture efficiency on gadolinium [97]. The final stage of
588 loading targets 0.1% concentrate.

589 3.1.2 Calibration

590 The calibration of the SK detector is documented in [86] and summarised below. The
591 analysis presented within this thesis is dependent upon ‘high energy events’ (Charged
592 particles with $O(> 100)\text{MeV}$ momenta). These are events that are expected to generate
593 a larger number of photons such that each PMT will be hit with multiple photons.
594 The reconstruction of these events depends upon the charge deposited within each
595 PMT and the timing response of each individual PMT. Therefore, the most relevant
596 calibration techniques to this thesis are outlined.

597 Before installation, 420 PMTs were calibrated to have identical charge responses
598 and then distributed throughout the tank in a cross-shape pattern (As illustrated by
599 Figure 3.2). These are used as a standardised measure for the rest of the PMTs installed
600 at similar geometric positions within SK to be calibrated against. To perform this
601 calibration, a xenon lamp is located at the center of the SK tank which flashes uniform
602 light at 1Hz. This allows for geometrical effects, water quality variation, and timing
603 effects to be measured in-situ throughout normal data-taking periods.

604 When specifically performing calibration of the detector (in out-of-data taking
605 mode), the water in the tank was circulated to avoid top/bottom asymmetric water
606 quality. Any non-uniformity within the tank significantly affects the PMT hit proba-

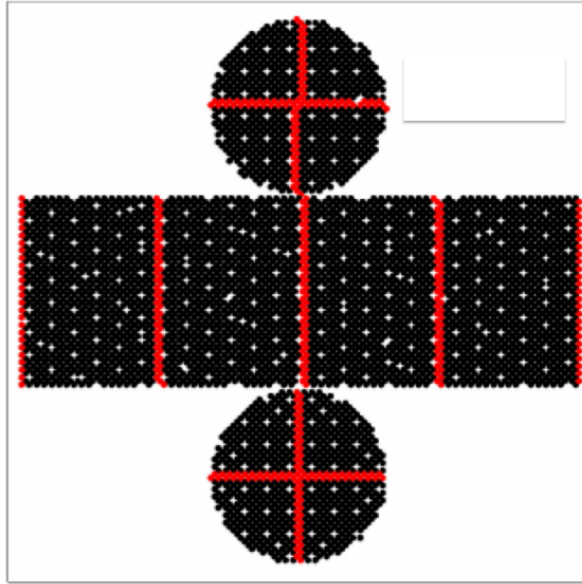


Figure 3.2: The location of “standard PMTs” (red) inside the SK detector. Taken from [86].

607 bility through scattering or absorption. This becomes a dominant effect for the very
 608 low-intensity light sources discussed later which are designed such that only one
 609 photon is incident upon a given PMT.

610 The “gain” of a PMT is defined as the ratio of the total charge of the signal produced
 611 compared to the charge of photoelectrons emitted by the photocathodes within the
 612 PMT. To calibrate the signal of each PMT, the “relative” and “absolute” gain values are
 613 measured. The relative gain is the variation of gain among each of the PMTs whereas
 614 the absolute gain is the average gain of all PMTs.

615 The relative gain is calibrated as follows. A laser is used to generate two measure-
 616 ments: a high-intensity flash that illuminates every PMT with a sufficient number of
 617 photons, and a low-intensity flash in which only a small number of PMTs collect light.
 618 The first measurement creates an average charge, $Q_{obs}(i)$ on PMT i , whereas the second
 619 measurement ensures that each hit PMT only generates a single photoelectron. For the
 620 low-intensity measurement, the number of times each PMT records a charge larger
 621 than 1/4 photoelectrons, $N_{obs}(i)$, is counted. The values measured can be expressed as

$$\begin{aligned} Q_{obs}(i) &\propto I_H \times f(i) \times \epsilon(i) \times G(i), \\ N_{obs}(i) &\propto I_L \times f(i) \times \epsilon(i), \end{aligned} \quad (3.1)$$

622 Where I_H and I_L is the intensity of the high and low flashes, $f(i)$ is the acceptance
 623 efficiency of the i^{th} PMT, $\epsilon(i)$ is the product of the quantum and collection efficiency
 624 of the i^{th} PMT and $G(i)$ is the gain of the i^{th} PMT. The relative gain for each PMT can
 625 determined by taking the ratio of these quantities.

626 The absolute gain calibration is performed by observing fixed energy γ -rays of
 627 $E_\gamma \sim 9\text{MeV}$ emitted isotropically from neutron capture on a NiCf source situated at
 628 the center of the detector. This generates a photon yield of about 0.004 photoelec-
 629 trons/PMT/event, meaning that $> 99\%$ of PMT signals are generated from single
 630 photoelectrons. A charge distribution is generated by performing this calibration over
 631 all PMTs, and the average value of this distribution is taken to be the absolute gain
 632 value.

633 As mentioned in subsection 3.1.1, the average quantum and collection efficiency
 634 for the SK detector is $\sim 21\%$ and $> 70\%$ respectively. However, these values do differ
 635 between each PMT and need to be calibrated accordingly. Consequently, the NiCf
 636 source is also used to calibrate the “quantum \times collection” efficiency (denoted “QE”)
 637 value of each PMT. The NiCf low-intensity source is used as the PMT hit probability
 638 is proportional to the QE ($N_{obs}(i) \propto \epsilon(i)$ in Equation 3.1). A Monte Carlo prediction
 639 which includes photon absorption, scattering, and reflection is made to estimate the
 640 number of photons incident on each PMT and the ratio of the number of predicted
 641 to observed hits is calculated. The difference is attributed to the QE efficiency of that
 642 PMT. This technique is extended to calculate the relative QE efficiency by normalizing
 643 the average of all PMTs which removes the dependence on the light intensity.

644 Due to differing cable lengths and readout electronics, the timing response between
645 a photon hitting the PMT and the signal being captured by the data acquisition can be
646 different between each PMT. Due to threshold triggers (Described in subsection 3.1.3),
647 the time at which a pulse reaches a threshold is dependent upon the size of the pulse.
648 This is known as the ‘time-walk’ effect and also needs to be accounted for in each PMT.
649 To calibrate the timing response, a pulse of light with width 0.2ns is emitted into the
650 detector through a diffuser. Two-dimensional distributions of time and pulse height
651 (or charge) are made for each PMT and are used to calibrate the timing response. This
652 is performed in-situ **whilst during** data taking with the light source pulsing at 0.03Hz.

653 The top/bottom water quality asymmetry is measured using the NiCf calibration
654 data and cross-referencing these results to the “standard PMTs”. The water attenuation
655 length is continuously measured by the rate of vertically-downgoing cosmic-ray
656 muons which enter via the top of the tank.

657 Dark noise is the phenomenon where a PMT registers a pulse that is consistent
658 with a single photoelectron emitted from photon detection despite the PMT being in
659 complete darkness. This is predominately caused by two processes. Firstly there is
660 intrinsic dark noise which is where photoelectrons gain enough thermal energy to be
661 emitted from the photocathode, and secondly, the radioactive decay of contaminants
662 inside the structure of the PMT. Typical dark noise rate for PMTs used within SK are
663 $O(3)$ kHz [87] **which equates to about 12 dark noise hits per 220ns**. This is lower than
664 the expected number of photons generated for a ‘high energy event’ (As described in
665 subsection 3.1.4) but instability in this value can cause biases in reconstruction. Dark
666 noise is related to the gain of a PMT and is calibrated using hits inside a time window
667 recorded before an event trigger [98].

⁶⁶⁸ 3.1.3 Data Acquisition and Triggering

⁶⁶⁹ The analysis presented in this thesis only uses the SK-IV period of the SK experiment
⁶⁷⁰ so this subsection focuses on the relevant points of the data acquisition and triggering
⁶⁷¹ systems to that SK period. The earlier data acquisition and triggering systems are
⁶⁷² documented in [99, 100].

⁶⁷³ Before the SK-IV period started, the existing front-end electronics were replaced
⁶⁷⁴ with “QTC-Based Electrons with Ethernet, QBEE” systems [101]. When the QBEE
⁶⁷⁵ observes a signal above a 1/4 photoelectron threshold, the charge-to-time (QTC)
⁶⁷⁶ converter generates a rectangular pulse. The start of the rectangular pulse indicates
⁶⁷⁷ the time at which the analog photoelectron signal was received and the width of the
⁶⁷⁸ pulse indicates the total charge integrated throughout the signal. This is then digitized
⁶⁷⁹ by time-to-digital converters and sent to the “front-end” PCs. The digitized signal
⁶⁸⁰ from every QBEE is then chronologically ordered and sent to the “merger” PCs. It is
⁶⁸¹ the merger PCs that apply the software trigger. Any triggered events are passed to the
⁶⁸² “organizer” PC. This sorts the data stream of multiple merger PCs into chronologically
⁶⁸³ ordered events which are then saved to disk. The schematic of data flow from PMTs to
⁶⁸⁴ disk is illustrated in Figure 3.3.

⁶⁸⁵ The software trigger (described in [103]) operates by determining the number of
⁶⁸⁶ PMT hits within a 200ns sliding window, $N_{200\text{-}}\text{.}$ **This window** coincides with the
⁶⁸⁷ maximum time that a Cherenkov photon would take to traverse the length of the SK
⁶⁸⁸ tank [100]. For lower energy events that generate fewer photons, this technique is
⁶⁸⁹ useful for eliminating background processes like dark noise and radioactive decay
⁶⁹⁰ which would be expected to separate in time. When the value of N_{200} exceeds some
⁶⁹¹ threshold, a software trigger is issued. There are several trigger thresholds used within
⁶⁹² the SK-IV period which are detailed in Table 3.2. If one of these thresholds is met, the

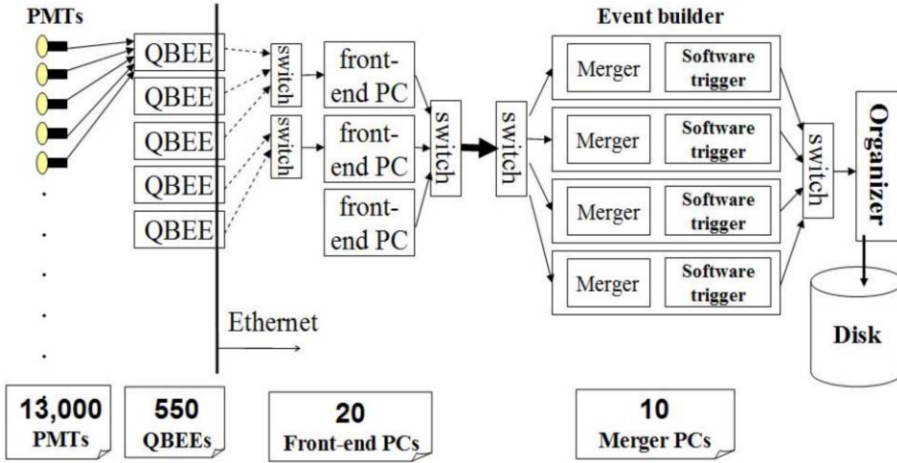


Figure 3.3: Schematic view of the data flow through the data acquisition and online system. Taken from [102].

693 PMT hits within an extended time window are also read out and saved to disk. In
 694 the special case of an event that exceeds the SHE trigger but does not exceed the OD
 695 trigger, the AFT trigger looks for delayed coincidences of 2.2MeV gamma rays emitted
 696 from neutron capture in a $535\mu\text{s}$ window after the SHE trigger. A similar but more
 697 complex “Wideband Intelligent Trigger (WIT)” has been deployed and is described
 698 in [104].

Trigger	Acronym	Condition	Extended time window (μs)
Super Low Energy	SLE	>34/31 hits	1.3
Low Energy	LE	>47 hits	40
High Energy	HE	>50 hits	40
Super High Energy	SHE	>70/58 hits	40
Outer Detector	OD	>22 hits in OD	N/A

Table 3.2: The trigger thresholds and extended time windows saved around an event which were utilised throughout the SK-IV period. The exact thresholds can change and the values listed here represent the thresholds at the start and end of the SK-IV period.

⁶⁹⁹ 3.1.4 Cherenkov Radiation

- ⁷⁰⁰ Cherenkov light is emitted from any highly energetic charged particle traveling
⁷⁰¹ with relativistic velocity, β , greater than the local speed of light in a medium [105].
⁷⁰² Cherenkov light is formed at the surface of a cone with characteristic pitch angle,

$$\cos(\theta) = \frac{1}{\beta n}. \quad (3.2)$$

⁷⁰³ where n is the refractive index of the medium. Consequently, the Cherenkov
⁷⁰⁴ momentum threshold, P_{thres} , is dependent upon the mass, m , of the charged particle
⁷⁰⁵ moving through the **media medium**,

$$P_{thres} = \frac{m}{\sqrt{n^2 - 1}} \quad (3.3)$$

⁷⁰⁶ For water, where $n = 1.33$, the Cherenkov threshold momentum and energy for
⁷⁰⁷ various particles are given in Table 3.3. In contrast, γ -rays are detected indirectly via
⁷⁰⁸ the combination of photons generated by Compton scattering and pair production.
⁷⁰⁹ The threshold for detection in the SK detector is typically higher than the threshold
⁷¹⁰ for photon production. This is due to the fact that the attenuation of photons in the
⁷¹¹ water means that typically $\sim 75\%$ of Cherenkov photons reach the ID PMTs. Then the
⁷¹² collection and quantum efficiencies described in subsection 3.1.1 result in the number
⁷¹³ of detected photons being lower than the number of photons which reach the PMTs.

Particle	Threshold Momentum (MeV)	Threshold Energy (MeV)
Electron	0.5828	0.7751
Muon	120.5	160.3
Pion	159.2	211.7
Proton	1070.0	1423.1

Table 3.3: The threshold momentum and energy for a particle to generate Cherenkov light in ultrapure water, as calculated in Equation 3.2 in ultrapure water which has refractive index $n = 1.33$.

The Frank-Tamm equation [106] describes the relationship between the number of

Cherenkov photons generated per unit length, dN/dx , the wavelength of the photons

generated, λ , and the relativistic velocity of the charged particle,

$$\frac{d^2N}{dx d\lambda} = 2\pi\alpha \left(1 - \frac{1}{n^2\beta^2}\right) \frac{1}{\lambda^2}. \quad (3.4)$$

where α is the fine structure constant. For a 100MeV momentum electron, approx-

imately 330 photons will be produced per centimeter in the $300\text{nm} \leq \lambda \leq 700\text{nm}$

region which the ID PMTs are most sensitive to [87].

3.2 The Tokai to Kamioka Experiment

The Tokai to Kamioka (T2K) experiment is a long-baseline neutrino oscillation exper-

iment located in Japan. Proposed in the early 2000s [107, 108] to replace K2K [109],

T2K was designed to observe electron neutrino appearance whilst precisely measuring

the oscillation parameters associated with muon neutrino disappearance [110]. The

experiment consists of a neutrino beam generated at the Japan Proton Accelerator

Research Complex (J-PARC), a suite of near detectors situated 280m from the beam

⁷²⁷ target, and the Super Kamiokande far detector positioned at a 295km baseline. The
⁷²⁸ cross-section view of the T2K experiment is drawn in Figure 3.4.

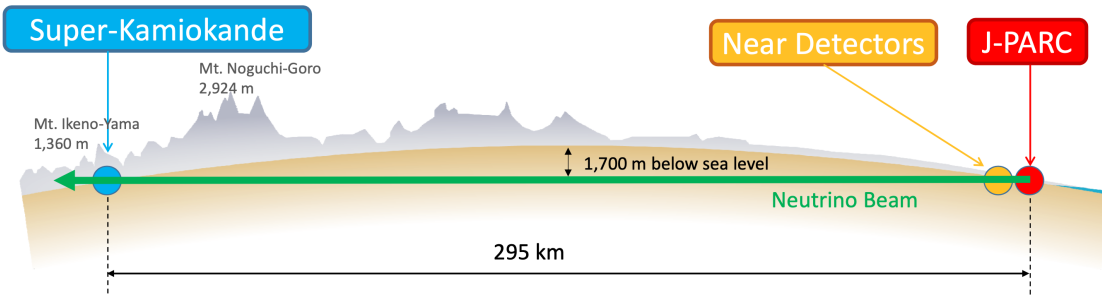


Figure 3.4: The cross-section view of the Tokai to Kamioka experiment illustrating the beam generation facility at J-PARC, the near detector situated at a baseline of 280m and the Super Kamiokande far detector situated 295km from the beam target.

⁷²⁹ The T2K collaboration makes world-leading measurements of the $\sin^2(\theta_{23})$, Δm_{23}^2 ,
⁷³⁰ and δ_{CP} oscillation parameters. Improvements in the precision and accuracy of param-
⁷³¹ eter estimates are still being made by including new data samples and developing the
⁷³² models which describe the neutrino interactions and detector responses [111]. Electron
⁷³³ neutrino appearance was first observed at T2K in 2014 [112] ~~which accompanied a~~
⁷³⁴ **7.3 σ significance of a non-zero $\sin^2(\theta_{13})$ measurement with 7.3 σ significance.**

⁷³⁵ The near detectors provide constraints on the beam flux and cross-section model
⁷³⁶ parameters used within the **fit oscillation analysis** by observing the unoscillated
⁷³⁷ neutrino beam. There are a host of detectors situated in the near detector hall (As
⁷³⁸ illustrated in Figure 3.5): ND280 (subsection 3.2.2), INGRID (subsection 3.2.3), NINJA
⁷³⁹ [113], WAGASCI [114], and Baby-MIND [115]. The latter three are not currently used
⁷⁴⁰ within the oscillation analysis presented within this thesis.

⁷⁴¹ Whilst this thesis presents the ND280 in terms of its purpose for the oscillation
⁷⁴² analysis, the detector can also make many cross-section measurements at neutrino
⁷⁴³ energies of $O(1)$ GeV for the different targets within the detector [116, 117]. These
⁷⁴⁴ measurements are of equal importance as they can lead the way in determining the

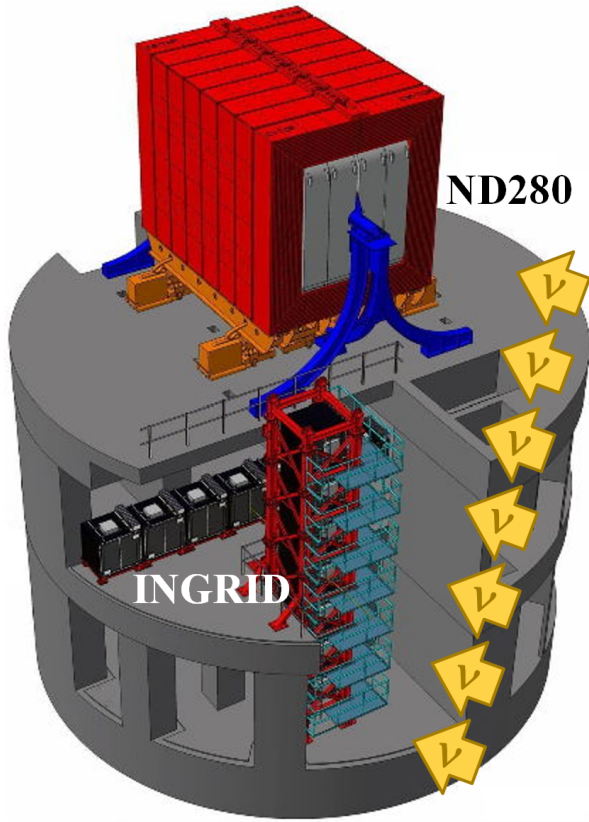


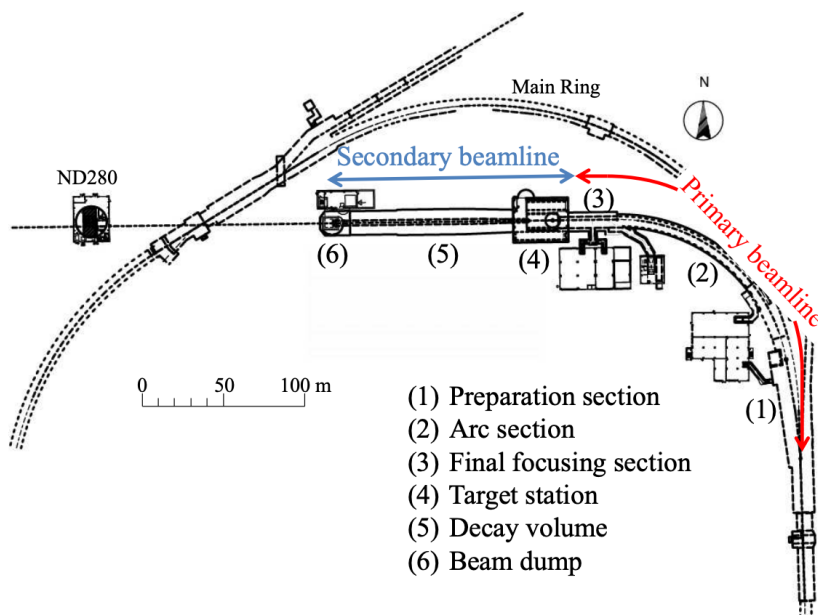
Figure 3.5: The near detector suite for the T2K experiment showing the ND280 and INGRID detectors. The distance between the detectors and the beam target is 280m.

745 model parameters used in the interaction models for the future high-precision era of
 746 neutrino physics.

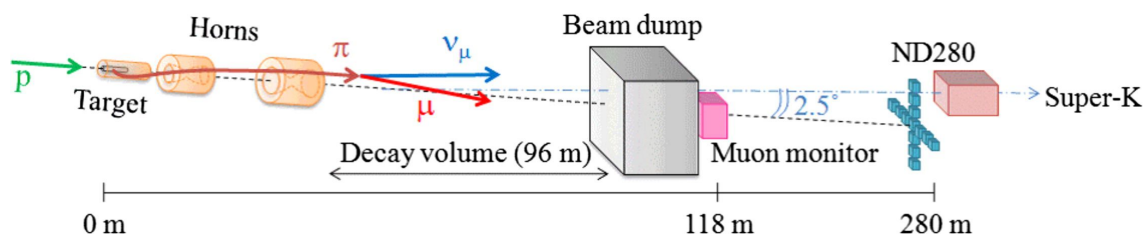
747 3.2.1 The Neutrino Beam

748 The neutrino beam used within the T2K experiment is described in [59, 118] and
 749 summarised below. The accelerating facility at J-PARC is composed of two sections; the
 750 primary and secondary beamlines. Figure 3.6 illustrates a schematic of the beamline,
 751 focusing mostly on the components of the secondary beamline. The primary beamline
 752 has three accelerators that progressively accelerate protons; a linear accelerator, a rapid-
 753 cycling synchrotron, and the main-ring (MR) synchrotron. Once fully accelerated by
 754 the MR, the protons have a kinetic energy of 30GeV. Eight bunches of these protons,

separated by 500ns, are extracted per “spill” from the MR and directed towards a graphite target (a rod of length 91.4cm and diameter 2.6cm). Spills are extracted at 0.5Hz with $\sim 3 \times 10^{14}$ protons contained per spill.



(a) Primary and secondary beamline

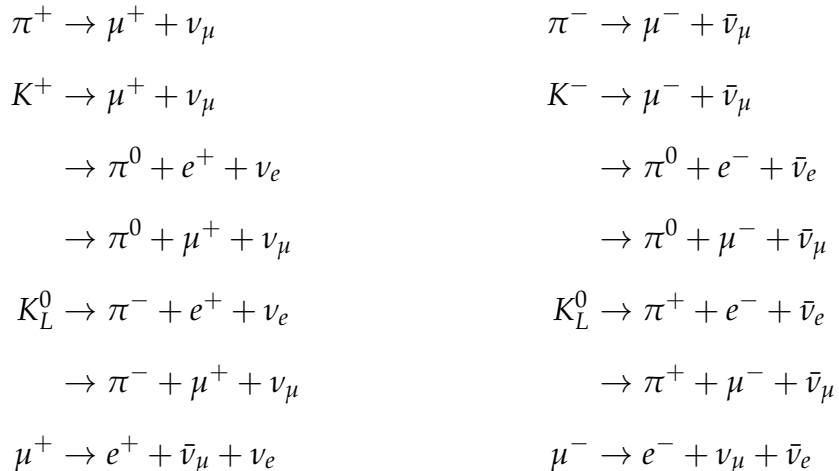


(b) Secondary beamline

Figure 3.6: Top panel: Bird's eye view of the most relevant part of primary and secondary beamline used within the T2K experiment. The primary beamline is the main-ring proton synchrotron, kicker magnet, and graphite target. The secondary beamline consists of the three focusing horns, decay volume, and beam dump. Figure taken from [118]. Bottom panel: The side-view of the secondary beamline including the focusing horns, beam dump and neutrino detectors. Figure taken from [119].

The secondary beamline consists of three main components: the target station, the decay volume, and the beam dump. The target station is comprised of the target, beam monitors, and three magnetic focusing horns. The proton beam interacts with the

⁷⁶¹ graphite target to form a secondary beam of mostly pions and kaons. The secondary
⁷⁶² beam travels through a 96m long decay volume, generating neutrinos through the
⁷⁶³ following decays [59],



⁷⁶⁴
⁷⁶⁵ The electrically charged component of the secondary beam is focused towards the
⁷⁶⁶ far detector by the three magnetic horns. These horns direct charged particles of a
⁷⁶⁷ particular polarity towards SK whilst defocusing the oppositely charged particles.
⁷⁶⁸ This allows a mostly neutrino or mostly antineutrino beam to be used within the
⁷⁶⁹ experiment, denoted as “forward horn current (FHC)” or “reverse horn current (RHC)”
⁷⁷⁰ respectively.

⁷⁷¹ Figure 3.7 illustrates the different contributions to the FHC and RHC neutrino flux.
⁷⁷² The low energy flux is dominated by the decay of pions whereas kaon decay becomes
⁷⁷³ the dominant source of neutrinos for $E_\nu > 3\text{GeV}$. The “wrong-sign” component,
⁷⁷⁴ which is the $\bar{\nu}_\mu$ background in a ν_μ beam, and the intrinsic irreducible ν_e background,
⁷⁷⁵ are predominantly due to muon decay for $E_\nu < 2\text{GeV}$. As the antineutrino **production**
⁷⁷⁶ cross-section is smaller than the neutrino cross-section, the wrong-sign component is
⁷⁷⁷ more dominant in the RHC beam as compared to that in the FHC beam.

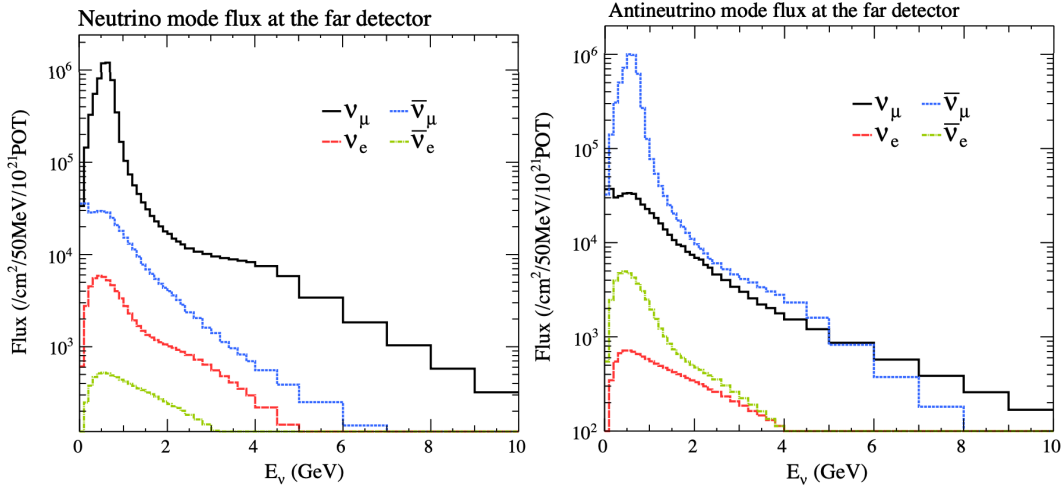


Figure 3.7: The Monte Carlo prediction of the energy spectrum for each flavour of neutrino (ν_e , $\bar{\nu}_e$, ν_μ and $\bar{\nu}_\mu$) in the neutrino dominated beam FHC mode (Left) and antineutrino dominated beam RHC mode (Right) expected at SK. Taken from [120].

The beam dump, situated at the end of the decay volume, stops all charged particles other than highly energetic muons ($p_\mu > 5\text{GeV}$). The MuMon detector monitors the penetrating muons to determine the beam direction and intensity which is used to constrain some of the beam flux systematics within the analysis [119, 121].

The T2K experiment uses an off-axis beam to narrow the neutrino energy distribution. This was the first implementation of this technique in a long-baseline neutrino oscillation experiment after its original proposal [122]. Pion decay, $\pi \rightarrow \mu + \nu_\mu$, is a two-body decay. Consequently, the neutrino energy, E_ν , can be determined based on the pion energy, E_π , and the angle at which the neutrino is emitted, θ ,

$$E_\nu = \frac{m_\pi^2 - m_\mu^2}{2(E_\pi - p_\pi \cos(\theta))}, \quad (3.5)$$

where m_π and m_μ are the mass of the pion and muon respectively. For a fixed energy pion, the neutrino energy distribution is dependent upon the angle at which the neutrinos are observed from the initial pion beam direction. For the 295km baseline at

⁷⁹⁰ T2K, $E_\nu = 0.6\text{GeV}$ maximises the electron neutrino appearance probability, $P(\nu_\mu \rightarrow \nu_e)$,
⁷⁹¹ whilst minimising the muon disappearance probability, $P(\nu_\mu \rightarrow \nu_\mu)$. Figure 3.8
⁷⁹² illustrates the neutrino energy distribution for a range of off-axis angles, as well as the
⁷⁹³ oscillation probabilities most relevant to T2K.

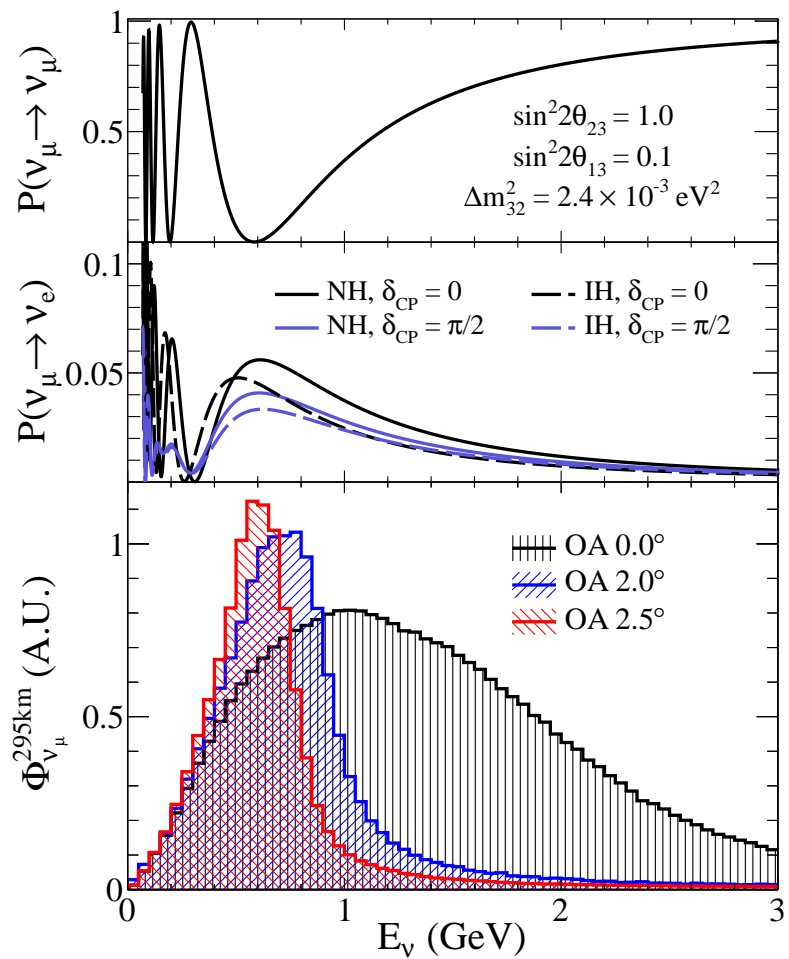


Figure 3.8: Top panel: T2K muon neutrino disappearance probability as a function of neutrino energy. Middle panel: T2K electron neutrino appearance probability as a function of neutrino energy. Bottom panel: The neutrino flux distribution for three different off-axis angles (Arbitrary units) as a function of neutrino energy.

⁷⁹⁴ 3.2.2 The Near Detector at 280m

⁷⁹⁵ Whilst all the near detectors are situated in the same “pit” located at 280m from the
⁷⁹⁶ beamline, the “ND280” detector is the off-axis detector which is situated at the same

⁷⁹⁷ off-axis angle as the Super-Kamiokande far detector. It has two primary functions;
⁷⁹⁸ firstly it measures the neutrino flux and secondly it counts the event rates of different
⁷⁹⁹ types of neutrino interactions. Both of these constrain the flux and cross-section
⁸⁰⁰ systematics invoked within the model for a more accurate prediction of the expected
⁸⁰¹ event rate at the far detector.

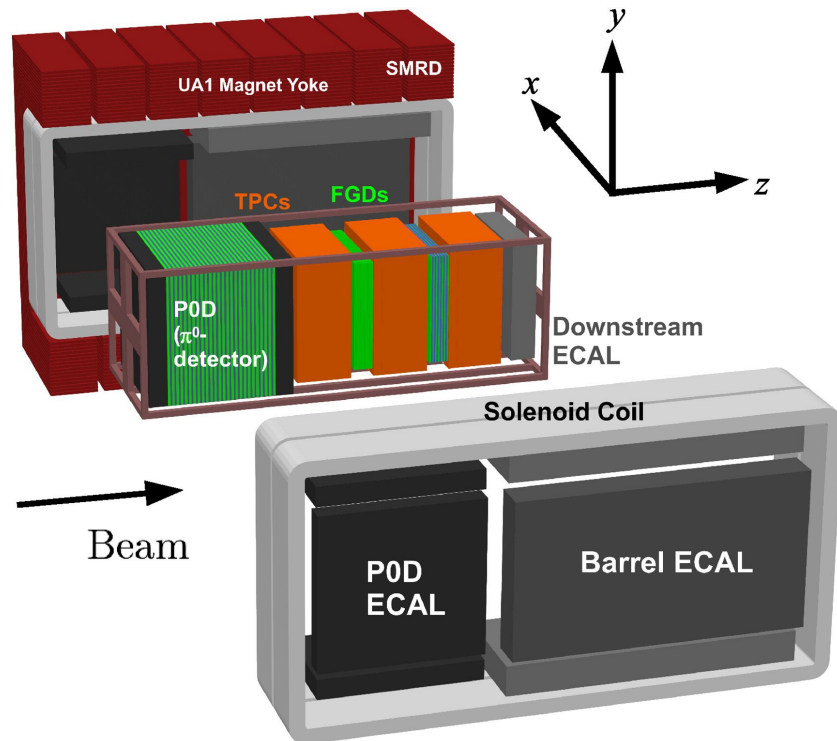


Figure 3.9: The components of the ND280 detector. The neutrino beam travels from left to right. Taken from [118].

⁸⁰² As illustrated in Figure 3.9, the ND280 detector consists of several sub-detectors.
⁸⁰³ The most important part of the detector for this analysis is the tracker region. This is
⁸⁰⁴ comprised of two time projection chambers (TPCs) sandwiched between three fine
⁸⁰⁵ grain detectors (FGDs). The FGDs contain both hydrocarbon plastics and water tar-
⁸⁰⁶ gets for neutrino interactions and provide track reconstruction near the interaction
⁸⁰⁷ vertex. The emitted charged particles can then propagate into the TPCs which pro-
⁸⁰⁸ vide particle identification and momentum reconstruction. The FGDs and TPCs are
⁸⁰⁹ further described in subsubsection 3.2.2.1 and subsubsection 3.2.2.2 respectively. The

810 electromagnetic calorimeter (ECAL) encapsulates the tracker region alongside the π^0
811 detector (P0D). The ECAL measures the deposited energy from photons emitted from
812 interactions within the FGD. The P0D constrains the cross-section of neutral current
813 interactions which generate neutral pions, which is one of the largest backgrounds in
814 the electron neutrino appearance oscillation channel. The P0D and ECAL detectors
815 are detailed in subsubsection 3.2.2.3 and subsubsection 3.2.2.4 respectively. The entire
816 detector is located within a large **yolk yoke** magnet which produces a 0.2T magnetic
817 field. This design of the magnet also includes a scintillating detector called the side
818 muon range detector (SMRD) which is used to track high-angle muons as well as
819 acting as a cosmic veto. The SMRD is described in subsubsection 3.2.2.5.

820 **3.2.2.1 Fine Grained Detectors**

821 The T2K tracker region is comprised of two fine grained detectors (FGD) and three
822 Time Projection Chambers (TPC). A detailed description of the FGD design, construc-
823 tion, and assembly is found in [123] and summarised below. The FGDs are the primary
824 target for neutrino interactions with a mass of 1.1 tonnes per FGD. Alongside this,
825 the FGDs are designed to be able to track short-range particles which do not exit the
826 FGD. Typically, short-range particles are low momentum and are observed as tracks
827 that deposit a large amount of energy per unit length. This means the FGD needs
828 good granularity to resolve these particles. The FGDs have the best timing resolution
829 ($\sim 3\text{ns}$) of any of the sub-detectors of the ND280 detector. As such, the FGDs are used
830 for time of flight measurements to **determine distinguish** forward going positively
831 charged particles from backward going negatively charged particles. Finally, any
832 tracks which pass through multiple sub-detectors are required to be track matched to
833 the FGD.

Both FGDs are made from square scintillator planes of side length 186cm and width 2.02cm. Each plane consists of two layers of 192 scintillator bars in an X or Y orientation. A wavelength shifting fiber is threaded through the center of each bar and is read out by a multi-pixel photon counter (MPPC). FGD1 is the most upstream of the two FGDs and contains 15 planes of carbon plastic scintillator which is a common target in external neutrino scattering data. As the far detector is a pure water target, 7 of the 15 scintillator planes in FGD2 have been replaced with a hybrid water-scintillator target. Due to the complexity of the nucleus, nuclear effects can not be extrapolated between different nuclei. Therefore having the ability to take data on one target which is the same as external data and another target which is the same as the far detector target is beneficial for reliable model parameter estimates.

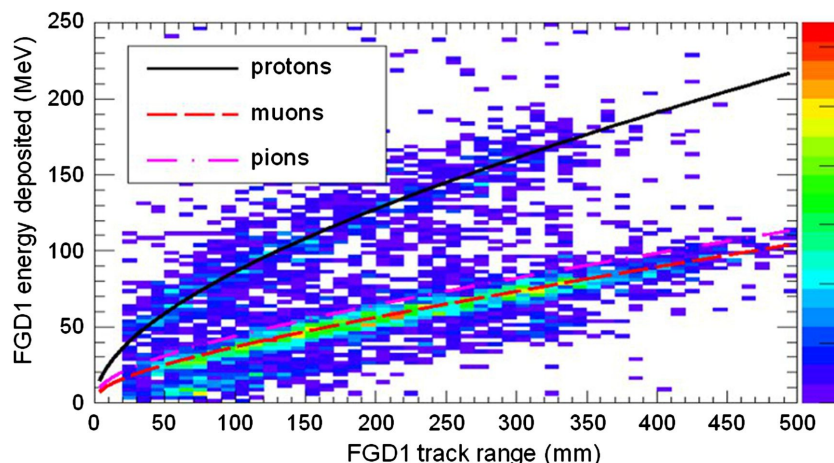


Figure 3.10: Comparison of data to Monte Carlo prediction of integrated deposited energy as a function of track length for particles that stopped in FGD1. Taken from [123].

The integrated deposited energy is used for particle identification. The FGD can distinguish protons from other charged particles by comparing the integrated deposited energy from data to Monte Carlo prediction as seen in Figure 3.10.

⁸⁴⁸ **3.2.2.2 Time Projection Chambers**

⁸⁴⁹ The majority of particle identification and momentum measurements within ND280
⁸⁵⁰ are provided by three Time Projection Chambers (TPCs) [124]. The TPCs are located
⁸⁵¹ on either side of the FGDs. They are located inside of the magnetic field meaning the
⁸⁵² momentum of a charged particle can be determined from the bending of the track.

⁸⁵³ Each TPC module consists of two gas-tight boxes, as shown in Figure 3.11, which
⁸⁵⁴ are made of non-magnetic material. The outer box is filled with CO₂ which acts as
⁸⁵⁵ an electrical insulator between the inner box and the ground. The inner box forms
⁸⁵⁶ the field cage which produces a uniform electric drift field of $\sim 275\text{V/cm}$ and **is filled**
⁸⁵⁷ **with** an argon gas mixture. Charged particles moving through this gas mixture ionize
⁸⁵⁸ the gas **mixture. The and the** ionised charge is drifted towards micromegas detectors
⁸⁵⁹ which measure the ionization charge. The time and position information in the readout
⁸⁶⁰ allows a three-dimensional image of the neutrino interaction.

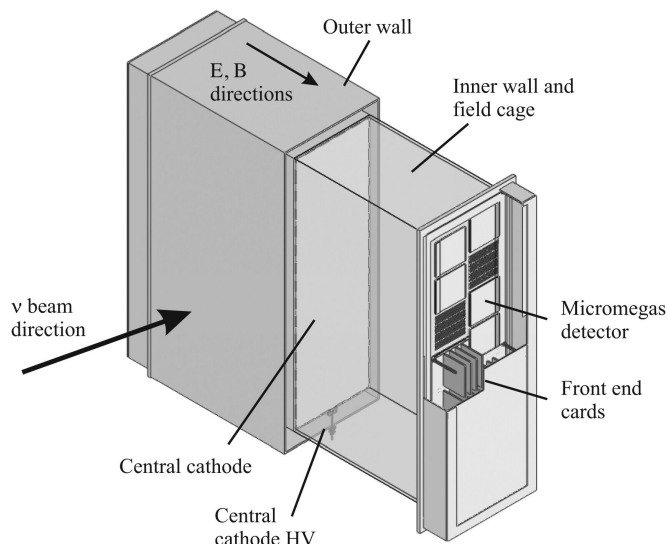


Figure 3.11: Schematic design of a Time Projection Chamber detector. Taken from [124].

⁸⁶¹ The particle identification of tracks that pass through the TPCs is performed using
⁸⁶² dE/dx measurements. Figure 3.12 illustrates the data to Monte Carlo distributions

863 of the energy lost by a charged particle passing through the TPC as a function of the
 864 reconstructed particle momentum. The resolution is $7.8 \pm 0.2\%$ meaning that electrons
 865 and muons can be distinguished. This allows reliable measurements of the intrinsic ν_e
 866 component of the beam.

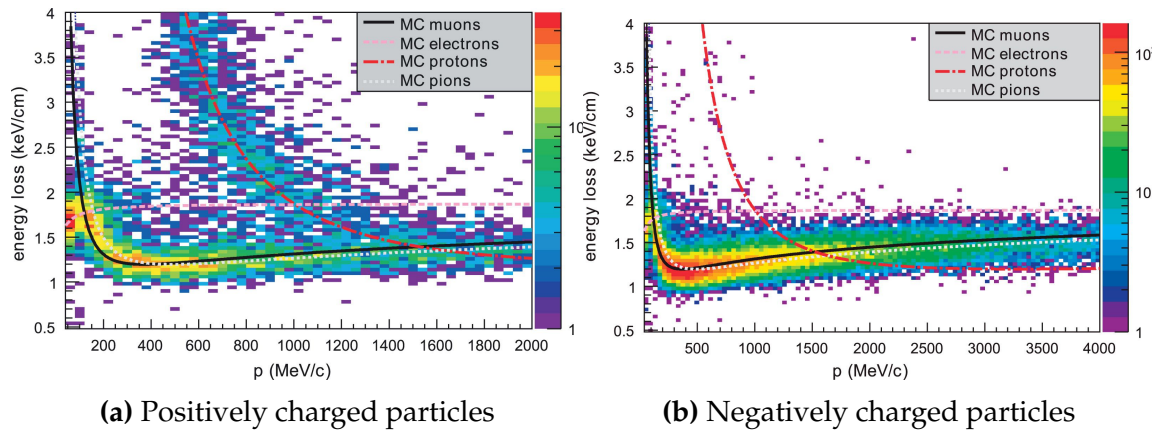


Figure 3.12: The distribution of energy loss as a function of reconstructed momentum for charged particles passing through the TPC, comparing data to Monte Carlo prediction. Taken from [124].

867 3.2.2.3 π^0 Detector

868 If one of the γ -rays from a $\pi^0 \rightarrow 2\gamma$ decay is missed at the far detector, the reconstruc-
 869 tion will determine that event to be **electron-like a charge current ν_e -like event**. This
 870 is one of the main backgrounds hindering the electron neutrino appearance searches.
 871 **Therefore, the The** π^0 detector (P0D) measures the cross-section of the neutral current
 872 induced neutral pion production on a water target **to constrain this background**.

873 The P0D is a cube of approximately 2.5m length **.The P0D consists consisting**
 874 of layers of scintillating bars, brass and lead sheets, and water bags as illustrated in
 875 Figure 3.13. Two electromagnetic calorimeters are positioned at the most upstream
 876 and most downstream position in the sub-detector and the water target is situated in
 877 between them. The scintillator layers are built from two triangular bars orientated
 878 in opposite directions to form a rectangular layer. Each triangular scintillator bar is

879 threaded with optical fiber which is read out by MPPCs. The high-Z brass and lead
 880 regions produce electron showers from the photons emitted in π^0 decay.

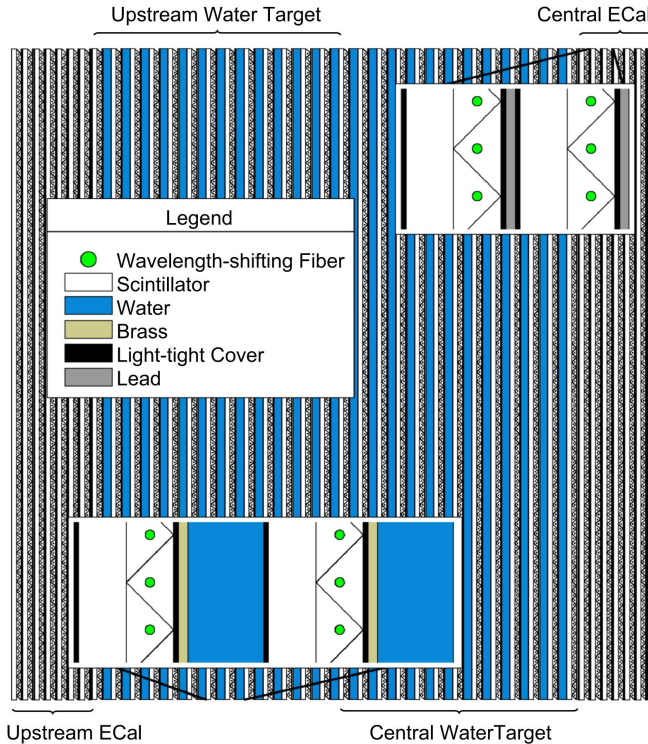


Figure 3.13: A schematic of the P0D side-view. Taken from [125].

881 The sub-detector can generate measurements of NC1 π^0 cross-sections on a water
 882 target by measuring the event rate both with and without the water target, with the
 883 cross-section on a water target being determined as the difference. The total active
 884 mass is 16.1 tonnes when filled with water and 13.3 tonnes when empty.

885 3.2.2.4 Electromagnetic Calorimeter

886 The electromagnetic calorimeter [126] (ECal) encapsulates the P0D and tracking sub-
 887 detectors. Its primary purpose is to aid π^0 reconstruction from any interaction in
 888 the tracker. To do this, it measures the energy and direction of photon showers from
 889 $\pi^0 \rightarrow 2\gamma$ decay. It can also distinguish pion and muon tracks depending on the shape
 890 of the photon shower deposited.

891 The ECal is comprised of three sections; the P0D ECal which surrounds the P0D,
892 the barrel ECal which encompasses the tracking region, and the downstream ECal
893 which is situated downstream of the tracker region. The barrel and downstream
894 ECals are tracking calorimeters that focus on electromagnetic showers from high-angle
895 particles emitted from the tracking sub-detectors. Particularly in the TPC, high-angle
896 tracks (those which travel perpendicularly to the beam-axis) can travel along a single
897 scintillator bar resulting in very few hits. The width of the barrel and downstream
898 ECal corresponds to ~ 11 electron radiation lengths to ensure ~~~50% of the energy~~
899 ~~of the π^0 is contained a significant amount of the π^0 energy is contained~~. As the
900 P0D has its own calorimetry which reconstructs showers, the P0D ECal determines
901 the energy which escapes the P0D.

902 Each ECal is constructed of multiple layers of scintillating bars sandwiched between
903 lead sheets. The scintillating bars are threaded with optical fiber and read out by
904 MPPCs. Each sequential layer of the scintillator is orientated perpendicular to the
905 previous which allows a ~~two-dimensional readout, which when temporal, information is included results in three-dimension event displays three dimensional event displays~~. The target mass of the P0D ECal, barrel ECal, and downstream ECal are 1.50,
906 4.80 and 6.62 tonnes respectively.

909 3.2.2.5 Side Muon Range Detector

910 As illustrated in Figure 3.9, the ECal, FGDs, P0D, and TPCs are enclosed within the
911 UA1 magnet. Originally designed for the NOMAD [127] experiment and reconditioned
912 for use in the T2K experiment [128], the UA1 magnet provides a uniform horizontal
913 magnetic field of ~~0.2 ± 2 × 10⁻⁴T~~ 0.2T with an uncertainty of 2×10^{-4} T.

914 Built into the UA1 magnet, the side muon range detector (SMRD) [129] monitors
915 high-energy muons which leave the tracking region and permeate through the ECal.
916 It additionally acts as a cosmic muon veto and trigger.

917 3.2.3 The Interactive Neutrino GRID

918 The Interactive Neutrino GRID (INGRID) detector is situated within the same “pit” as
919 the other near detectors. It is aligned with the beam in the “on-axis” position and mea-
920 sures the beam direction, spread, and intensity. The detector was originally designed
921 with 16 identical modules [118] (two modules have since been decommissioned) and a
922 “proton” module. The design of the detector is cross-shaped with length and height
923 10m × 10m as illustrated in Figure 3.14.

924 Each module is composed of iron sheets interlaced with eleven tracking scintillator
925 planes for a total target mass of 7.1 tonnes per module. The scintillator design is an X-Y
926 pattern of 24 bars in both orientations, where each bar contains wave-length shifting
927 fibers which are connected to multi-pixel photon counters (MPPCs). ~~The MPPCs con-~~
928 ~~vert detected photons into electrical signals via photodiodes. This is then read out~~
929 ~~by Trip-T front-end electronics and passed to the readout merging modules along~~
930 ~~with timing information from the clock module.~~ Each module is encapsulated inside
931 veto planes to aid the rejection of charged particles entering the module.

932 The proton module is different from the other modules in that it consists of entirely
933 scintillator planes with no iron target. The scintillator bars are also smaller than those
934 used in the other modules to increase the granularity of the detector and improve
935 tracking capabilities. The module sits in the center of the beamline and is designed to
936 give precise measurements of quasi-elastic charged current interactions to evaluate
937 the performance of the Monte Carlo simulation of the beamline.

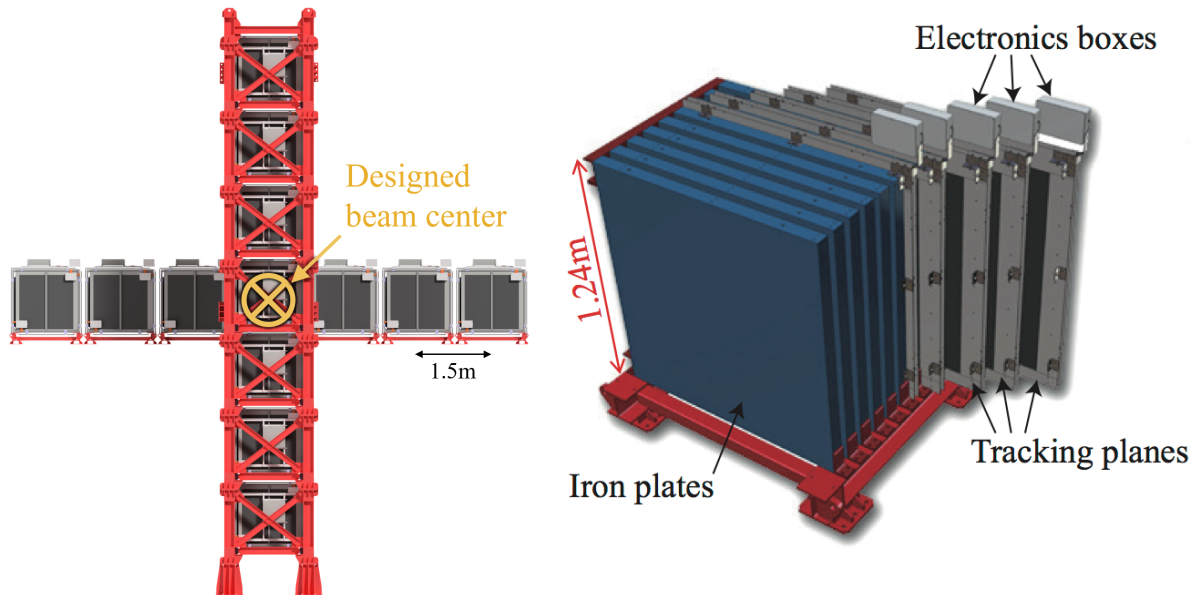


Figure 3.14: Left panel: The Interactive Neutrino GRID on-axis Detector. 14 modules are arranged in a cross-shape configuration, with the center modules being directly aligned with the on-axis beam. Right panel: The layout of a single module of the INGRID detector. Both figures are recreated from [118].

938 The INGRID detector can measure the beam direction to an uncertainty of 0.4mrad

939 and the beam center within a resolution of 10cm [118]. The beam direction in both the

940 vertical and horizontal directions is discussed in [130] and it is found to be in good

941 agreement with the MUMON monitor described in subsection 3.2.1.

942 **Chapter 4**

943 **Bayesian Statistics and Markov Chain
944 Monte Carlo Techniques**

945 ~~The analysis throughout this thesis is based upon~~ This thesis presents a Bayesian
946 oscillation analysis. To extract the oscillation parameters, a Markov Chain Monte
947 Carlo (MCMC) method is used. This chapter explains the theory of how parameter
948 estimates can be determined using this technique and condenses the material found in
949 the literature [131–134].

950 The oscillation parameter determination presented within this thesis is built upon
951 a ~~a simultaneous fit to the near detector, far detector beam, and atmospheric neutrino data~~
952 ~~a simultaneous fit to neutrino beam data in the near detector, beam data~~
953 ~~at SK and atmospheric data at SK~~. In total, there are four oscillation parameters of
954 interest ($\sin^2(\theta_{23})$, $\sin^2(\theta_{13})$, Δm_{23}^2 , and δ_{CP}), two oscillation parameters to which
955 this study will not be sensitive ($\sin^2(\theta_{12})$, Δm_{12}^2) and many nuisance parameters
956 that control the systematic uncertainty models invoked within this study. ~~The systematic~~
957 ~~uncertainties can be grouped into categories depending on how they are~~
958 ~~defined: 574 bin-normalisations due to the near detector response, 45 bin-normali-~~
959 ~~sations to describe the far detector response to neutrino beam events, 27 parameters~~
960 ~~to describe the detector response to atmospheric neutrino events, 100 to model the~~
961 ~~bin-normalisation due to beam flux uncertainties, 18 which model the atmospheric~~
962 ~~flux uncertainties, and 87 to describe the correlated cross-section model. An alter-~~
963 ~~native parameterisation, where the far detector response is correlated between the~~

964 ~~beam and atmospheric samples, replaces the bin normalisation parameters with~~
 965 ~~224 shift and smear systematics. Section Link to Systematics Chapter describes the~~
 966 ~~systematic model in more depth.~~

967 The MCMC technique generates a multi-dimensional probability distribution across
 968 all of the model parameters used in the fit. To determine the parameter estimate of a
 969 single parameter, this multi-dimensional object is integrated over all other parameters.
 970 This process is called Marginalisation and is further described in subsection 4.3.1.
 971 Monte Carlo techniques approximate the probability distribution of each parameter
 972 within the limit of generating infinite samples. As ever, generating a large number of
 973 samples is time and resource-dependent. Therefore, an MCMC technique is utilised
 974 within this analysis to reduce the required number of steps to sufficiently sample the
 975 parameter space. This technique is described in further detail in subsection 4.2.1.

976 4.1 Bayesian Statistics

977 ~~According to Bayesian Inference, observables and parameters of a statistical model~~
 978 ~~are treated on an equal footing. To estimate model parameters $\vec{\theta}$ from some data~~
 979 ~~D , one needs to define the joint probability distribution $P(D|\vec{\theta})$ which Bayesian~~
 980 ~~inference treats observable data, D , and model parameters, $\vec{\theta}$, on equal footing such~~
 981 ~~that a probability model of both data and parameters is required. This is the joint~~
 982 ~~probability distribution $P(D, \vec{\theta})$ and~~ can be described ~~as by~~ the prior distribution for
 983 model parameters $P(\vec{\theta})$ and the likelihood of the data given the model parameters
 984 $P(D|\vec{\theta})$,

$$P(D, \vec{\theta}) = P(D|\vec{\theta})P(\vec{\theta}). \quad (4.1)$$

The prior distribution, $P(\vec{\theta})$, describes all previous knowledge about the parameters within the model. For example, if the risk of developing health problems is known to increase with age, the prior distribution would describe the increase. For the purpose of this analysis, the prior distribution is typically the best-fit values taken from external data measurements with a Gaussian uncertainty. The prior distribution can also contain correlations between model parameters. In an analysis using Monte Carlo techniques, the likelihood of measuring some data assuming some set of model parameters is calculated by comparing the Monte Carlo prediction generated at that particular set of model parameters to the data.

It is parameter estimation that is important for this analysis and as such, we apply Bayes' theorem [135] to calculate the probability for each parameter to have a certain value given the observed data, $P(\vec{\theta}|D)$, which is known as the posterior distribution (often termed the posterior). This can be expressed as

$$P(\vec{\theta}|D) = \frac{P(D|\vec{\theta})P(\vec{\theta})}{\int P(D|\vec{\theta})P(\vec{\theta})d\vec{\theta}}. \quad (4.2)$$

The denominator in Equation 4.2 is the integral of the joint probability distribution over all values of all parameters used within the fit. For brevity, we say that the posterior distribution is

$$P(\vec{\theta}|D) \propto P(D|\vec{\theta})P(\vec{\theta}). \quad (4.3)$$

In subsection 4.3.1, we see that for the cases used within this analysis, it is reasonable to know the posterior to some normalisation constant.

1003 4.2 Monte Carlo Simulation

1004 Monte Carlo techniques are used to numerically solve a complex problem that does
1005 not necessarily have an analytical solution. These techniques rely on building a large
1006 ensemble of samples from an unknown distribution and then using the ensemble to
1007 approximate the properties of the distribution.

1008 An example that uses Monte Carlo techniques is to calculate the area underneath
1009 a curve. For example, take the problem of calculating the area under a straight line
1010 with gradient $M = 0.4$ and intercept $C = 1.0$. Analytically, one can calculate the area
1011 under the line is equal to 30 units for $0 \leq x \leq 10$. Using Monte Carlo techniques,
1012 one can calculate the area under this line by throwing many random values for the x
1013 and y components of each sample and then calculating whether that point falls below
1014 the line. The area can then be calculated by the ratio of points below the line to the
1015 total number of samples thrown multiplied by the total area in which samples were
1016 scattered. The study is shown in Figure 4.1 highlights this technique and finds the area
1017 under the curve to be 29.9 compared to an analytical solution of 30.0. The deviation
1018 of the numerical to analytical solution can be attributed to the number of samples
1019 used in the study. The accuracy of the approximation in which the properties of the
1020 Monte Carlo samples replicate those of the desired distribution is dependent on the
1021 number of samples used. Replicating this study with a differing number of Monte
1022 Carlo samples used in each study (As shown in Figure 4.2) highlights how the Monte
1023 Carlo techniques are only accurate within the limit of a high number of samples.

1024 Whilst the above example has an analytical solution, these techniques are just as
1025 applicable to complex solutions. Clearly, any numerical solution is only as useful as its
1026 efficiency. As discussed, the accuracy of the Monte Carlo technique is dependent upon
1027 the number of samples generated to approximate the properties of the distribution.

Furthermore, if the positions at which the samples are evaluated are not ‘cleverly’ picked, the efficiency of the Monte Carlo technique significantly drops. Given the example in Figure 4.1, if the region in which the samples are scattered significantly extends passed the region of interest, many calculations will be calculated but do not add to the ability of the Monte Carlo technique to achieve the correct result. For instance, any sample evaluated at a $y \geq 5$ could be removed without affecting the final result. This does bring in an aspect of the ‘chicken and egg’ problem in that to achieve efficient sampling, one needs to know the distribution beforehand.

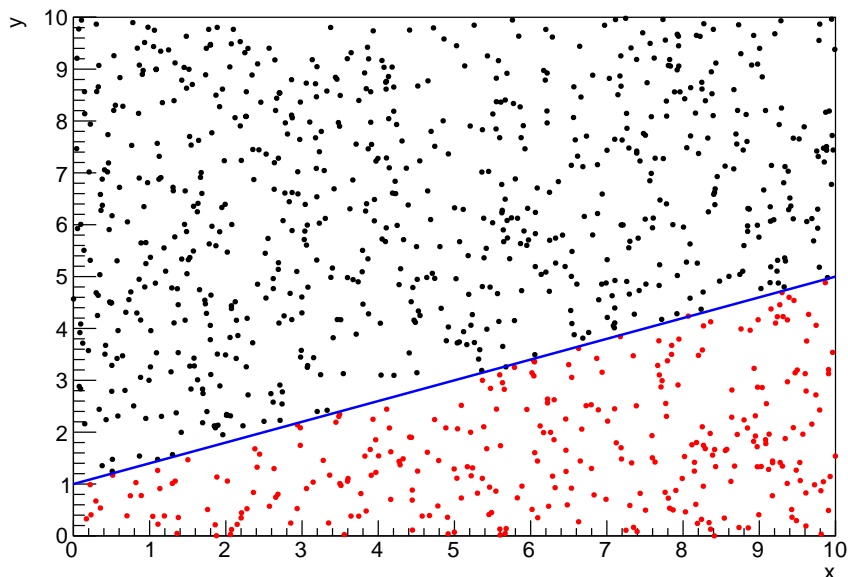


Figure 4.1: Example of using Monte Carlo techniques to find the area under the blue line. The gradient and intercept of the line are 0.4 and 1.0 respectively. The area found to be under the curve using one thousand samples is 29.9 units.

4.2.1 Markov Chain Monte Carlo

This analysis utilises a multi-dimensional probability distribution, with some dimensions being significantly more constrained than others. This could be from prior knowledge of parameter distributions from external data or un-physical regions in

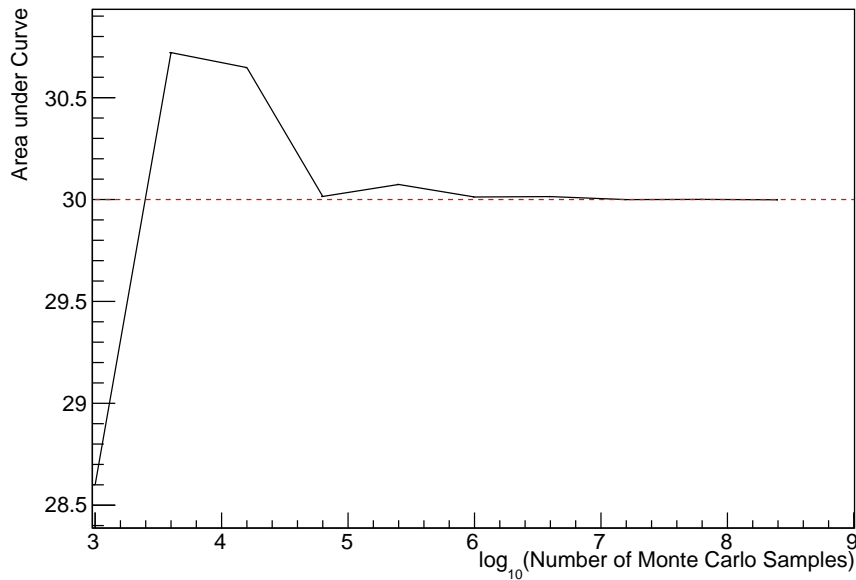


Figure 4.2: The area under a line of gradient 0.4 and intercept 1.0 for the range $0 \leq x \leq 10$ as calculated using Monte Carlo techniques as a function of the number of samples used in each repetition. The analytical solution to the area is 30 units as given by the red line.

which parameters can not exist. Consequently, the Monte Carlo techniques used need to be as efficient as possible. For this analysis, the Markov Chain Monte Carlo (MCMC) technique is chosen. An MCMC technique is a Monte Carlo technique that uses a Markov chain to select which points at which to sample the parameter distribution. This technique performs a semi-random stochastic walk through the allowable parameter space. This builds a posterior distribution which has the property that the density of sampled points is proportional to the probability density of that parameter. This does mean that the samples produced by this technique are not statistically independent but they will cover the space of the distribution.

A Markov chain functions by selecting the position of step \vec{x}_{i+1} based on the position of \vec{x}_i . The space in which the Markov chain selects samples is dependent upon the total number of parameters utilised within the fit, where a discrete point in this space is described by the N-dimensional space \vec{x} . In a perfectly operating Markov chain, the position of the next step depends solely on the previous step and not on the

1054 further history of the chain (\vec{x}_0, \vec{x}_1 , etc.). However, in solving the multi-dimensionality
 1055 of the fit used within this analysis, each step becomes correlated with several of
 1056 the steps preceding itself. This behaviour is further explained in subsection 4.2.3.
 1057 Providing the MCMC chain is well optimised, it will begin to converge towards a
 1058 unique stationary distribution. The period between the chain's initial starting point
 1059 and the convergence to the unique stationary distribution is colloquially known as the
 1060 burn-in period. This is discussed further in subsection 4.2.3. Once the chain reaches
 1061 the stationary distribution, all points sampled after that point will look like samples
 1062 from that distribution.

1063 Further details of the theories underpinning MCMC techniques are discussed
 1064 in [132] but can be summarised by the requirement that the chain satisfies the three
 1065 'regularity conditions':

- 1066 • Irreducibility: From every position in the parameter space \vec{x} , there must exist a
 1067 non-zero probability for every other position in the parameter space to be reached.
- 1068 • Recurrence: Once the chain arrives at the stationary distribution, every step fol-
 1069 lowing from that position must be samples from the same stationary distribution.
- 1070 • Aperiodicity: The chain must not repeat the same sequence of steps at any point
 1071 throughout the sampling period.

1072 The output of the chain after burn-in (ie. the sampled points after the chain
 1073 has reached the stationary distribution) can be used to approximate the posterior
 1074 distribution and model parameters $\vec{\theta}$. To achieve the requirement that the unique
 1075 stationary distribution found by the chain be the posterior distribution, one can use
 1076 the Metropolis-Hastings algorithm. This guides the stochastic process depending on
 1077 the likelihood of the current proposed step compared to that of the previous step.
 1078 Implementation and other details of this technique are discussed in subsection 4.2.2.

1079 4.2.2 Metropolis-Hastings Algorithm

1080 As a requirement for MCMCs, the Markov chain implemented in this technique must
 1081 have a unique stationary distribution that is equivalent to the posterior distribution.
 1082 To ensure this requirement and that the regularity conditions are met, this analysis
 1083 utilises the Metropolis-Hastings (MH) algorithm [136,137]. For the i^{th} step in the chain,
 1084 the MH algorithm determines the position in the parameter space to which the chain
 1085 moves to based on the current step, \vec{x}_i , and the proposed step, \vec{y}_{i+1} . The proposed step
 1086 is randomly selected from some proposal function $f(\vec{x}_{i+1}|\vec{x}_i)$, which depends solely
 1087 on the current step (ie. not the further history of the chain). The next step in the chain
 1088 \vec{x}_{i+1} can be either the current step or the proposed step determined by whether the
 1089 proposed step is accepted or rejected. To decide if the proposed step is selected, the
 1090 acceptance probability, $\alpha(\vec{x}_i, \vec{y}_i)$, is calculated as

$$\alpha(\vec{x}_i, \vec{y}_{i+1}) = \min\left(1, \frac{P(\vec{y}_{i+1}|D)f(\vec{x}_i|\vec{y}_{i+1})}{P(\vec{x}_i|D)f(\vec{y}_{i+1}|\vec{x}_i)}\right). \quad (4.4)$$

1091 Where $P(\vec{y}_{i+1}|D)$ is the posterior distribution as introduced in section 4.1. To
 1092 simplify this calculation, the proposal function is required to be symmetric such that
 1093 $f(\vec{x}_i|\vec{y}_{i+1}) = f(\vec{y}_{i+1}|\vec{x}_i)$. In practice, a multi-variate Gaussian distribution is used to
 1094 throw parameter proposals from. This reduces Equation 4.4 to

$$\alpha(\vec{x}_i, \vec{y}_{i+1}) = \min\left(1, \frac{P(\vec{y}_{i+1}|D)}{P(\vec{x}_i|D)}\right). \quad (4.5)$$

After calculating this quantity, a random number, β , is generated uniformly between 0 and 1. If $\beta \leq \alpha(\vec{x}_i, \vec{y}_{i+1})$, the proposed step is accepted. Otherwise, the chain sets the next step equal to the current step and this procedure is repeated. This can be interpreted as if the posterior probability of the proposed step is greater than that of the current step, ($P(\vec{y}_{i+1}|D) \geq P(\vec{x}_i|D)$), the proposed step will always be accepted. If the opposite is true, ($P(\vec{y}_{i+1}|D) \leq P(\vec{x}_i|D)$), the proposed step will be accepted with probability $P(\vec{x}_i|D)/P(\vec{y}_{i+1}|D)$. This ensures that the Markov chain does not get trapped in any local minima in the potentially non-Gaussian posterior distribution. The outcome of this technique is that the density of steps taken in a discrete region is directly proportional to the probability density in that region.

4.2.3 MCMC Optimisation

As discussed in subsection 4.2.2, the proposal function invoked within the MH algorithm can take any form and the chain will still converge to the stationary distribution. ~~As discussed in Link to Analysis Strategy Section, this analysis performs the Monte Carlo reweighting on an event-by-event basis. This requires significant computational resources to perform a parameter fit At each set of proposed parameter values, a prediction of the same spectra has to be generated which requires significant computational resources.~~ Therefore, the number of steps taken before the unique stationary distribution is found should be minimised as only steps after convergence add information to the **fit oscillation analysis**. Furthermore, the chain should entirely cover the allowable parameter space to ensure that all values have been considered. Tuning the distance that the proposal function jumps between steps on a parameter-by-parameter basis can both minimise the length of the burn-in period and ensure that the correlation between step \vec{x}_i and \vec{x}_j is sufficiently small.

1119 The effect of changing the width of the proposal function is highlighted in Figure 4.3.
1120 Three scenarios, each with the same underlying stationary distribution (A Gaussian of
1121 width 1.0 and mean 0.), are presented. The only difference between the three scenarios
1122 is the width of the proposal function, colloquially known as the ‘step size σ ’. Each
1123 scenario starts at an initial parameter value of 10.0 which would be considered an
1124 extreme variation. For the case where $\sigma = 0.1$, it is clear to see that the chain takes
1125 a long time to reach the expected region of the parameter. This indicates that this
1126 chain would have a large burn-in period and does not converge to the stationary
1127 distribution until step ~ 500 . Furthermore, whilst the chain does move towards the
1128 expected region, each step is significantly correlated with the previous. Considering
1129 the case where $\sigma = 5.0$, the chain approaches the expected parameter region almost
1130 instantly meaning that the burn-in period is not significant. However, there are clearly
1131 large regions of steps where the chain does not move. This is likely due to the chain
1132 proposing steps in the tails of the distribution which have a low probability of being
1133 accepted. Consequently, this chain would take a significant number of steps to fully
1134 span the allowable parameter region. For the final scenario, where $\sigma = 0.5$, you can see
1135 a relatively small burn-in period of approximately 100 steps. Once the chain reaches
1136 the stationary distribution, it moves throughout the expected region of parameter
1137 values many times, sufficiently sampling the full parameter region. This example is a
1138 single parameter varying across a continuous distribution and does not fully reflect
1139 the difficulties in the many-hundred multi-variate parameter distribution used within
1140 this analysis. However, it does give a conceptual idea of the importance of selecting
1141 the proposal function and associated step size.

1142 As discussed, step size tuning directly correlates to the average step acceptance
1143 rate. If the step size is too small, many steps will be accepted but the chain moves
1144 slowly. If the opposite is true, many steps will be rejected as the chain proposes steps
1145 in the tails of the distribution. Discussion in [138] suggests that the ‘ideal’ acceptance

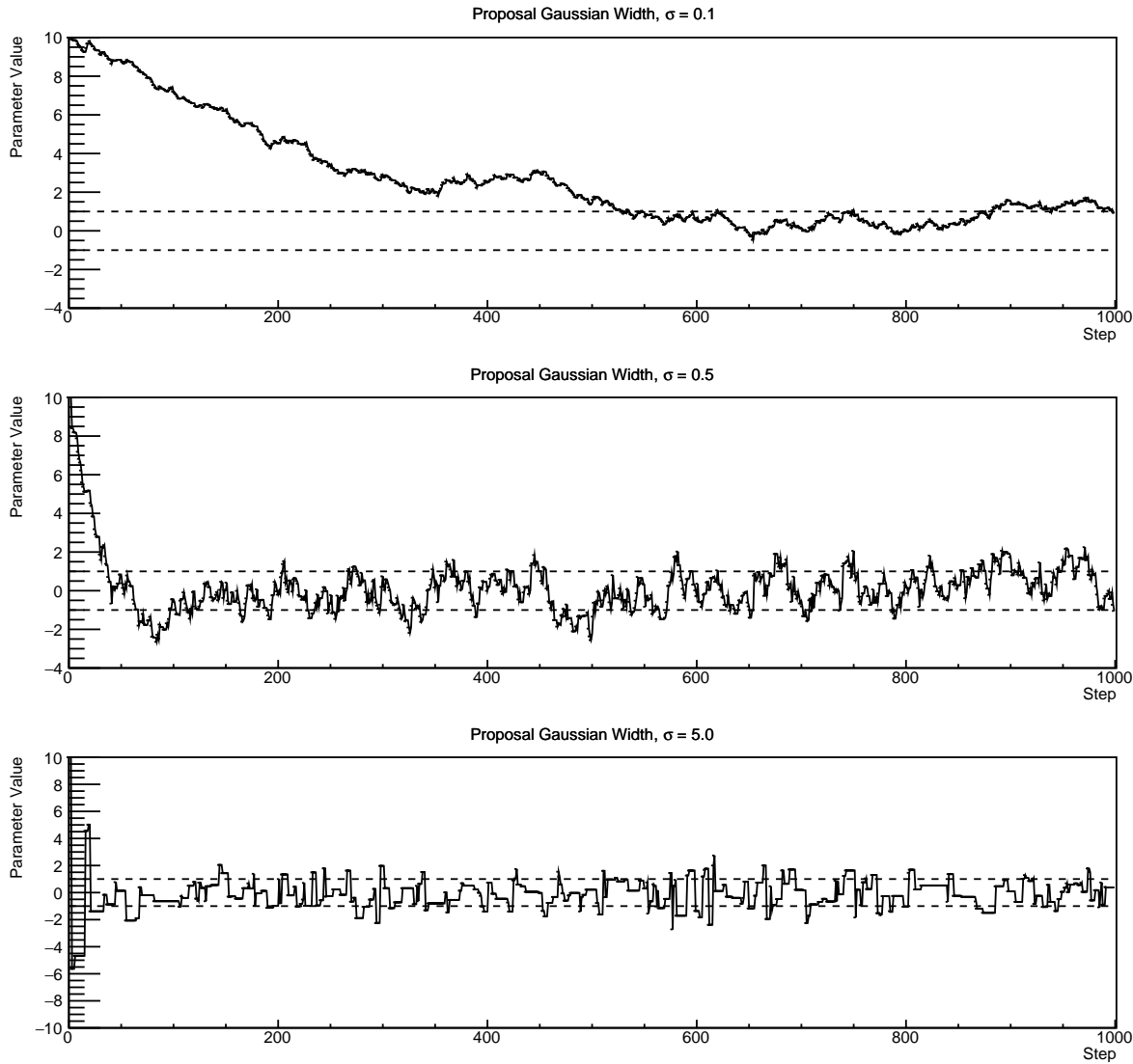


Figure 4.3: Three MCMC chains, each with a stationary distribution equal to a Gaussian centered at 0 and width 1 (As indicated by the black dotted lines). All of the chains use a Gaussian proposal function but have different widths (or ‘step size σ ’). The top panel has $\sigma = 0.1$, middle panel has $\sigma = 0.5$ and the bottom panel has $\sigma = 5.0$.

¹¹⁴⁶ rate of a high dimension MCMC chain should be approximately $\sim 25\%$. An “ideal”

¹¹⁴⁷ step size [138] of

$$\sigma = \frac{2.4}{N_p}, \quad (4.6)$$

1148 where N_p is the number of parameters included in the MCMC fit. However, the
 1149 complex correlations between systematics mean that some parameters have to be hand
 1150 tuned and many efforts have been taken to select a set of parameter-by-parameter step
 1151 sizes to approximately reach the ideal acceptance rate.

1152 Figure 4.3 highlights the likelihood as calculated by the fit in [DB: Link to AsimovA](#)
 1153 [Sensitivity Section](#) as a function of the number of steps in each chain. In practice,
 1154 many independent MCMC chains are run simultaneously to parallelise the task of
 1155 performing the fit. This figure overlays the distribution found in each chain. As seen,
 1156 the likelihood decreases from its initial value and converges towards a stationary
 1157 distribution after $\sim 1 \times 10^5$ steps. ~~Each fit (whether it be different asimov fits or data~~
~~fit) will have a different set of preferred parameter values which results in a differ-~~
~~ent stationary distribution. For each fit presented in this thesis, a burn-in period of~~
 ~~1×10^5 steps was found to be sufficient.~~

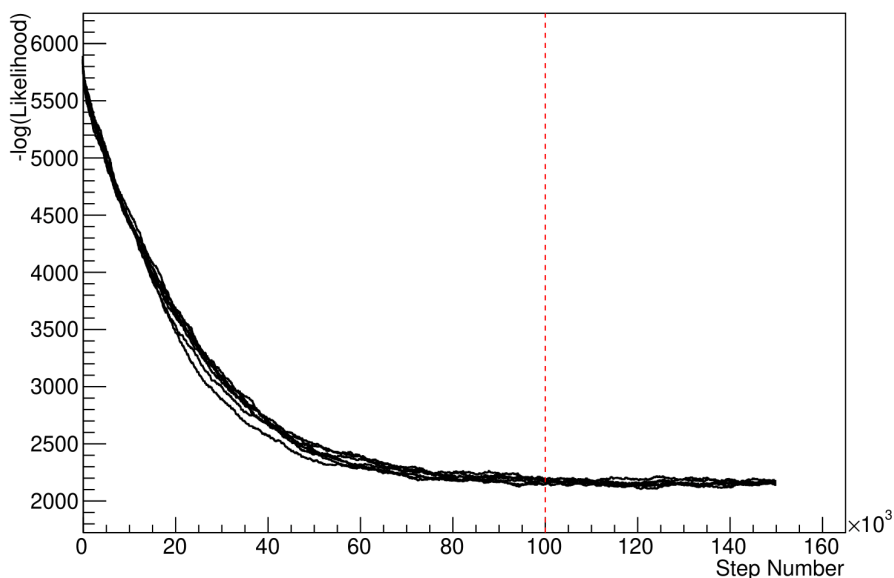


Figure 4.4: The log-likelihood from the fit detailed in [DB: Link to AsimovA](#) [Sensitivity Section](#) as a function of the number of steps accumulated in each fit. Many independent MCMC chains were run in parallel and overlaid on this plot. The red line indicates the 1×10^5 step burn-in period after which the log-likelihood becomes stable.

1161 Multiple configurations of this analysis have been performed throughout this
1162 thesis where different samples or systematics have been used. For all of these
1163 configurations, it was found that a burnin period of 1×10^5 was sufficient in all
1164 cases.

1165

4.3 Understanding the MCMC Results

1166 Whilst Link and Link describe how to interpret Bayesian statistics and explains the
1167 MCMC techniques used within this analysis, there is no mention of how to inter-
1168 pret the output of the chain. The previous sections have described how to generate
1169 the posterior probability distribution using Bayesian MCMC techniques. How-
1170 ever, this analysis focuses on oscillation parameter determination. The posterior
1171 distribution output from the chain is a high dimension object, with as many dimen-
1172 sions as there are parameters included in the fit oscillation analysis. However, this
1173 multi-dimensional object is difficult to conceptualize so parameter estimations are
1174 often presented in one or two-dimensional projections of this probability distribution.
1175 To do this, we invoke the marginalisation technique highlighted in subsection 4.3.1.

1176

4.3.1 Marginalisation

1177 The output of the MCMC chain is a highly dimensional probability distribution
1178 which is very difficult to interpret. From the standpoint of an oscillation analysis
1179 experiment, the one or two-dimensional ‘projections’ of the oscillation parameters of
1180 interest are most relevant. Despite this, the best fit values and uncertainties on the
1181 oscillation parameters of interest should correctly encapsulate the correlations to the
1182 other systematic uncertainties (colloquially called ‘nuisance’ parameters). For this joint
1183 beam and atmospheric analysis, the oscillation parameters of interest are $\sin^2(\theta_{23})$,

1184 $\sin^2(\theta_{13})$, Δm_{23}^2 , and δ_{CP} . All other parameters (Including the oscillation parameter
 1185 this fit is insensitive to) are deemed nuisance parameters. To generate these projections,
 1186 we rely upon integrating the posterior distribution over all nuisance parameters. This
 1187 is called marginalisation. A simple example of this technique is to imagine the scenario
 1188 where two coins are flipped. To determine the probability that the first coin returned
 1189 a ‘head’, the exact result of the second coin flip is disregarded and simply integrated
 1190 over. For the parameters of interest, $\vec{\theta}_i$, we can calculate the marginalised posterior by
 1191 integrating over the nuisance parameters, $\vec{\theta}_n$. In this case, Equation 4.2 becomes

$$P(\vec{\theta}_i|D) = \frac{\int P(D|\vec{\theta}_i, \vec{\theta}_n)P(\vec{\theta}_i, \vec{\theta}_n)d\vec{\theta}_n}{\int P(D|\vec{\theta})P(\vec{\theta})d\vec{\theta}} \quad (4.7)$$

1192 Where $P(\vec{\theta}_i, \vec{\theta}_n)$ encodes the prior knowledge about the uncertainty and correlations
 1193 between the parameters of interest and the nuisance parameters. In practice, this
 1194 is simply taking the one or two-dimensional projection of the multi-dimensional
 1195 probability distribution.

1196 Whilst in principle an easy solution to a complex problem, correlations between the
 1197 interesting and nuisance parameters can bias the marginalised results. A similar effect
 1198 is found when the parameters being marginalised over have non-Gaussian probability
 1199 distributions. For example, Figure 4.5 highlights the marginalisation bias in the
 1200 probability distribution found for a parameter when requiring a correlated parameter
 1201 to have a positive parameter value. Due to the complex nature of this oscillation
 1202 parameter fit presented in this thesis, there are **certainly** correlations occurring between
 1203 the oscillation parameters of interest and the other nuisance parameters included in
 1204 the fit.

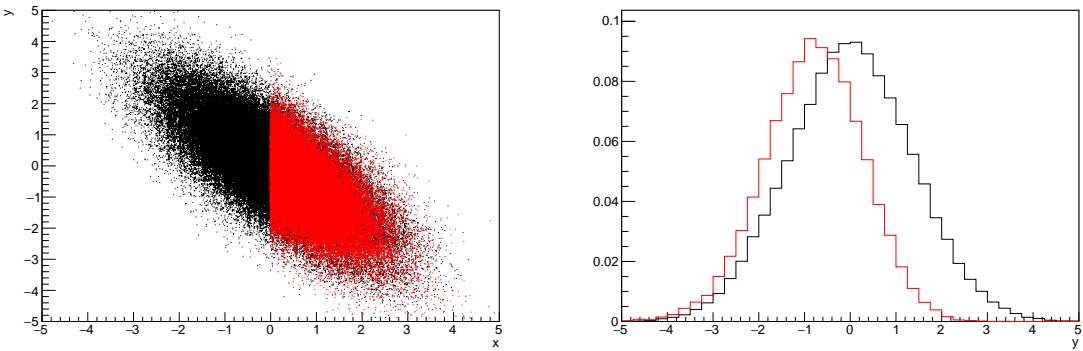


Figure 4.5: Left: The two dimensional probability distribution for two correlated parameters x and y . The red distribution shows the two dimensional probability distribution when $0 \leq x \leq 5$. Right: The marginalised probability distribution for the y parameter found when requiring the x to be bound between $-5 \leq x \leq 5$ for the black and red distribution, respectively.

1205 4.3.2 Parameter Estimation and Credible Intervals

1206 The purpose of this analysis is to determine the best fit values for the oscillation
 1207 parameters that the beam and atmospheric samples are sensitive to: $\sin^2(\theta_{23})$, $\sin^2(\theta_{13})$
 1208 , Δm_{23}^2 , and δ_{CP} . Typically, the results presented take the form of one or two-dimension
 1209 marginalised probability distributions for the appearance ($\sin^2(\theta_{13})$ and δ_{CP}) and
 1210 disappearance ($\sin^2(\theta_{23})$ and Δm_{23}^2) parameters. The posterior probability density
 1211 taken from the output MCMC chain is binned in these parameters. The parameter
 1212 best-fit point is then taken to be the value that has the highest posterior probability.
 1213 This is performed in both one and two-dimensional projections.

1214 However, the single best-fit point in a given parameter is not of much use on its
 1215 own. We would also like to determine the uncertainty, or credible interval, on that
 1216 best-fit point. The definition of the 1σ credible interval is that we have 68% belief that
 1217 the parameter is within those bounds. For a more generalised definition, the credible
 1218 interval is the region, R , of the posterior distribution that contains a specific fraction of
 1219 the total probability, such that

$$\int_R P(\theta|D)d\theta = \alpha \quad (4.8)$$

1220 Where θ is the parameter on which we calculate the credible interval. This technique
1221 then calculates the $\alpha \times 100\%$ credible interval.

1222 In practice, this analysis uses the highest posterior density (HPD) credible intervals
1223 which are calculated through the following method. First, the probability distribution
1224 is area-normalised such that it has an integrated area equal to 1.0. The bins of proba-
1225 bility are then summed from the highest to lowest until the sum exceeds the 1σ level
1226 (0.68 in this example). This process is repeated for a range of credible intervals, notably
1227 the 1σ , 2σ and 3σ along with other levels where the critical values for each level can
1228 be found in [139]. This process can be repeated for the two-dimensional probability
1229 distributions by creating two-dimensional contours of credible intervals rather than a
1230 one-dimensional result.

1231 4.3.3 Bayesian Model Comparisons

1232 Due to the matter resonance, this analysis has some sensitivity to the mass hierarchy
1233 of neutrino states (whether Δm_{23}^2 is positive or negative) and the octant of $\sin^2(\theta_{23})$
1234 . The Bayesian approach utilised within this analysis gives an intuitive method of
1235 model comparison by determining which hypothesis is most favourable. Taking the
1236 ratio of Equation 4.3 for the two hypotheses of normal hierarchy, NH , and inverted
1237 hierarchy, IH , gives

$$\frac{P(\vec{\theta}_{NH}|D)}{P(\vec{\theta}_{IH}|D)} = \frac{P(D|\vec{\theta}_{NH})}{P(D|\vec{\theta}_{IH})} \times \frac{P(\vec{\theta}_{NH})}{P(\vec{\theta}_{IH})}. \quad (4.9)$$

1238 The middle term defines the Bayes factor which is a data-driven interpretation of
 1239 how strong the data prefers one hierarchy to the other. For this analysis, equal priors
 1240 on both mass hierarchy hypotheses are chosen ($P(\vec{\theta}_{NH}) = P(\vec{\theta}_{IH}) = 0.5$). In practice,
 1241 the MCMC chain proposes a value of $|\Delta m_{23}^2|$ and then applies a 50% probability
 1242 that the value is sign flipped. Consequently, the Bayes factor can be calculated from
 1243 the ratio of the probability density in either hypothesis. This equates to counting the
 1244 number of steps taken in the normal and inverted hierarchies and taking the ratio. The
 1245 same approach can be taken to compare the upper octant (UO) compared to the lower
 1246 octant (LO) hypothesis of $\sin^2(\theta_{23})$.

1247 Whilst the value of the Bayes factor should always be shown, the Jeffreys scale [140]
 1248 (highlighted in Table 4.1) gives an indication of the strength of preference for one model
 1249 compared to the other. Other interpretations of the strength of preference of a model
 1250 exist, e.g. the Kass and Raferty Scale [141].

$\log_{10}(B_{AB})$	B_{AB}	Strength of Preference
< 0.0	< 1	No preference for hypothesis A (Supports hypothesis B)
$0.0 - 0.5$	$1.0 - 3.16$	Preference for hypothesis A is weak
$0.5 - 1.0$	$3.16 - 10.0$	Preference for hypothesis A is substantial
$1.0 - 1.5$	$10.0 - 31.6$	Preference for hypothesis A is strong
$1.5 - 2.0$	$31.6 - 100.0$	Preference for hypothesis A is very strong
> 2.0	> 100.0	Decisive preference for hypothesis A

Table 4.1: Jeffreys scale for strength of preference for two models A and B as a function of the calculated Bayes factor ($B_{AB} = B(A/B)$) between the two models [140]. The original scale is given in terms of $\log_{10}(B(A/B))$ but converted to linear scale for easy comparison throughout this thesis.

1251 4.3.4 Comparison of MCMC Output to Expectation

1252 ~~Whilst not important for the extraction of oscillation parameters, understanding~~
1253 ~~how the data constrains the model parameters is important to the understanding~~
1254 ~~of this analysis. To ensure the fit is performing well, a best-fit spectra is produced~~
1255 ~~using the posterior probability distribution and compared with the data, allowing~~
1256 ~~easy by-eye comparisons to be made.~~ A simple method of doing this is to perform a
1257 comparison in the fitting parameters (For instance, the reconstructed neutrino energy
1258 and lepton direction for T2K far detector beam samples) of the spectra generated by
1259 the MCMC chain to ‘data’. This ‘data’ could be true data or some variation of Monte
1260 Carlo prediction. This allows easy comparison of the MCMC probability distribution
1261 to the data. To perform this, N steps from the post burn-in MCMC chain are randomly
1262 selected (Where for all plots of this style in this thesis, $N = 3000$). From these, the
1263 Monte Carlo prediction at each step is generated by reweighting the model parameters
1264 to the values specified at that step. Due to the probability density being directly
1265 correlated with the density of steps in a certain region, parameter values close to the
1266 best fit value are most likely to be selected.

1267 In practice, for each bin of the fitting parameters has a probability distribution
1268 of event rates, with one entry per sampled MCMC step. This distribution is binned
1269 where the bin with the highest probability is selected as the mean and an error on
1270 the width of this probability distribution is calculated using the approach highlighted
1271 in subsection 4.3.2. Consequently, the best fit distribution in the fit parameter is not
1272 necessarily that which would be attained by reweighting the Monte Carlo prediction
1273 to the most probable parameter values.

1274 A similar study can be performed to illustrate the freedom of the model parameter
1275 space prior to the fit. This can be done by throwing parameter values from the prior

₁₂₇₆ uncertainty of each parameter. This becomes troublesome for parameters with no
₁₂₇₇ prior uncertainty as the range is technically infinite. Where applicable solutions to
₁₂₇₈ remove these have been addressed.

1279 **Chapter 5**

1280 **Simulation, Reconstruction, and Event
1281 Reduction**

1282 As a crucial part of the oscillation analysis, an accurate prediction of the expected
1283 neutrino spectrum at the far detector is required. This includes modeling the flux
1284 generation, neutrino interactions, and detector effects. All of the simulation packages
1285 required to do this are briefly described in section 5.1. The reconstruction of neutrino
1286 events inside the far detector, including the `fitQun` algorithm, is documented in
1287 section 5.2. This also includes data quality checks of the SK-V data which the author
1288 performed for the T2K oscillation analysis presented at Neutrino 2020 [80]. Finally,
1289 section 5.3 describes the steps taken in the SK detector to trigger on events of interest
1290 whilst removing the comparatively large rate of cosmic ray muon events.

1291 **5.1 Simulation**

1292 In order to generate a Monte Carlo prediction of the expected event rate at the far
1293 detector, all the processes in the beam and atmospheric flux, neutrino interaction, and
1294 detector need to be modeled. Each of these parts is individually modeled and each of
1295 them is detailed below.

1296 The beamline simulation consists of three distinct parts: the initial hadron inter-
1297 action modeled by FLUKA [142], the target station geometry and particle tracking

1298 performed by JNUBEAM, [143, 144] and any hadronic re-interactions simulated by
 1299 GCALOR [145]. The primary hadronic interactions are $O(10)\text{GeV}$, where FLUKA
 1300 matches external cross-section data better than GCALOR [146]. However, FLUKA
 1301 is not very adaptable so a small simulation is built to model the interactions in the
 1302 target and the output is then passed to JNUBEAM and GCALOR for propagation.
 1303 The hadronic interactions are tuned to data from the NA61/SHINE [147–149] and
 1304 HARP [150] experiments. The tuning is done by reweighting the FLUKA and GCALOR
 1305 predictions to match the external data multiplicity and cross-section measurements,
 1306 based on final state particle kinematics [146]. The culmination of this simulation
 1307 package generates the predicted flux for neutrino and antineutrino beam modes which
 1308 are illustrated in Figure 3.7.

1309 The atmospheric neutrino flux predictions are simulated by the HKKM model
 1310 [43, 45]. The primary cosmic ray flux is tuned to AMS [151] and BESS [152] data assum-
 1311 ing the US-standard atmosphere '76 [153] density profile and includes geomagnetic
 1312 field effects. The primary cosmic rays interact to generate pions and muons. The
 1313 interaction of these secondary particles to generate neutrinos is handled by DPMJET-
 1314 III [154] for energies above 32GeV and JAM [45, 155] for energies below that value **DB:**
 1315 **Question for Giles: Why different generators for above/below 32GeV?** These hadronic
 1316 interactions are tuned to BESS and L3 data [156, 157] using the same methodology
 1317 as the tuning of the beamline simulation. The energy and cosine zenith predictions
 1318 of $\nu_e, \bar{\nu}_e, \nu_\mu, \bar{\nu}_\mu$ flux are given in Figure 2.3 and Figure 2.5, respectively. The flux is
 1319 approximately symmetrical and peaked around the horizon ($\cos(\theta_Z) = 0.0$). This is be-
 1320 cause horizontally-going pions and kaons can travel further than their vertically-going
 1321 counterparts resulting in a larger probability of decaying to neutrinos. The symmetry
 1322 is broken in low-energy neutrinos due to geomagnetic effects, which modify the track
 1323 of the primary cosmic rays. Updates to the HKKM model are currently ongoing [158].

Once a flux prediction has been made for all three detectors, NEUT 5.4.0 [159, 160] models the interactions of the neutrinos in the detectors. For the purposes of this analysis, quasi-elastic (QE), meson exchange (MEC), single meson production (PROD), coherent pion production (COH), and deep inelastic scattering (DIS) interactions are simulated. These interaction categories can be further broken down by whether they were propagated via a W^\pm boson in Charged Current (CC) interactions or via a Z^0 boson in Neutral Current (NC) interactions. CC interactions have a charged lepton in the final state, which can be flavour-tagged in reconstruction to determine the flavour of the neutrino. In contrast, NC interactions have a neutrino in the final state so no flavour information can be determined from the observables left in the detector after an interaction. This is the reason why NC events are assumed to not oscillate within this analysis. Both CC and NC interactions are modeled for all the above interaction categories, other than MEC interactions which are only modeled for CC events. The SK detector is only sensitive to charged particles, so all charged current interactions are simulated whilst only neutral current processes that produce charged mesons (NCDIS, NCCOH, and NCProd) are modeled. NC MEC interactions can only produce charged particles through secondary re-interactions which is a low cross-section process.

As illustrated in Figure 5.1, CC QE interactions dominate the low-energy cross-section of neutrino interactions. The NEUT implementation adopts the Llewellyn Smith [161] model for neutrino-nucleus interactions, where the nuclear ground state of any bound nucleons (neutrino-oxygen interactions) is approximated by a spectral-function [162] model that simulates the effects of Fermi momentum and Pauli blocking. The cross-section of QE interactions are controlled by vector and axial-vector form factors parameterised by the BBBA05 [163] model and a dipole form factor with $M_A^{QE} = 1.21\text{GeV}$ fit to external data [164], respectively. NEUT implements the Valencia [165] model to simulate MEC events, where two nucleons and two holes in the nuclear target are produced (Often called 2p2h interactions).

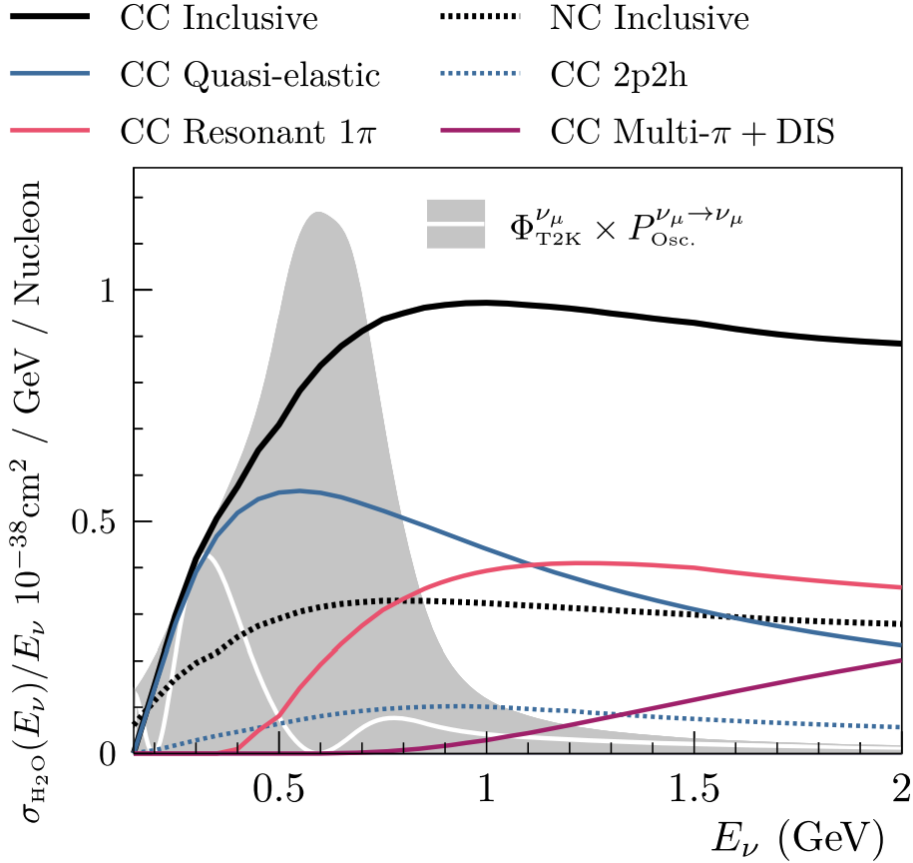


Figure 5.1: The NEUT prediction of the ν_μ -H₂O cross-section overlaid on the T2K ν_μ flux. The charged current (black, solid) and neutral current (black, dashed) inclusive, charged current quasi-elastic (blue, solid), charged current 2p2h (blue, dashed), charged current single pion production (pink), and charged current multi- π and DIS (Purple) cross-sections are illustrated. Figure taken from [159].

For neutrinos of energy $O(1)\text{GeV}$, PROD interactions become dominant. These predominantly produce charged and neutral pions although γ , kaon, and η production is also considered. To simulate these interactions, the Berger-Sehgal [166] model is implemented within NEUT. It simulates the excitation of a nucleon from a neutrino interaction, production of an intermediate baryon, and the consequential decay to a single meson or γ . Pions can also be produced through COH interactions, which occur when the incoming neutrino interacts with the entire oxygen nuclei target leaving a single pion outside of the nucleus. NEUT utilises the Berger-Sehgal [167] model to simulate these COH interactions.

¹³⁶⁰ DIS and multi- π producing interactions become the most dominant for energies
¹³⁶¹ $> O(5)\text{GeV}$. PYTHIA [168] is used to simulate any interaction with invariant mass,
¹³⁶² $W > 2\text{GeV}/c^2$, which produces at least one meson. For any interaction which produces
¹³⁶³ at least two mesons but has $W < 2\text{GeV}/c^2$, the Bronner model is invoked [169].
¹³⁶⁴ Both of these models use Parton distribution functions based on the Bodek-Yang
¹³⁶⁵ model [170–172].

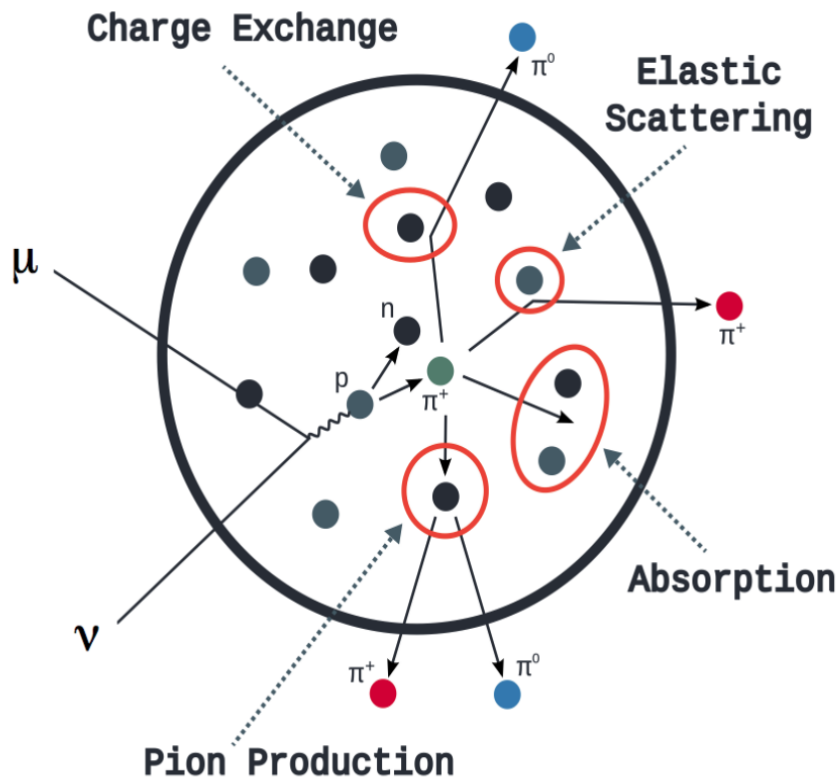


Figure 5.2: Illustration of the various processes which a pion can undergo before exiting the nucleus. Taken from [173].

¹³⁶⁶ Any pion which is produced within the nucleus can re-interact through final state
¹³⁶⁷ interactions before it exits, as illustrated by the scattering, absorption, production, and
¹³⁶⁸ exchange interactions in Figure 5.2. These re-interactions alter the observable particles
¹³⁶⁹ within the detector. For instance, if the charged pion from a CC PROD interaction is
¹³⁷⁰ absorbed, the observables would mimic a CC QE interaction. To simulate these effects,

1371 NEUT uses a semi-classical intranuclear cascade model [159]. This cascade functions by
1372 stepping the pion through the nucleus in fixed-length steps equivalent to $dx = R_N/100$,
1373 where R_N is the radius of the nucleus. At each step, the simulation allows the pion
1374 to interact through scattering, charged exchange, absorption, or production with an
1375 interaction-dependent probability calculated from a fit to external data [174]. This
1376 cascade continues until the pion is absorbed or exits the nucleus.

1377 Once the final state particle kinematics have been determined from NEUT, they
1378 are passed into the detector simulation. The near detectors, ND280 and INGRID, are
1379 simulated using a GEANT4 package [118,175] to simulate the detector geometry, particle
1380 tracking, and energy deposition. The response of the detectors is simulated using
1381 the elecSim package [118]. The far detector simulation is based upon the original
1382 Kamiokande experiment software which uses the GEANT3-based SKDETSIM [118,176]
1383 package. This controls the interactions of particles in the water as well as Cherenkov
1384 light production. The water quality and PMT calibration measurements detailed in
1385 subsection 3.1.2 are also used within this simulation to make accurate predictions of
1386 the detector response.

1387 5.2 Event Reconstruction at SK

1388 Any above Cherenkov threshold event which occurs in SK will be recorded by the
1389 PMT array, where each PMT records the time and accumulated charge. This recorded
1390 information is shown in event displays similar to those illustrated in Figure 5.3. To
1391 be useful for physics analyses, this series of PMT hit information needs to be recon-
1392 structed to determine the particle's identity and kinematics (or track parameters):
1393 four-vertex, direction, and momenta. This is because the charge and timing distribu-
1394 tion of photons generated by a particular particle in an event is dependent upon its

1395 initial kinematics. The concept of distinguishing electron and muon events is from the
1396 “fuzziness” of the ring. Muons are heavier and less affected by scattering or showering
1397 meaning they typically produce “crisp” rings. Electrons are more likely to interact
1398 via electromagnetic showering or scattering which results in larger variations of their
1399 direction from the initial direction. Consequently, electrons typically produce “fuzzier”
1400 rings compared to muons.

1401 For the purposes of this analysis, the `fitQun` reconstruction algorithm is utilised.
1402 Its core function is to compare a prediction of the accumulated charge and timing
1403 distribution from each PMT, generated for a particular particle identity and track
1404 parameters, to that observed in the neutrino event. It determines the preferred values
1405 by minimising a likelihood function which includes information from PMTs which
1406 were hit and those that were not hit. The `fitQun` algorithm improves upon the APFit
1407 reconstruction algorithm which has been used for many previous SK analyses. APFit
1408 fits the vertex from timing information and then fits the momentum and direction
1409 of the particle from PMT hits within a 43 deg Cherenkov cone (which assumes an
1410 ultra-relativistic particle). It then fits the particle identity once the track parameters
1411 have been fit. Conversely, `fitQun` performs a simultaneous fit of particle kinematics
1412 and identity, improving both the accuracy of the fit parameters and the rejection of
1413 neutral current π^0 events [177,178]. The `fitQun` algorithm is based on the key concepts
1414 of the MiniBooNE reconstruction algorithm [179] and is described in [180] which is
1415 summarised below.

1416 An event in SK can consist of multiple particles. For example, a charge current
1417 muon neutrino interaction can generate two particles that have the potential of gen-
1418 erating Cherenkov photons: the primary muon, and the secondary decay-electron
1419 from the muon. To ensure both subevents are reconstructed separately, each event is
1420 divided into time clusters which are called “subevents”. The number of subevents is

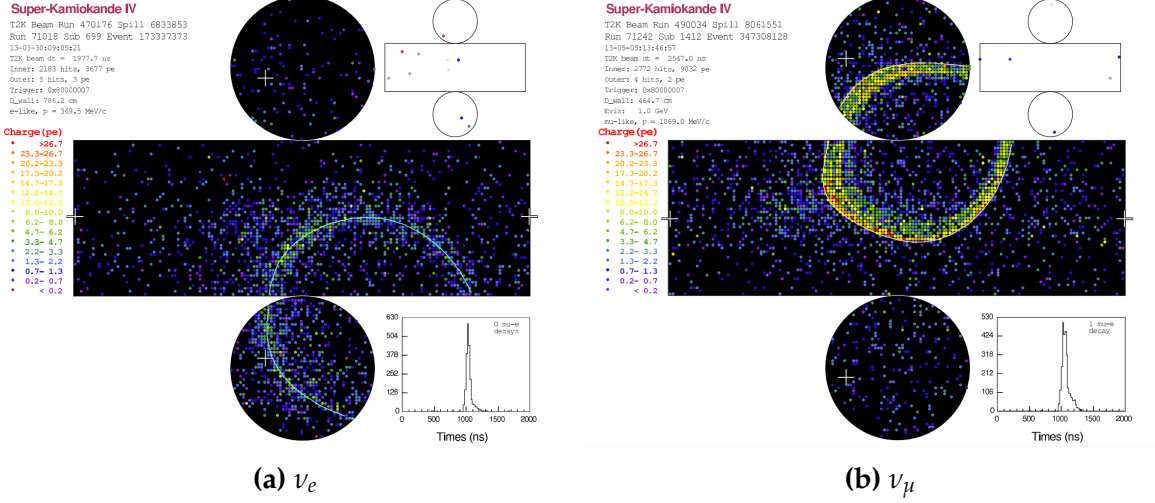


Figure 5.3: Event displays from Super Kamiokande illustrating the “crisp” ring from a muon and the typically “fuzzy” electron ring. Each pixel represents a PMT and the color scheme denotes the accumulated charge deposited on that PMT. Figures taken from [181].

equal to the number of decay electrons minus one (the primary event). To find all the subevents in an event, a vertex goodness metric is calculated for some vertex position \vec{x} and time t ,

$$G(\vec{x}, t) = \sum_i^{\text{hit PMTs}} \exp \left(-\frac{1}{2} \left(\frac{T_{Res}^i(\vec{x}, t)}{\sigma} \right)^2 \right) \quad (5.1)$$

where

$$T_{Res}^i(\vec{x}, t) = t^i - t - |R_{PMT}^i - \vec{x}| / c_n \quad (5.2)$$

is the residual hit time. It is the difference in time between the PMT hit time, t^i , of the i^{th} PMT and the expected time of the PMT hit if the photon was emitted at the start of the vertex. R_{PMT}^i is the position of the i^{th} PMT, c_n is the speed of light in

¹⁴²⁸ water and $\sigma = 4\text{ns}$ which is comparable to the time resolution of the PMT. When the
¹⁴²⁹ proposed fit values of time and vertex are close to the true values, $T_{Res}^i(\vec{x}, t)$ tends to
¹⁴³⁰ zero resulting in subevents appearing as spikes in the goodness metric. The proposed
¹⁴³¹ fit vertex and time are grid-scanned, and the values which maximise the goodness
¹⁴³² metric are selected as the “pre-fit vertex”. Whilst this predicts a vertex for use in
¹⁴³³ the clustering algorithm, the final vertex is fit using the higher-precision maximum
¹⁴³⁴ likelihood method described below.

¹⁴³⁵ Once the pre-fit vertex has been determined, the goodness metric is scanned as
¹⁴³⁶ a function of t to determine the number of subevents. A peak-finding algorithm is
¹⁴³⁷ then used on the goodness metric, requiring the goodness metric to exceed some
¹⁴³⁸ threshold and drop below a reduced threshold before any subsequent additional
¹⁴³⁹ peaks are considered. The thresholds are set such that the rate of false peak finding
¹⁴⁴⁰ is minimised while still attaining good data to Monte Carlo agreement. To improve
¹⁴⁴¹ performance, the pre-fit vertex for each delayed subevent is re-calculated after PMT
¹⁴⁴² hits from the previous subevent are masked. This improves the decay-electron tagging
¹⁴⁴³ performance. Once all subevents have been determined, the time window around
¹⁴⁴⁴ each subevent is then defined by the earliest and latest time which satisfies $-180 <$
¹⁴⁴⁵ $T_{Res}^i < 800\text{ns}$. The subevents and associated time windows are then used as seeds for
¹⁴⁴⁶ further reconstruction.

¹⁴⁴⁷ For a given subevent, the `fitQun` algorithm constructs a likelihood based on the
¹⁴⁴⁸ accumulated charge q_i and time information t_i from the i^{th} PMT,

$$L(\Gamma, \vec{\theta}) = \prod_j^{\text{unhit}} P_j(\text{unhit}|\Gamma, \vec{\theta}) \prod_i^{\text{hit}} \{1 - P_i(\text{unhit}|\Gamma, \vec{\theta})\} f_q(q_i|\Gamma, \vec{\theta}) f_t(t_i|\Gamma, \vec{\theta}), \quad (5.3)$$

1449 where $\vec{\theta}$ defines the track parameters; vertex position, direction vector and mo-
 1450 menta, and Γ represents the particle hypothesis. $P_i(\text{unhit}|\Gamma, \vec{\theta})$ defines the probability
 1451 of the i^{th} tube to not register a hit given the track parameters and particle hypothesis.
 1452 The charge likelihood, $f_q(q_i|\Gamma, \vec{\theta})$, and time likelihood, $f_t(t_i|\Gamma, \vec{\theta})$, represent the prob-
 1453 ability density function of observing charge q_i and time t_i on the i^{th} PMT given the
 1454 specified track parameters and particle hypothesis.

1455 As the generation and propagation of the optical photons are independent of the
 1456 PMT and electronics response, it is natural to split the calculation into two. Firstly,
 1457 the expected number of photoelectrons (or predicted charge), $\mu_i = \mu_i(\vec{\theta}, \Gamma)$, at the i^{th}
 1458 PMT is calculated. This value is then substituted into the likelihood function. This
 1459 allows the charge likelihood density $f_q(q_i|\mu_i)$ and unhit probability $P_i(\text{unhit}|\mu_i)$ to be
 1460 expressed via quantities that are only dependent on the response of the PMT.

1461 The predicted charge is calculated based on contributions from both the direct
 1462 light and the scattered light. The direct light contribution is determined based on the
 1463 integration of the Cherenkov photon profile along the track. PMT angular acceptance,
 1464 water quality, and calibration measurements discussed in subsection 3.1.2 are included
 1465 to accurately predict the charge probability density at each PMT. The scattered light
 1466 is calculated in a similar way, although it includes a scattering function that depends
 1467 on the vertex of the particle and the position of the PMT. The charge likelihood is
 1468 calculated by comparing the prediction to the observed charge in the PMT.

1469 The time likelihood is approximated to depend on the vertex \vec{x} , direction \vec{d} , and
 1470 time t of the track parameters as well as the particle hypothesis. The expected time
 1471 for PMT hits is calculated by assuming unscattered photons being emitted from the
 1472 midpoint of the track, S_{mid} ,

$$t_{exp}^i = t + S_{mid}/c + |R_{PMT}^i - \vec{x} - S_{mid}\vec{d}|/c_n, \quad (5.4)$$

1473 where c is the speed of light in a vacuum. The time likelihood is then expressed in
 1474 terms of the residual difference between the PMT hit time and the expected hit time,
 1475 $t_{Res}^i = t^i - t_{exp}^i$. The particle hypothesis and momentum also affect the Cherenkov
 1476 photon distribution. These parameters modify the shape of the time likelihood density
 1477 since in reality not all photons are emitted at the midpoint of the track. As with the
 1478 charge likelihood, the contributions from both the direct and scattered light to the time
 1479 likelihood density are calculated separately, which are both calculated from particle
 1480 gun studies.

1481 The track parameters and particle identity which maximise $L(\Gamma, \vec{\theta})$ are defined as
 1482 the best-fit parameters. In practice MINUIT [182] is used to minimise the value of
 1483 $-\ln L(\Gamma, \vec{\theta})$. The `fitQun` algorithm considers an electron-like, muon-like, and charged
 1484 pion-like hypothesis for events with a single final state particle, denoted “single-ring
 1485 events”. The particle’s identity is determined by taking the ratio of the likelihood
 1486 of each of the hypotheses. For instance, electrons and muons are distinguished by
 1487 considering the value of $\ln(L(e, \vec{\theta}_e)/L(\mu, \vec{\theta}_\mu))$ in comparison to the reconstructed
 1488 momentum of the electron hypothesis [180]. This distance from this criteria is termed
 1489 the PID parameter and is illustrated in Figure 5.4.

1490 The `fitQun` algorithm also considers a π^0 hypothesis. To do this, it performs a
 1491 fit looking for two standard electron-hypothesis tracks which point to the same four-
 1492 vertex. This assumes the electron tracks are generated from photon-conversion so the
 1493 electron tracks actually appear offset from the proposed π^0 vertex. For these fits, the
 1494 conversion length, direction, and momenta of each photon are also considered as track

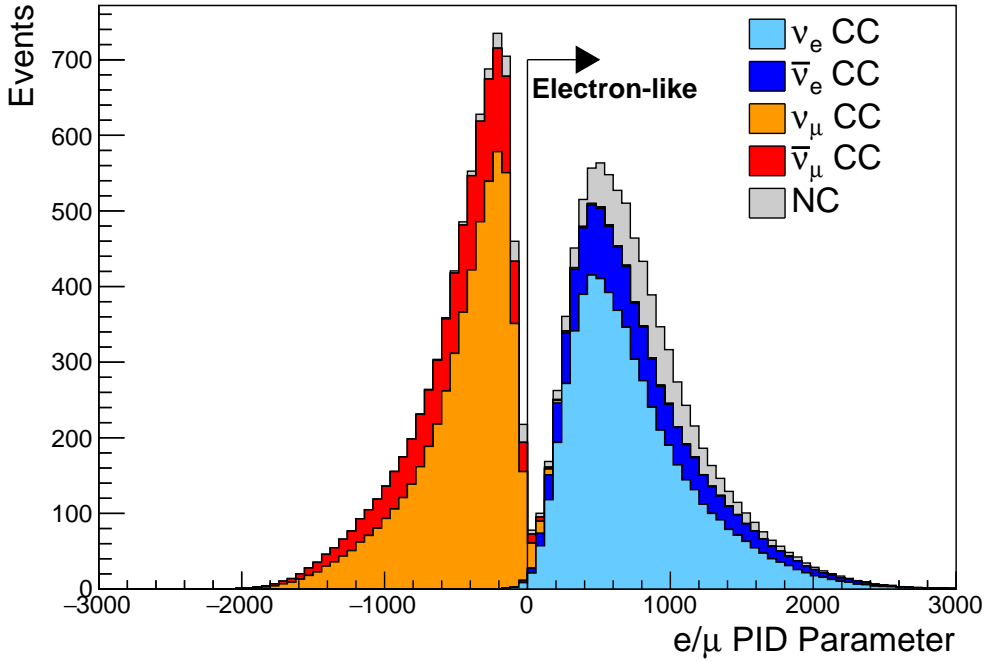


Figure 5.4: The electron/muon PID separation parameter for all sub-GeV single-ring events in SK-IV. The charged current (CC) component is broken down in four flavours of neutrino (ν_μ , $\bar{\nu}_\mu$, ν_e and $\bar{\nu}_e$). Events with positive values of the parameter are determined to be electron-like.

parameters which are then fit in the same methodology as the standard single-ring hypotheses.

Whilst low energy events are predominately single-ring events, higher energy neutrino events can generate final states with multiple particles which generate Cherenkov photons. These “multi-ring” hypotheses are also considered in the `fitQun` algorithm. When calculating the charge likelihood density, the predicted charge associated with each ring is calculated separately and then merged to calculate the total accumulated charge on each PMT. Similarly, the time likelihood for the multi-ring hypothesis is calculated assuming each ring is independent. Each track is time-ordered based on the time of flight from the center of the track to the PMT and the direct light from any ring incident on the PMT is assumed to arrive before any scattered light. To reduce computational resources, the multi-ring fits only consider electron-like and

1507 charged pion-like rings as the pion fit can be used as a proxy for a muon fit due to
1508 their similar mass.

1509 Multi-ring fits proceed by proposing another ring to the previous fit and then
1510 fitting the parameters in the method described above. Typically, multi-ring fits have
1511 the largest likelihood because of the additional degrees of freedom introduced. Conse-
1512 quently, the additional ring is only added if the ratio of likelihoods passes a criterion,
1513 which is determined by Monte Carlo studies.

1514 As an example of how the reconstruction depends on the detector conditions, the
1515 author of this thesis assessed the quality of event reconstruction for SK-V data. The
1516 detector systematics invoked within the T2K-only oscillation analysis are determined
1517 using data to Monte Carlo comparisons using the SK-IV data [183]. Due to tank-open
1518 maintenance occurring between SK-IV and SK-V, the dark rate of each PMT was
1519 observed to increase in SK-V due to light exposure for a significant time during the
1520 repairs. This increase can be seen in Figure 5.5. Run-10 of the T2K experiment was
1521 conducted in the SK-V period, so the consistency of SK-IV and SK-V data needs to
1522 be studied to determine whether the SK-IV-defined systematics can be applied to the
1523 run-10 data. This comparison study was performed using the stopping muon data set
1524 for both the SK-IV and SK-V periods. This data sample is used due to the high rate of
1525 interactions ($O(200)$ events per hour) as well as having similar energies to muons from
1526 CCQE ν_μ interactions from beam interactions. The rate of cosmic muons does depend
1527 on the solar activity cycle [184] but has been neglected in this comparison study. This
1528 is because the shape of the distributions is most important for the purposes of being
1529 compared to the detector systematics. The SK-IV and SK-V data samples consist of
1530 2398.42 and 626.719 hours of data which equates to 686k and 192k events respectively.

1531 The predicted charge calculated in the `fitQun` charge likelihood prediction includes
1532 a contribution from the photoelectron emission due to dark noise. Therefore, the

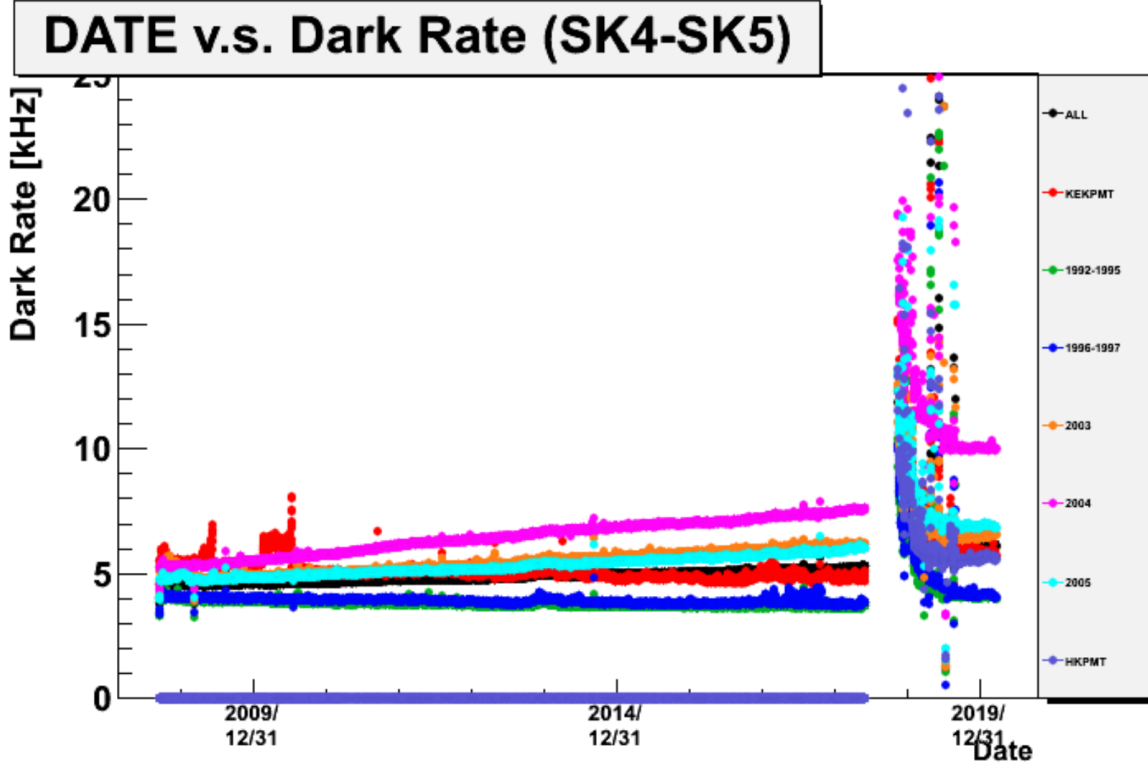


Figure 5.5: The variation of the measured dark rate as a function of date, broken down by PMT type. The SK-IV and SK-V periods span September 2008 to May 2018 and January 2019 to July 2020, respectively. The break in measurement in 2018 corresponds to the period of tank repair and refurbishment. Figure adapted from [183].

increase in the SK-V dark rate needs to be accounted for. In practice, the average dark rate in each SK period is calculated and used as an input in the reconstruction. This is calculated by averaging the dark rate per run for each period separately, using the calibration measurements detailed in subsection 3.1.2. The average dark rate from SK-IV and SK-V were found to be 4.57kHz and 6.30kHz, respectively. The associated charge with the muon and decay electron subevents are illustrated in Figure 5.6. The photoelectron emission from dark noise will be more noticeable for events that have lower energy. This is because this contribution becomes more comparable to the number of photoelectrons emitted from incident photons in low-energy events. This behaviour is observed in the data, where the charge deposited by the muon subevent

1543 is mostly unaffected by the increase in dark rate, whilst the charge associated with the
 1544 decay-electron is clearly affected.

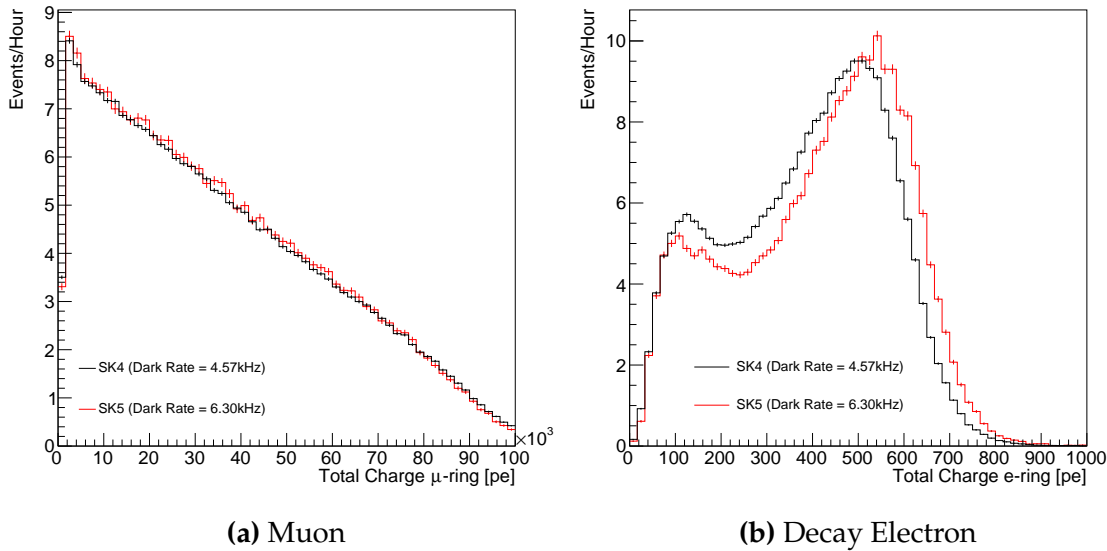


Figure 5.6: Comparison of the measured raw charge deposited per event from the stopping muon data samples between SK-IV (Blue) and SK-V (Red), split by the primary muon subevent and the associated decay electron subevent.

1545 The energy scale systematic for the SK-IV period was determined to be 2.1% [185].
 1546 It is defined to be equal to the difference between data and Monte Carlo prediction
 1547 in the stopping muon data sample. To determine the consistency of the SK-IV and
 1548 SK-V with respect to the energy scale systematic, the muon momentum distribution is
 1549 compared between the two SK periods. As the total number of Cherenkov photons
 1550 is integrated across the track length, the reconstructed momentum divided by track
 1551 length (or range) is compared between SK-IV and SK-V as illustrated in Figure 5.7.

1552 The consistency between these distributions has been computed in two ways.
 1553 Firstly, a Gaussian is fit to each distribution separately. The mean of which is found to
 1554 be $(2.272 \pm 0.003)\text{MeV/cm}$ and $(2.267 \pm 0.006)\text{MeV/cm}$ for SK-IV and SK-V respec-
 1555 tively. The ratio of these is equal to 1.002 ± 0.003 . The mean of the Gaussian fits are
 1556 consistent with the expected stopping power of a minimum ionising muon for a target

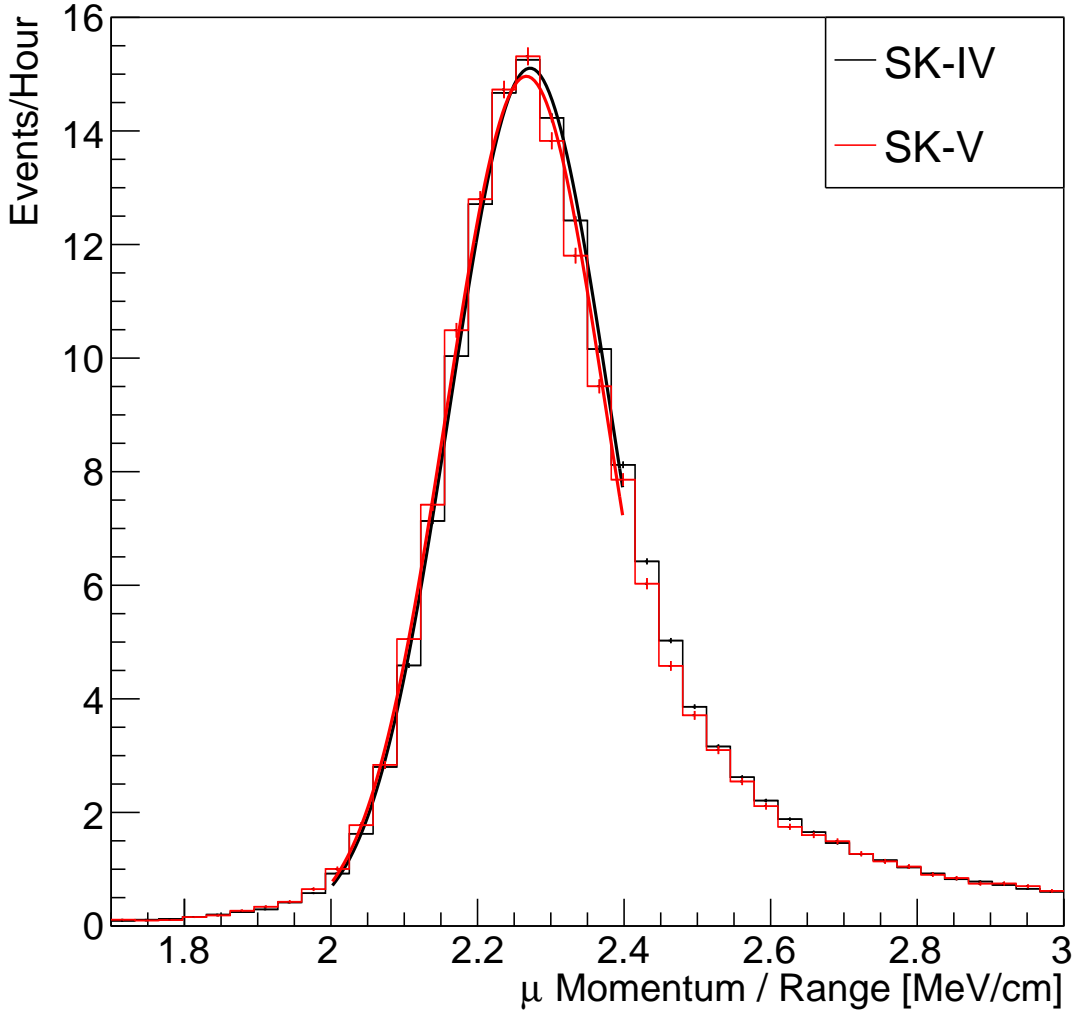


Figure 5.7: The distribution of the reconstructed momentum from the muon ring divided by the distance between the reconstructed muon and decay electron vertices as found in the stopping muon data sets of SK-IV (Black) and SK-IV (Red). Only events with one tagged decay electron are considered. A Gaussian fit is considered in the range [2.0, 2.4] MeV/cm and illustrated as the solid curve.

material (water) with $Z/A \sim 0.5$ [186]. The second consistency check is performed by introducing a nuisance parameter, α , which modifies the SK-V distribution. The value of α which minimises the χ^2 value between the SK-IV and SK-V is determined by scanning across a range of values. This is repeated by applying the nuisance parameter as both a multiplicative factor and an additive shift. The χ^2 distributions for different values of α is illustrated in Figure 5.8. The values which minimise the χ^2 are found to

- ₁₅₆₃ be 0.0052 and 1.0024 for the additive and multiplicative implementations, respectively.
- ₁₅₆₄ No evidence of shifts larger than the 2.1% uncertainty on the energy scale systematic
- ₁₅₆₅ has been found in the reconstructed momentum distribution of SK-IV and SK-V.

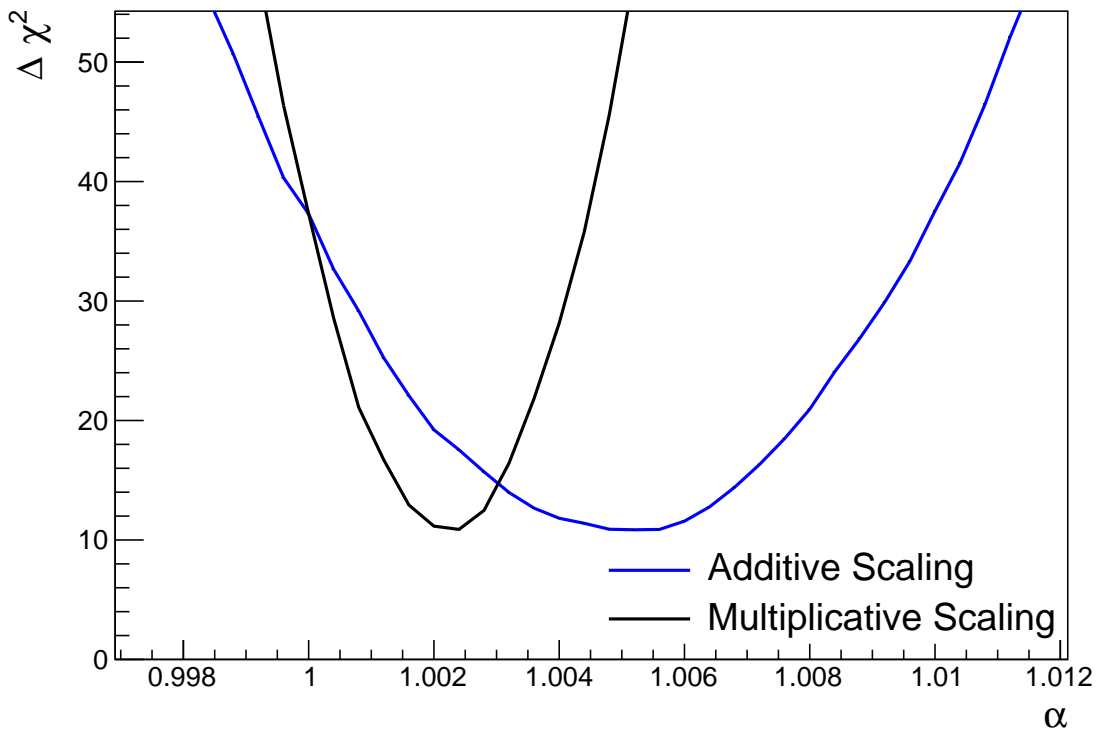


Figure 5.8: The χ^2 difference between the SK-IV and SK-V reconstructed muon momentum divided by range when the SK-V is modified by the scaling parameter α . Both additive (Blue) and multiplicative (Black) scaling factors have been considered. In practice, the additive scaling factor actually uses the value of $(\alpha - 1.0)$ but is illustrated like this so the results can be shown on the same axis range.

₁₅₆₆ 5.3 Event Reduction at SK

- ₁₅₆₇ Atmospheric neutrino events observed in the SK detector are categorised into three
- ₁₅₆₈ different types of samples: fully contained (FC), partially contained (PC) and up-
- ₁₅₆₉ going muon (Up- μ), using PMT hit signatures in the inner and outer detector (ID
- ₁₅₇₀ and OD, respectively). To identify FC neutrino events, it is required that the neutrino

1571 interacts inside the fiducial volume of the ID such that no significant OD activity is
 1572 observed. For this analysis, an event is defined to be in the fiducial volume providing
 1573 the event vertex is at least 0.5m away from the ID walls. PC events have the same
 1574 ID requirements but can have a larger signal present inside the OD. Typically these
 1575 events are higher energy muon interactions that penetrate the ID walls. The Up- μ
 1576 sample contains events where muons are created from neutrino interactions in the
 1577 OD water or rock below the tank. They then propagate upwards through the detector.
 1578 The reason downward-going muons generated from neutrino interactions above the
 1579 tank are neglected is due to the difficulty in separating their signature from the cosmic
 1580 muon shower background. The sample categories are visually depicted in Figure 5.9.

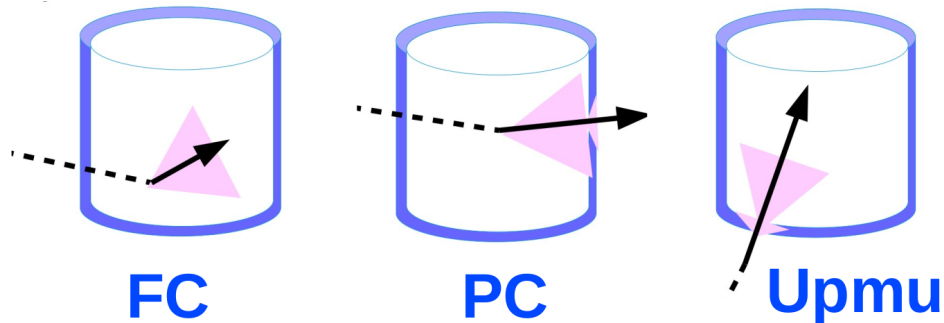


Figure 5.9: A depiction of the topology patterns for fully-contained (FC), partially-contained (PC) and up-going muon (Up- μ) samples included in this analysis.

1581 Based on the event characteristics, as defined by the `fitQun` event reconstruction
 1582 software, the FC events are categorised by

- 1583 • **Visible Energy:** equal to the sum of the reconstructed kinetic energy above the
 1584 Cerenkov threshold for all rings present in the event. The purpose is to separate
 1585 events into sub-GeV and multi-GeV categories.
- 1586 • **Number of observed Cerenkov rings.** The purpose is to separate single-ring and
 1587 multi-ring events, where single-ring events predominantly consist of quasi-elastic
 1588 interactions and multi-ring events are typically resonant pion production or deep
 1589 inelastic scattering events.

- 1590 • **Particle identification parameter of the most energetic ring:** A value deter-
1591 mined from the maximum likelihood value based on `fitQun`'s electron, muon, or
1592 pion hypothesis. The purpose is to separate electron-like and muon-like events.

- 1593 • **Number of decay electrons:** The purpose is to separate quasi-elastic events
1594 (which have one decay electron emitted from the muon decay) and resonant pion
1595 production events (which have two decay electrons emitted from the muon and
1596 pion).

1597 The PC and Up- μ categories are broken down into “through-going” and “stopping”
1598 samples depending on whether the muon left the detector. This is because the stopping
1599 events deposit the entire energy of the interaction into the detector, resulting in better
1600 reconstruction. The energy of events that exit the detector has to be estimated which
1601 introduces much larger systematic uncertainties. Through-going Up- μ samples are
1602 further broken down by whether any hadronic showering was observed in the event
1603 which typically indicates DIS interactions. The expected neutrino energy for the
1604 different categories is given in Figure 5.10. FC sub-GeV and multi-GeV events peak
1605 around 0.7GeV and 3GeV respectively, with slightly different peak energies for $\nu_x \rightarrow \nu_e$
1606 and $\nu_x \rightarrow \nu_\mu$ oscillation channels. PC and Up- μ are almost entirely comprised of
1607 $\nu_x \rightarrow \nu_\mu$ events and peak around 7GeV and 100GeV, respectively.

1608 In normal data-taking operations, the SK detector observes many background
1609 events alongside the beam and atmospheric neutrino signal events of physics interest.
1610 Cosmic ray muons and flasher events, which are the spontaneous discharge of a given
1611 PMT, contribute the largest amount of background events in the energy range relevant
1612 to any analysis searching for neutrino events. Lower energy analyses like DSNB
1613 searches are also subject to radioactive backgrounds [187]. Therefore the data recorded
1614 is reduced with the aim of removing these background events. The reduction process
1615 is detailed in [47, 89] and briefly summarised below.

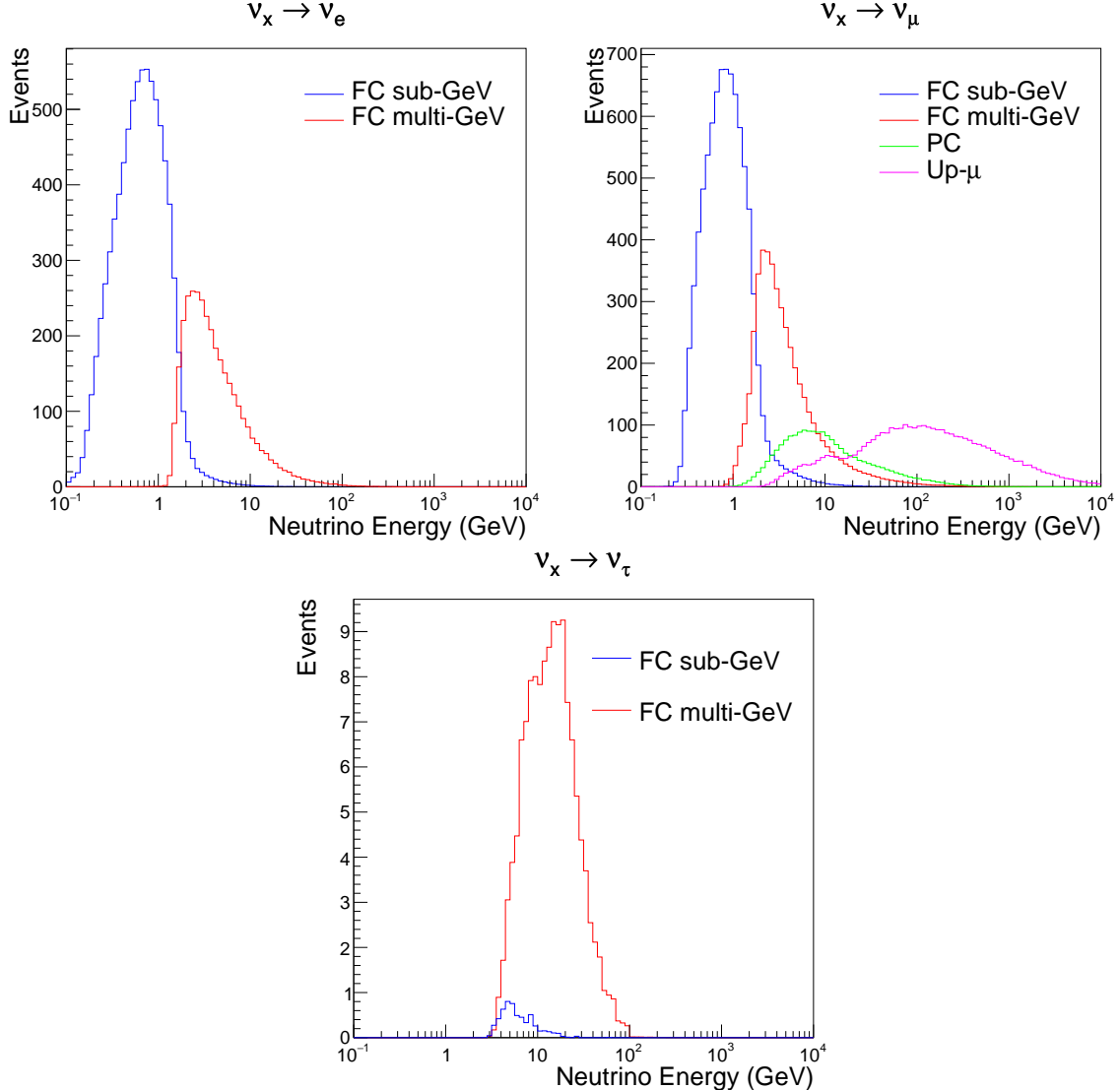


Figure 5.10: The predicted neutrino flux of the fully contained (FC) sub-GeV and multi-GeV, partially contained (PC), and upward-going muon (Up- μ) events. The prediction is broken down by the $\nu_x \rightarrow \nu_e$ prediction (top left), $\nu_x \rightarrow \nu_\mu$ prediction (top right) and $\nu_x \rightarrow \nu_\tau$ prediction (bottom). All systematic dials are set to their nominal values and the Asimov A oscillation parameters are assumed.

1616 The first two steps in the FC reconstruction remove the majority of cosmic ray
 1617 muons by requiring a significant amount of ID activity compared to that measured in
 1618 the OD. Events that pass this cut are typically very high momentum muons or events
 1619 that leave very little activity in the OD. Consequently, a third reduction step is then
 1620 applied to select cosmic-ray muons that pass the initial reduction step. A purpose-built
 1621 cosmic muon fitter is used to determine the entrance (or exit) position of the muon and

1622 a cut is applied to OD activity contained within 8m of this position. Flasher events are
1623 removed in the fourth reduction step which is based on the close proximity of PMT
1624 hits surrounding the PMT producing the flash. Events that pass all these reduction
1625 steps are reconstructed with the APFit algorithm. The fifth step of the reduction uses
1626 information from the more precise fitter to repeat the previous two steps with tighter
1627 cuts. Muons below the Cherenkov threshold can not generate optical photons in the
1628 ID but the associated decay electron can due to its lower mass. These are the types of
1629 events targeted in the fifth reduction step. The final cuts require the event vertex to be
1630 within the fiducial volume (0.5m from the wall although the nominal distance is 2.0m),
1631 visible energy $E_{vis} > 30\text{MeV}$ and fewer than 16 hits within the higher energy OD
1632 cluster. The culmination of the fully contained reduction results in 8.09 events/day in
1633 the nominal fiducial volume [188]. The uncertainty in the reconstruction is calculated
1634 by comparing Monte Carlo prediction to data. The largest discrepancy is found to be
1635 1.3% in the fourth reduction step.

1636 The PC and Up- μ events are processed through their own reduction processes
1637 detailed in [47]. Both of these samples are reconstructed with the APFit algorithm
1638 rather than fitQun. This is because the efficiency of reconstructing events that leave
1639 the detector has not been sufficiently studied for reliable systematic uncertainties. The
1640 PC and Up- μ samples attain events at approximately 0.66 and 1.44 events/day.

1641 Events due to beam neutrinos undergo the same reduction steps as FC events and
1642 are then subject to further cuts [189]. The GPS system which links the timing between
1643 the beam facility and SK needs to be operating correctly and there should be no activity
1644 within the detector in the previous $100\mu\text{s}$ before the trigger. The events then need to
1645 triggered between $-2\mu\text{s}$ and $10\mu\text{s}$ of the expected spill timing.

1646 **Chapter 6**

1647 **Sample Selections and Systematics**

1648 **6.1 Systematic Uncertainties**

1649 The systematics for this uncertainty are split into the groups, or blocks, depending
1650 on their purpose. They consist of flux uncertainties, neutrino-matter interaction
1651 systematics and detector efficiencies. There are also uncertainties on the oscillation
1652 parameters which this analysis will not be sensitive to, Δm_{12}^2 and $\sin^2(\theta_{12})$. As
1653 described in chapter 4, each model parameter used within this analysis requires a
1654 prior uncertainty. This is provided via separate covariance matrices for each block.
1655 The covariance matrices can include prior correlations between parameters within a
1656 single block, but the separate treatment means prior uncertainties can not be included
1657 for parameters in different groups. Alternatively, some parameters have no reasonably
1658 motivated uncertainties. These parameters are assigned flat priors which do not
1659 change the likelihood penalty. The flux, neutrino interaction and detector modelling
1660 has already been discussed in section 5.1. The uncertainties invoked within these
1661 models are described below.

1662 **6.1.1 Beam Flux**

1663 The neutrino beam flux systematics are based upon our uncertainty in the modelling of
1664 the components of the beam. This includes: the hadron production model and their re-
1665 interactions, the shape, intensity and alignment of the beam with respect to the target,

and the uniformity of the magnetic field produced by the horn, alongside other effects. The uncertainty, as a function of neutrino energy, is illustrated in Figure 6.1 which includes the total uncertainty as well as the individual components. The uncertainty for events below, and much higher than, the peak neutrino energy is dominated by hadron production and re-interaction systematics. The beam profile and alignment of the proton beam dominates the systematic uncertainty for events with $E_\nu \sim 1\text{GeV}$.

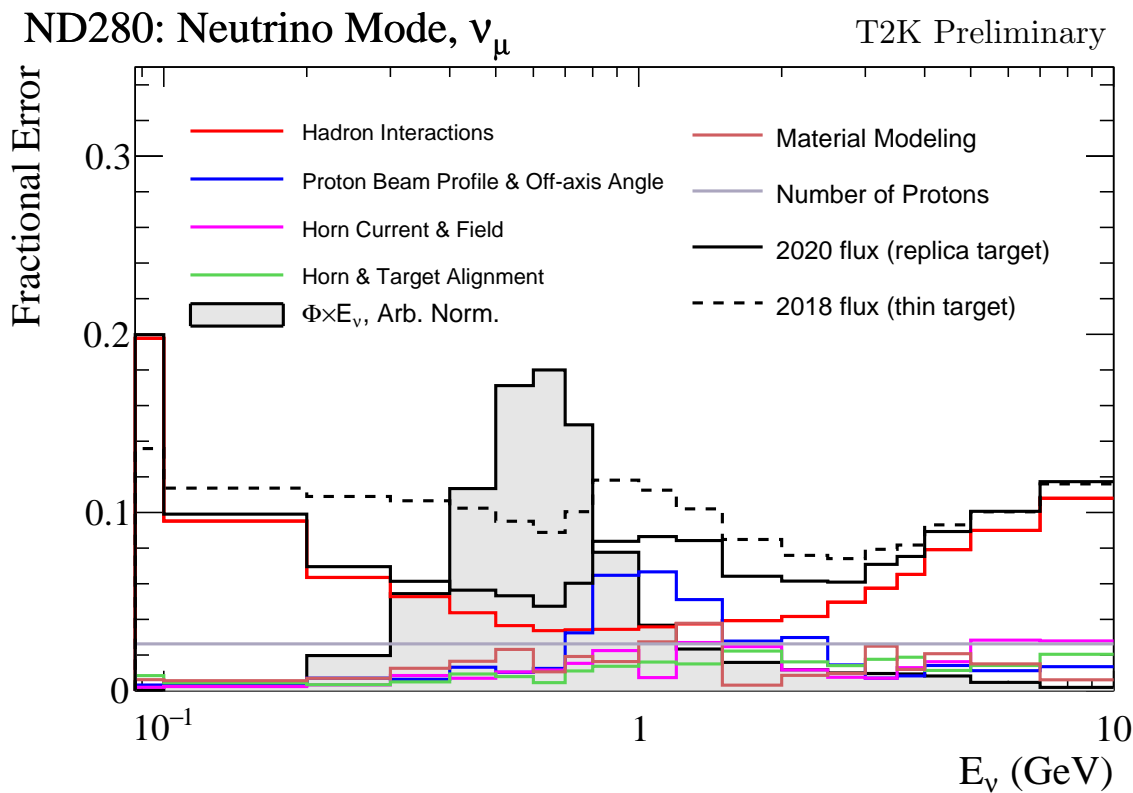


Figure 6.1: The total uncertainty evaluated on the near detector ν_μ flux prediction constrained by the replica-target data, illustrated as a function of neutrino energy. The solid(dashed) line indicates the uncertainty used within this analysis(the T2K 2018 analysis). The solid histogram indicates the neutrino flux as a function of energy. Figure taken from [190].

The beam flux uncertainties are described by one hundred parameters. They are split between both ND280 and SK detectors and binned by neutrino flavour: $\nu_\mu, \bar{\nu}_\mu, \nu_e$ and $\bar{\nu}_e$. The response is then broken down as a function of neutrino energy. The bin density in the neutrino energy is the same for the FHC- ν_μ and RHC- $\bar{\nu}_\mu$, and narrows

for neutrino energies close to the oscillation maxima of $E_\nu = 0.6\text{GeV}$. This binning is specified in Table 6.1. All of these systematic uncertainties are applied as normalisation parameters with Gaussian priors centered at 1.0 and error specified from a covariance matrix provided by the T2K beam group.

Neutrino Flavour	Sign	Neutrino Energy Bin Edges (GeV)
μ	Right	0., 0.4, 0.5, 0.6, 0.7, 1., 1.5, 2.5, 3.5, 5., 7., 30.
μ	Wrong	0., 0.7, 1., 1.5, 2.5, 30.
e	Right	0., 0.5, 0.7, 0.8, 1.5, 2.5, 4., 30.
e	Wrong	0., 2.5, 30.

Table 6.1: The neutrino energy binning for the different neutrino flavours. “Right” sign indicates neutrinos in the FHC beam and antineutrinos in the RHC beam mode. “Wrong” sign indicates antineutrinos in the FHC beam and neutrinos in the RHC beam mode. The binning of the detector response is identical for the FHC and RHC modes as well as at ND280 and SK.

6.1.2 Atmospheric Flux

The atmospheric neutrino flux is modelled by the HKKM model, however 16 systematic uncertainties are applied to control the normalisation of each neutrino flavour, energy and direction. All of the parameters are given Gaussian priors centered at 0 and width 1.. They are summarised below:

- **Absolute Normalisation:** The overall normalisation of each neutrino flavour is controlled by two independent systematic uncertainties, for $E_\nu < 1\text{GeV}$ and $E_\nu > 1\text{GeV}$, respectively. This is driven mostly by hadronic interaction uncertainties for the production of pions and kaons [43]. The strength of the response is dependent upon the neutrino energy.

- **Relative Normalisation:** Uncertainties on the ratio of $(\nu_\mu + \bar{\nu}_\mu) / (\nu_e + \bar{\nu}_e)$ are controlled by the difference between the HKKM model [43], FLUKA [46] and

1692 Bartol models [42]. Three independent parameters are applied in the energy
1693 ranges: $E_\nu < 1\text{GeV}$, $1\text{GeV} < E_\nu < 10\text{GeV}$, and $E_\nu > 10\text{GeV}$.

- 1694 • **$\nu/\bar{\nu}$ Normalisation:** The uncertainties in the π^+/π^- (and kaon equivalent) pro-
1695 duce uncertainties in the flux of $\nu/\bar{\nu}$. The response is applied in the same way as
1696 the relative normalisation parameters.
- 1697 • **Up/Down and Vertical/Horizontal Ratio:** Similar to the above two systematics,
1698 the difference between the HKKM, FLUKA and Bartol model predictions, as a
1699 function of $\cos(\theta_Z)$, is used to control the normalisation of events as a function of
1700 zenith angle.
- 1701 • **K/π Ratio:** Higher energy neutrinos ($E_\nu < 10\text{GeV}$) become dependent upon
1702 kaon decay as the dominant source of neutrinos. Measurements of the ratio of
1703 K/π [191] are used to control the systematic uncertainty of the expected ratio of
1704 pion and kaon production.
- 1705 • **Solar Activity:** As the 11-year solar cycle can affect the Earth's magnetic field, the
1706 flux of primary cosmic rays is modulated across the same period. The uncertainty
1707 is calculated by taking a ± 1 year variation, equating to a 10% uncertainty for the
1708 SK-IV period.
- 1709 • **Atmospheric Density:** The height of the interaction of the primary cosmic rays is
1710 dependent upon the atmospheric density. The HKKM assumes the US standard
1711 1976 [153] profile. This systematic controls the uncertainty in that model.

1712 Updates to the HKKM and Bartol models are underway to use a similar tuning
1713 technique to that used in the beam flux predictions. After those updates, it may be
1714 possible to include correlations in the hadron production uncertainty systematics for
1715 beam and atmospheric flux predictions.

1716 6.1.3 Neutrino Interaction

₁₇₁₇ **Chapter 7**

₁₇₁₈ **Oscillation Probability Calculation**

₁₇₁₉ It is important to understand how and where the sensitivity to the oscillation pa-
₁₇₂₀ rameters comes from for both atmospheric and beam samples. An overview of how
₁₇₂₁ these samples observe changes in δ_{CP} , Δm_{23}^2 , and $\sin^2(\theta_{23})$ is given in section 7.1. It
₁₇₂₂ also explains the additional complexities involved when performing an atmospheric
₁₇₂₃ neutrino analysis as compared to a beam-only analysis.

₁₇₂₄ Without additional techniques, atmospheric sub-GeV upward-going neutrinos
₁₇₂₅ ($E_\nu < 1.33\text{GeV}, \cos(\theta_Z) < 0.$) can artificially inflate the sensitivity to δ_{CP} due to the
₁₇₂₆ quickly varying oscillation probability in this region. Therefore, a “sub-sampling”
₁₇₂₇ approach has been developed to reduce these biases ensuring accurate and reliable
₁₇₂₈ sensitivity measurements. This technique ensures that small-scale unresolvable fea-
₁₇₂₉ tures of the oscillation probability have been averaged over whilst the large-scale
₁₇₃₀ features in the oscillation probability are unaffected. The documentation and valida-
₁₇₃₁ tion of this technique are found in section 7.2. The oscillation probability calculation is
₁₇₃₂ computationally intensive due to the large number of matrix multiplications needed.
₁₇₃₃ Consequently, the CUDAProb3 implementation choice made within the fitting frame-
₁₇₃₄ work, as detailed in section 7.3, ensures that the analysis can be done in a timely
₁₇₃₅ manner.

₁₇₃₆ Whilst the beam neutrinos are assumed to propagate through a constant density
₁₇₃₇ slab of material, the density variations through the Earth result in more complex
₁₇₃₈ oscillation patterns. Furthermore, the uncertainty in the electron density can modify
₁₇₃₉ the oscillation probability for the denser core layers of the Earth. The model of the

¹⁷⁴⁰ Earth used within this analysis is detailed in section 7.4. This includes information
¹⁷⁴¹ about the official SK-only methodology as well as improvements that can be made
¹⁷⁴² to remove some of the approximations made in that analysis. Another complexity of
¹⁷⁴³ atmospheric neutrinos oscillation studies is that the height of production in the atmo-
¹⁷⁴⁴ sphere is not known on an event-by-event basis. An analytical averaging technique
¹⁷⁴⁵ that approximates the uncertainty of the oscillation probability has been followed,
¹⁷⁴⁶ with the author of this thesis being responsible for the implementation and validation.
¹⁷⁴⁷ This implementation of an external technique is illustrated in section 7.5.

¹⁷⁴⁸ 7.1 Overview

¹⁷⁴⁹ The analysis presented within this thesis focuses on the determination of oscillation
¹⁷⁵⁰ parameters from atmospheric and beam neutrinos. Whilst subject to the same oscil-
¹⁷⁵¹ lation formalism, the way in which the two samples have sensitivity to the different
¹⁷⁵² oscillation parameters differs quite significantly.

¹⁷⁵³ Atmospheric neutrinos have a varying baseline, or “path length”, L , such that
¹⁷⁵⁴ the distance each neutrino travels before interacting is dependent upon the zenith
¹⁷⁵⁵ angle, θ_Z . As primary cosmic rays can interact anywhere between the Earth’s surface
¹⁷⁵⁶ and $\sim 50\text{km}$ above that, the height, h , in the atmosphere at which the neutrino was
¹⁷⁵⁷ generated also affects the path length,

$$L = \sqrt{(R_E + h)^2 - R_E^2 (1 - \cos^2(\theta_Z))} - R_E \cos(\theta_Z). \quad (7.1)$$

¹⁷⁵⁸ Where $R_E = 6,371\text{km}$ is the Earth’s radius. Consequently, the oscillation probabil-
¹⁷⁵⁹ ity is dependent upon two parameters, $\cos(\theta_Z)$ and E_ν .

¹⁷⁶⁰ The oscillation probability used within this analysis is based on [21]. The neutrino
¹⁷⁶¹ wavefunction in the vacuum Hamiltonian evolves in each layer of constant matter
¹⁷⁶² density via

$$i\frac{d\psi_j(t)}{dt} = \frac{m_j^2}{2E_\nu}\psi_j(t) - \sum_k \sqrt{2}G_F N_e U_{ej} U_{ke}^\dagger \psi_k(t), \quad (7.2)$$

¹⁷⁶³ where m_j^2 is the square of the j^{th} vacuum eigenstate mass, E_ν is the neutrino
¹⁷⁶⁴ energy, G_F is Fermi's constant, N_e is the electron number density and U is the PMNS
¹⁷⁶⁵ matrix. The transformation $N_e \rightarrow -N_e$ and $\delta_{CP} \rightarrow -\delta_{CP}$ is applied for antineutrino
¹⁷⁶⁶ propagation. Thus, a model of the Earth's density is required for atmospheric neutrino
¹⁷⁶⁷ propagation. Following the official SK-only methodology [192], this analysis uses the
¹⁷⁶⁸ Preliminary Reference Earth Model (PREM) [193]. This model provides piecewise cubic
¹⁷⁶⁹ polynomials as a function of the Earth's radius which results in the density profile
¹⁷⁷⁰ illustrated in Figure 7.1. As discussed, the propagator requires layers of constant
¹⁷⁷¹ density. The SK methodology approximates the PREM model by using four layers of
¹⁷⁷² constant density [192]. The details of these layers are detailed in Table 7.1.

Layer	Outer Radius [km]	Density [g/cm ³]	Chemical composition (Z/A)
Inner Core	1220	13	0.468 ± 0.029
Outer Core	3480	11.3	0.468 ± 0.029
Lower Mantle	5701	5.0	0.496
Transition Zone	6371	3.3	0.496

Table 7.1: Description of the four layers of the Earth invoked within the constant density approximation of the PREM model [193].

¹⁷⁷³ The atmospheric neutrino oscillation probabilities can be presented as two dimensional
¹⁷⁷⁴ “oscillograms” as illustrated in Figure 7.2. The distinct discontinuities, as a

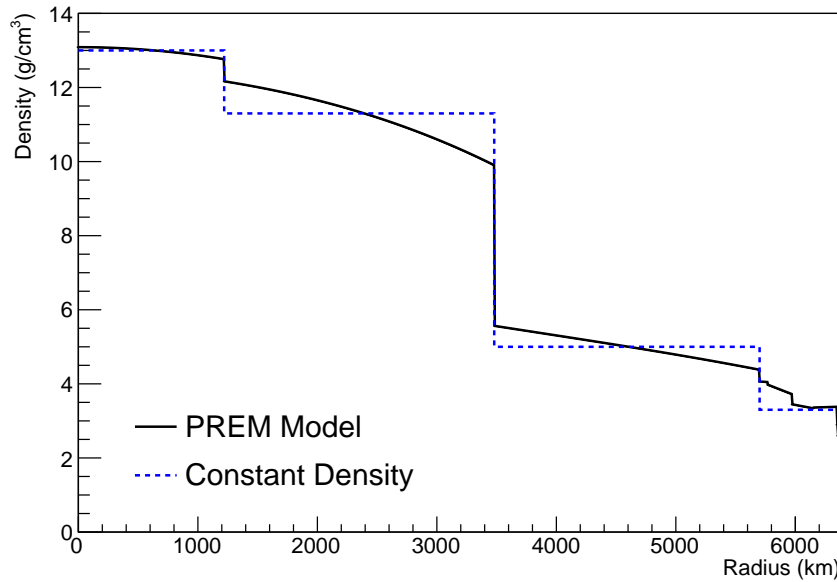


Figure 7.1: The density of the Earth given as a function of the radius, as given by the PREM model (Black), and the constant density four-layer approximation (Blue), as used in the official SK-only analysis.

₁₇₇₅ function of $\cos(\theta_Z)$, are due to the discrete change in density invoked within the PREM
₁₇₇₆ model.

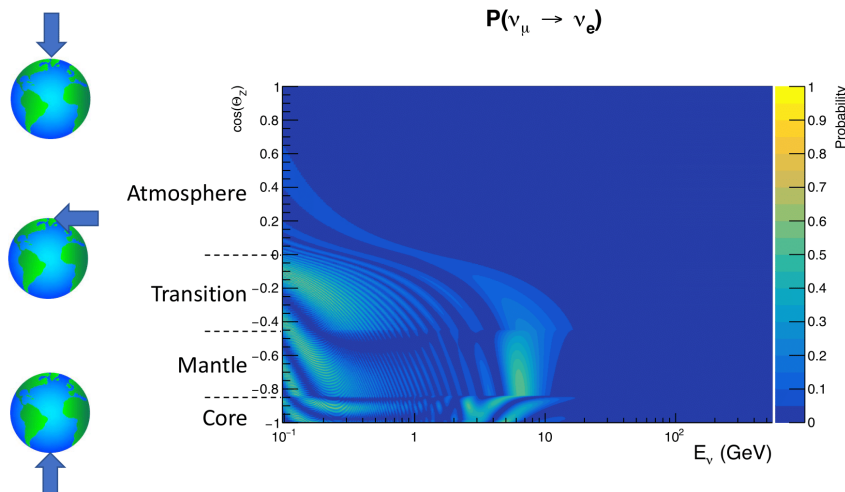


Figure 7.2: An “oscillogram” that depicts the $P(\nu_\mu \rightarrow \nu_e)$ oscillation probability as a function of neutrino energy and cosine of the zenith angle. The zenith angle is defined such that $\cos(\theta_Z) = 1.0$ represents neutrinos that travel from directly above the detector. The four-layer constant density PREM model approximation is used and Asimov A oscillation parameters are assumed (Table 2.2).

Atmospheric neutrinos do have sensitivity to δ_{CP} through a normalisation term. Figure 7.3 illustrates the difference in oscillation probability between CP-conserving ($\delta_{CP} = 0.$) and a CP-violating ($\delta_{CP} = -1.601$) value taken from Asimov A oscillation parameter set (Table 2.2). The result is a complicated oscillation pattern in the appearance probability for sub-GeV upgoing neutrinos. The detector does not have sufficient resolution to resolve these individual patterns so the sensitivity to δ_{CP} for atmospheric neutrinos comes via the overall normalisation of these events.

The presence of matter means that the effect δ_{CP} has on the oscillation probability is not equal between neutrinos and antineutrinos, which would be expected when propagating through a vacuum. This is further extenuated by the fact that SK can not distinguish neutrinos and antineutrinos well and that the cross-section neutrino interaction is larger than that for antineutrinos. Finally, sample selections (discussed in DB: [Link to selection chapter](#)) targeting different neutrino interaction modes result in an imbalance in the percentage of neutrinos to anti-neutrinos. This is because negatively charged pions from antineutrino interactions are more likely to be captured by a nucleus compared to a positively charged pion. All of these effects lead to a difference in the number of neutrinos detected compared to antineutrinos. This changes how the δ_{CP} normalisation term is observed, resulting in a very complex sensitivity to δ_{CP} .

Atmospheric neutrinos are subject to matter effects as they travel through the dense matter in the Earth. The vacuum and matter oscillation probabilities for $P(\nu_e \rightarrow \nu_e)$ and $P(\bar{\nu}_e \rightarrow \bar{\nu}_e)$ are presented in Figure 7.4, where the PREM model has been assumed. The oscillation probability for both neutrinos and antineutrinos is affected in the presence of matter. However, the resonance effects around $O(5)\text{GeV}$ only occur for neutrinos in normal mass hierarchy and antineutrinos in inverse mass hierarchy. The

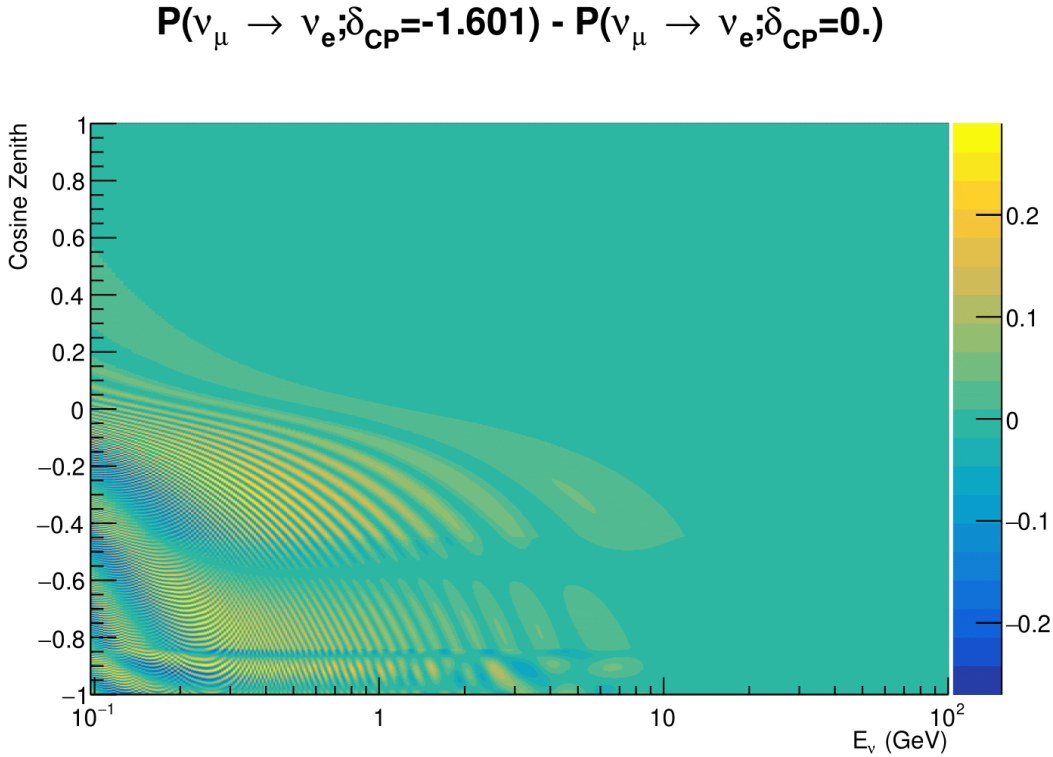


Figure 7.3: The effect of δ_{CP} for atmospheric neutrinos given in terms of the neutrino energy and zenith angle. This oscillogram compares the $P(\nu_\mu \rightarrow \nu_e)$ oscillation probability for a CP conserving ($\delta_{CP} = 0.0$) and a CP violating ($\delta_{CP} = -1.601$) value taken from the Asimov A parameter set. The other oscillation parameters assume the Asimov A oscillation parameter set given in Table 2.2.

1802 exact position and amplitude of the resonance depend on $\sin^2(\theta_{23})$ meaning that the
 1803 atmospheric neutrinos have sensitivity to $\sin^2(\theta_{23})$.

1804 As the T2K beam flux is centered at the first oscillation maximum ($E_\nu = 0.6\text{GeV}$),
 1805 the sensitivity to δ_{CP} is predominantly observed as a change in the event-rate of e-like
 1806 samples in $\nu/\bar{\nu}$ modes. Figure 7.5 illustrates the $P(\nu_\mu \rightarrow \nu_e)$ oscillation probability
 1807 for a range of δ_{CP} values. A circular modulation of the first oscillation peak (in both
 1808 magnitude and position) is observed when varying throughout the allowable values
 1809 of δ_{CP} . The CP-conserving values of $\delta_{CP} = 0, \pi$ have a lower(higher) oscillation
 1810 maximum than the CP-violating values of $\delta_{CP} = -\pi/2 (\delta_{CP} = \pi/2)$. A sub-dominant

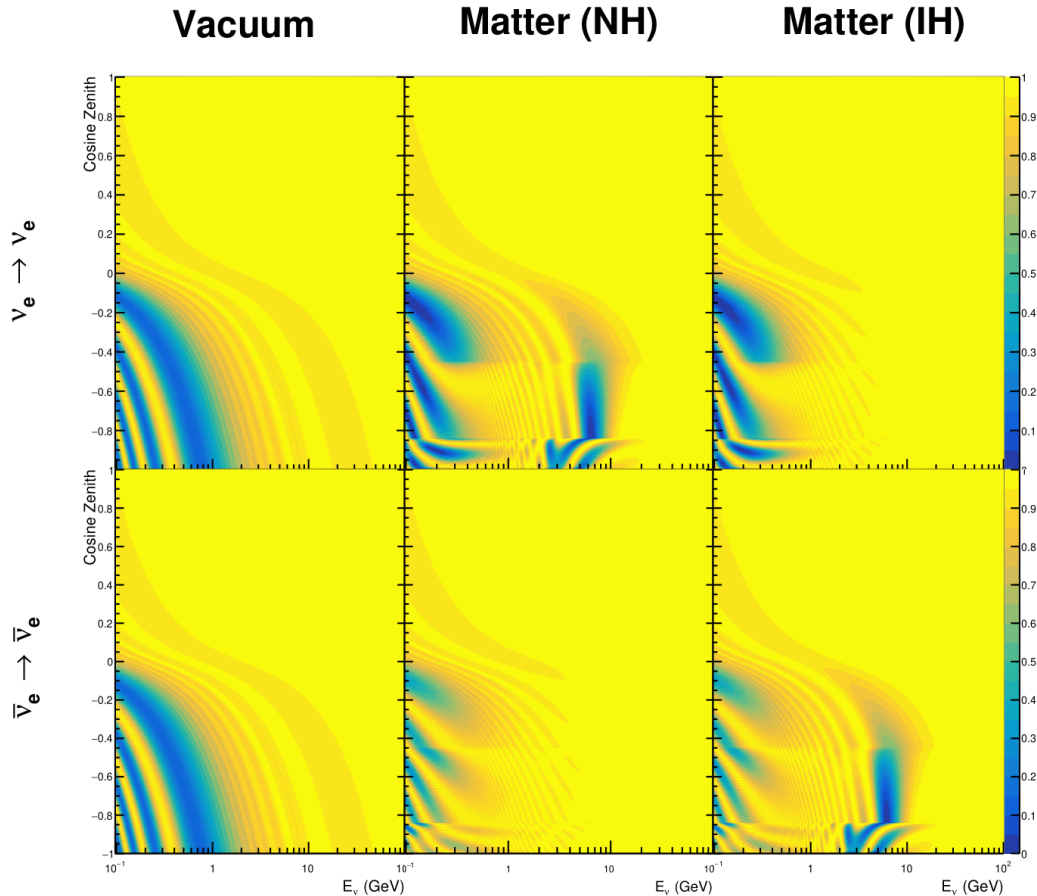


Figure 7.4: An illustration of the matter-induced effects on the oscillation probability, given as a function of neutrino energy and zenith angle. The top row of panels gives the $P(\nu_e \rightarrow \nu_e)$ oscillation probability and the bottom row illustrates the $P(\bar{\nu}_e \rightarrow \bar{\nu}_e)$ oscillation probability. The left column highlights the oscillation probability in a vacuum, whereas the middle and right column represents the oscillation probabilities when the four-layer fixed density PREM model is assumed. All oscillation probabilities assume the “Asimov A” set given in Table 2.2, but importantly, the right column sets an inverted mass hierarchy. The “matter resonance” effects at $E_\nu \sim 5\text{GeV}$ can be seen in the $P(\nu_e \rightarrow \nu_e)$ for normal mass hierarchy and $P(\bar{\nu}_e \rightarrow \bar{\nu}_e)$ for inverted hierarchy.

shift in the energy of the oscillation peak is also present to aid in separating the two

CP-conserving values of δ_{CP} .

T2K’s sensitivity to the $\sin^2(\theta_{23})$ and Δm_{23}^2 is observed as a shape-based variation

of the muon-like samples, as illustrated in Figure 7.5. The value of Δm_{32}^2 laterally shifts

the position of the oscillation dip (around $E_\nu \sim 0.6\text{GeV}$) in the $P(\nu_\mu \rightarrow \nu_\mu)$ oscillation

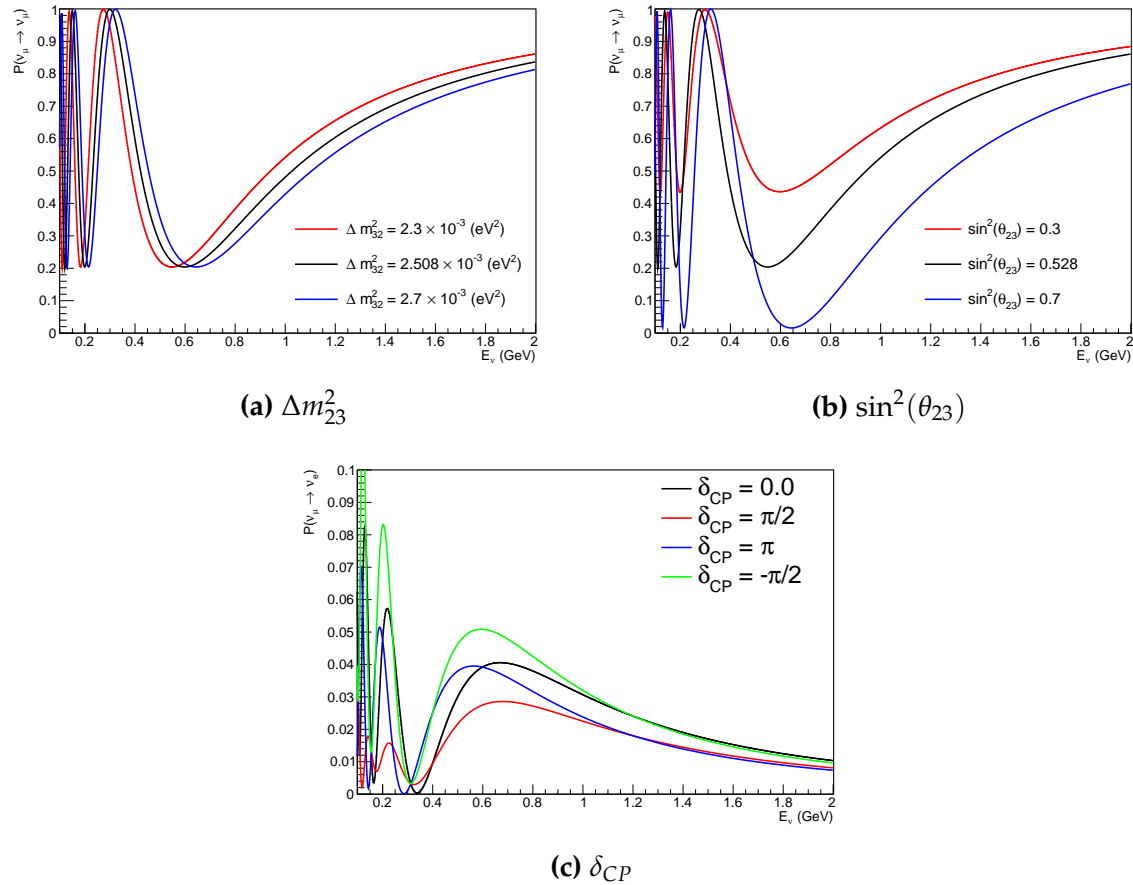


Figure 7.5: The oscillation probability for beam neutrino events given as a function of neutrino energy. All oscillation parameters assume the “Asimov A” set given in Table 2.2 unless otherwise stated. Each panel represents a change in one of the oscillation parameters whilst keeping the remaining parameters fixed.

probability. A variation of $\sin^2(\theta_{23})$ is predominantly observed as a vertical shift of the oscillation dip with second-order horizontal shifts being due to matter effects. The beam neutrinos have limited sensitivity to matter effects due to the relatively shorter baseline as well as the Earth’s mantle being a relatively low-density material (as compared to the Earth’s core). For some values of δ_{CP} , the degeneracy in the number of e-like events allows the mass hierarchy to be resolved. This leads to a δ_{CP} -dependent mass hierarchy sensitivity which can be seen in Figure 7.6.

Whilst all oscillation channels should be included for completeness, the computational resources required to run a fit are limited and any reasonable approximations

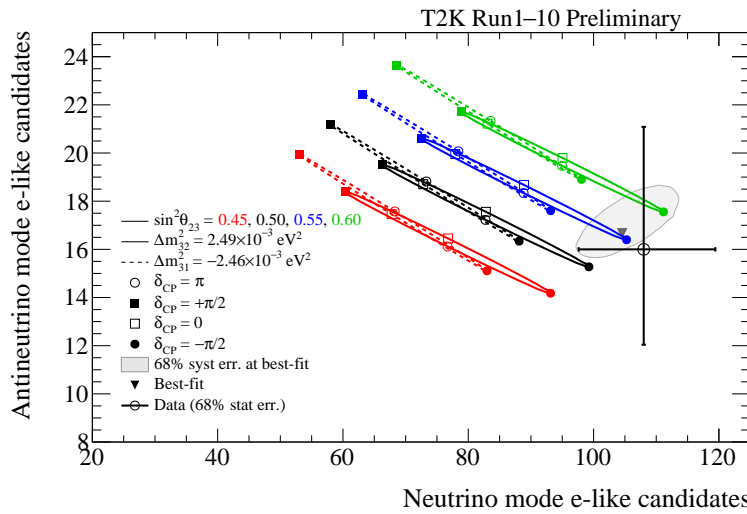


Figure 7.6: The number of electron-like events in the FHC and RHC operating mode of the beam, as a function of the oscillation probabilities. Both normal hierarchy (Solid) and inverse hierarchy (Dashed) values of Δm_{23}^2 are given.

which reduce the number of oscillation probability calculations that need to be made should be applied. The $\nu_e \rightarrow \nu_{e,\mu,\tau}$ (and antineutrino equivalent) oscillations can be ignored for beam neutrinos as the $\nu_e/\bar{\nu}_e$ fluxes are approximately two orders of magnitude smaller than the corresponding $\nu_\mu/\bar{\nu}_\mu$ flux. Furthermore, as the peak neutrino energy of the beam is well below the threshold for charged current tau production ($E_\nu = 3.5 \text{ GeV}$ [51], only a small proportion of the neutrinos produced in the beam have the required energy. For the few neutrinos that have sufficient energy, the oscillation probability is very small due to the short baseline. Whilst these approximations can be made for the beam neutrinos, the atmospheric flux of ν_e is of the same order of magnitude as the ν_μ flux and the energy distribution of atmospheric neutrinos extends well above the tau production threshold.

¹⁸³⁶ 7.2 Treatment of Fast Oscillations

¹⁸³⁷ As shown in Figure 7.7, atmospheric neutrino oscillations have a significantly more
¹⁸³⁸ complex structure for upgoing neutrinos with energy below 1GeV. This is because the
¹⁸³⁹ L/E dependence of the oscillation probability in this region induces rapid variations
¹⁸⁴⁰ for small changes in L or E . As discussed in section 7.1, this is also the region in which
¹⁸⁴¹ atmospheric neutrinos have sensitivity to δ_{CP} . In practice, the direction of the neutrino
¹⁸⁴² is inferred from the direction of the final state particles traveling in the detector, which
¹⁸⁴³ can be poor for low-energy neutrino interactions. This creates a distinct difference
¹⁸⁴⁴ from the beam neutrinos where the position of the source is very precisely known.

¹⁸⁴⁵ As a consequence of the unresolvable structure, an average oscillation probability
¹⁸⁴⁶ is observed in the subGeV upgoing region. This creates a computational problem; A
¹⁸⁴⁷ significantly large amount of Monte Carlo statistics would be required to accurately
¹⁸⁴⁸ predict the number of events if Monte Carlo averaging was the only technique used.
¹⁸⁴⁹ This section describes the ‘sub-sampling’ approach developed for this analysis and
¹⁸⁵⁰ compares it to the methodology used within the SK-only analysis.

¹⁸⁵¹ The official SK-only analysis uses the osc3++ oscillation parameter fitter [192].
¹⁸⁵² To perform the fast oscillation averaging, it uses a ‘nearest-neighbour’ technique.
¹⁸⁵³ For a given neutrino event, the nearest twenty neighbours in reconstructed lepton
¹⁸⁵⁴ momentum and zenith angle are found and a distribution of their neutrino energies is
¹⁸⁵⁵ built. The RMS, σ , of this distribution is then used to compute an average oscillation
¹⁸⁵⁶ probability for the given neutrino Monte Carlo event.

¹⁸⁵⁷ For the i^{th} event, the oscillation weight is calculated as

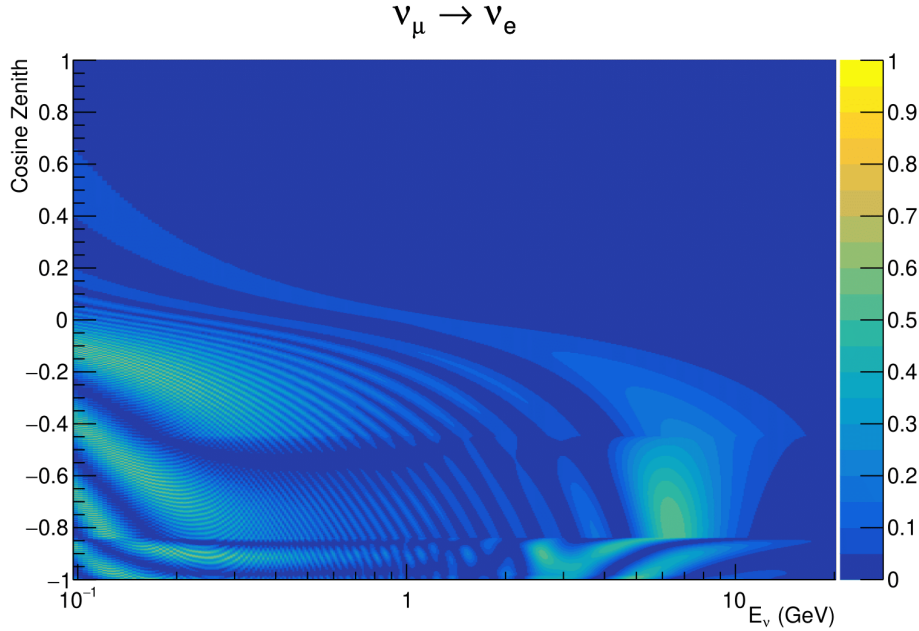


Figure 7.7: The oscillation probability $P(\nu_\mu \rightarrow \nu_e)$, given as a function of neutrino energy and zenith angle, which highlights an example of the “fast” oscillations in the sub-GeV upgoing region.

$$W_i = \frac{1}{5}P(E_i, \bar{L}_i) + \frac{1}{5} \sum_{\beta=-1,-0.5,0.5,1} P(E_i + \beta\sigma_i, L_\beta), \quad (7.3)$$

where $P(E, L)$ is the oscillation probability calculation for neutrino energy E and path length L and the two path lengths, \bar{L}_i and L_β are discussed below. All of the oscillation probability calculations are performed with a fixed zenith angle such that the same density profile is used.

The uncertainty in the production height is controlled by using an “average” production height, \bar{L}_i , which represents the average path length computed using twenty production heights taken from the Honda flux model’s prediction [45]. For a given event, the production heights are sampled in steps of 5% of their cumulative distribution function. L_β values are similarly calculated but instead use different combinations of four production heights,

$$\begin{aligned}
 L_{-1.0} &= \frac{1}{4}L(45, 50, 55, 60), \\
 L_{-0.5} &= \frac{1}{4}L(35, 40, 65, 70), \\
 L_{+0.5} &= \frac{1}{4}L(25, 30, 75, 68), \\
 L_{+1.0} &= \frac{1}{4}L(15, 20, 85, 89).
 \end{aligned} \tag{7.4}$$

1868 This averaging technique works because of the inference between the zenith angle
 1869 and the reconstructed direction of final state particles in the detector. For low-energy
 1870 neutrinos, where the resolution of the true neutrino direction is poor, σ_i will be large,
 1871 resulting in significant averaging effects. Contrary to this, the inferred direction of
 1872 high-energy neutrinos will be much closer to the true value, meaning that σ_i will be
 1873 smaller, culminating in small averaging effects.

1874 In practice, this technique is performed before the fit in order to deal with the
 1875 computational cost. This is possible as the Osc3++ framework uses binned oscillation
 1876 parameters rather than continuous so the oscillation parameters used in the fit are
 1877 known prior to run-time. The framework used in this analysis uses continuous
 1878 oscillation parameters, and due to the MCMC fitting technique, there is no way to
 1879 know which oscillation parameter values will be selected *a priori*. Therefore, the
 1880 oscillation parameter calculation has to be performed at run-time. Computing five
 1881 oscillation probabilities per event would require far too many computational resources
 1882 to be viable. Therefore SK technique can not be used within this analysis. However,
 1883 the concept of the averaging technique can be taken from it.

1884 To perform a similar averaging as the SK analysis, a sub-sampling approach using
 1885 binned oscillograms has been devised. The technique can be explained by considering
 1886 a “fine” and “coarse” oscillogram. The fine oscillograms are used to define the array of

1887 $\cos(\theta_Z)$ and E_ν used in the oscillation engine. The coarse oscillograms cover the same
1888 phase-space but have fewer bins, where the value of a particular coarse bin is taken
1889 as the linear average (flat prior in E_ν and $\cos(\theta_Z)$) of all fine bins which falls into it.
1890 The coarse oscillogram is then used for determining the oscillation weight for a given
1891 event. The binning which is used to calculate the oscillation probabilities, known as
1892 the ‘fine’ binning, has $N \times N$ subdivisions per coarse bin. Figure 7.8 illustrates the
1893 $N = 2$ example where the assigned value to a coarse bin is the average of the four fine
1894 bins which fall in that coarse bin. Whilst the coarse bin edges do not have to be linear
1895 on either axis, the sub-division of the fine bins is linear over the range of a coarse bin.

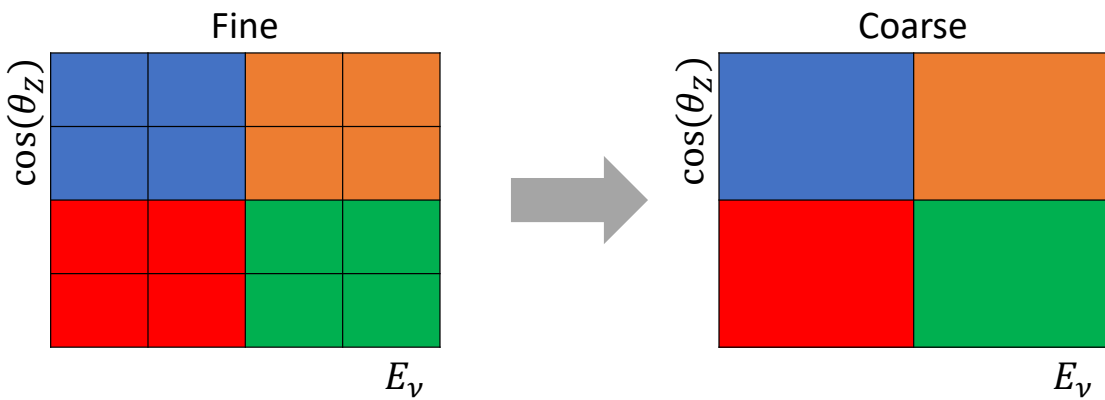


Figure 7.8: Illustration of the averaging procedure for $N = 2$. The oscillation probabilities calculated on the finer left binning are averaged to obtain the oscillation probabilities in the coarser right binning. These averaged oscillation probabilities with the coarser binning are then applied to each event during the fit.

1896 The coarse binning is defined with 67×52 bins in true neutrino energy \times cosine
1897 zenith. It is picked to be identical to that provided in [194]. In general, the binning is
1898 logarithmically spaced in neutrino energy but has some hand-picked bin edges. Firstly,
1899 the bin density around the matter resonance is smoothly increased around the matter
1900 resonance region. This is to avoid smearing this region which can be well sampled by
1901 the Monte Carlo. Secondly, bin edges are selected to hit $0.4, 0.6, 1, 10, 30, 50, 100\text{GeV}$.
1902 This is to ensure that the Coulomb correction systematic and the atmospheric flux
1903 systematics definitions in neutrino energy can be hit. The cosine zenith binning is

1904 approximately linearly spaced across the allowable range but the values of layer
 1905 transitions are hit precisely: -0.8376 (core-mantle) and -0.4464 (mantle/transition
 1906 zone). Bins are spread further apart for downgoing events as this is a region unaffected
 1907 by the fast oscillation wavelengths and reduces the total number of calculations
 1908 required to perform the calculation.

1909 The choice of N is justified based on two studies. Firstly, the variation of event rates
 1910 of each sample is studied as a function of N . For a given set of oscillation parameters
 1911 thrown from the PDG prior constraints (detailed in Table 2.1), the oscillation probabili-
 1912 ties are calculated using a given value of N . Each sample is re-weighted and the event
 1913 rate is stored. The value of N is scanned from 1, which corresponds to no averaging, to
 1914 24, which corresponds to the largest computationally viable subdivision binning. The
 1915 event rate of each sample at large N is expected to converge to a stationary value due
 1916 to the fine binning fully sampling the small-scale structure. Figure 7.9 illustrates this
 1917 behaviour for the SubGeV_elike_0dcy sample for 30 different throws of the oscillation
 1918 parameters.

1919 Denoting the event rate for one sample for a given throw t at each N by λ_t^N , the
 1920 average over all considered N values ($\bar{\lambda}_t = \frac{1}{24} \sum_{N=1}^{24} \lambda_t^N$) is computed. The variance in
 1921 the event rate at each N is then calculated as

$$\text{Var}[\lambda^N] = \frac{1}{N_{\text{throws}}} \sum_{t=1}^{N_{\text{throws}}} (\lambda_t^N - \bar{\lambda}_t)^2 - \left[\frac{1}{N_{\text{throws}}} \sum_{t=1}^{N_{\text{throws}}} (\lambda_t^N - \bar{\lambda}_t) \right]^2. \quad (7.5)$$

1922 The aim of the study is to find the lowest value of N such that this variance is
 1923 below 0.001. This is the typical threshold used by T2K fitters to validate systematic
 1924 implementation so has been set as the same criteria. The results of this study for
 1925 each atmospheric sample used within this thesis are illustrated in Figure 7.10 for

SubGeV-elike-0dcy

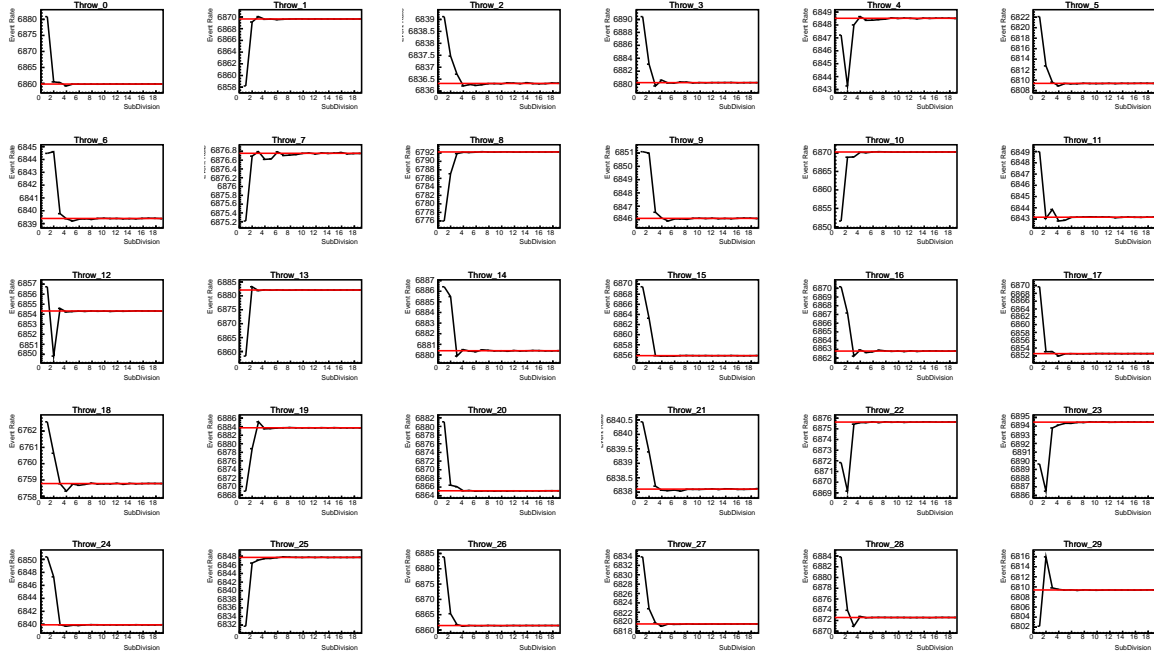


Figure 7.9: Event rate of the SubGeV_elike_0dcy sample as a function of the number of subdivisions per coarse bin. Each subplot represents the event rate of the sample at a different oscillation parameter set thrown from the PDG priors detailed in Table 2.1. The red line in each subplot represents the mean of the event rate over the different values of sub-divisions for that particular oscillation parameter throw.

1926 2000 throws of the oscillation parameters. As can be seen, the variance is below
 1927 the threshold at $N = 10$, and is driven primarily by the SubGeV_mulike_1dcy and
 1928 SubGeV_elike_0dcy samples.

1929 The second study to determine the value of N is as follows. The likelihood for each
 1930 sample is computed against an Asimov data set created with Asimov A oscillation
 1931 parameters (Table 2.2). Following Equation 7.5, the variance of the log-likelihood over
 1932 all considered N is computed. The results are shown in Figure 7.11.

1933 A choice of $N = 10$ sub-divisions per coarse bin has a variance in both event rate
 1934 and log-likelihood residuals less than the required threshold of 0.001. The largest
 1935 value of the likelihood variance is of order 10^{-7} , corresponding to an error on the log-

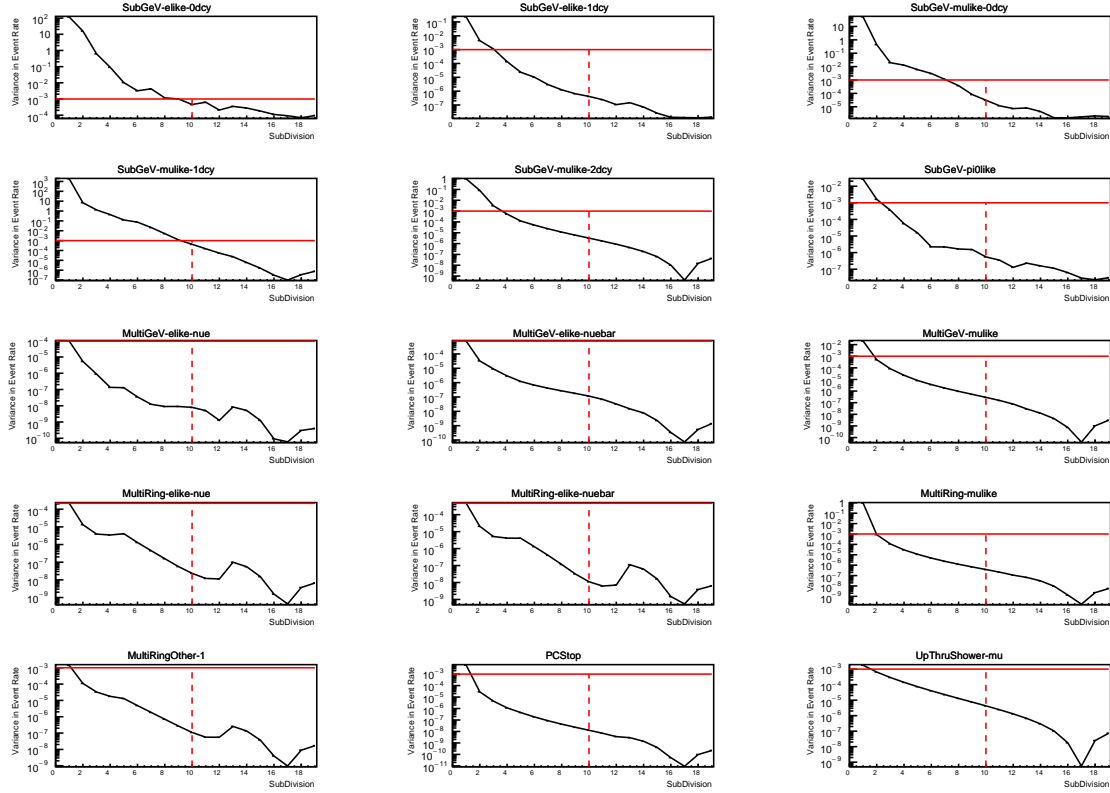


Figure 7.10: Variance of event rate for each atmospheric sample as a function of the number of sub-divisions per coarse bin. The solid red line indicates the 0.1% threshold and the dashed red line indicates the variance at a sub-division $N = 10$.

1936 likelihood of about 3×10^{-4} which is small enough to be negligible for the oscillation
 1937 analysis.

1938 Figure 7.12 illustrates the effect of the smearing using $N = 10$. The fast oscillations
 1939 in the sub-GeV upgoing region have been replaced with a normalisation effect whilst
 1940 the large matter resonance structure remains.

1941 7.3 Calculation Engine

1942 As previously discussed in section 7.2, the calculation of oscillation probabilities is per-
 1943 formed at run-time due to utilising continuous oscillation parameters. Consequently,
 1944 the time per calculation is crucial for fit performance. The initial fitting framework

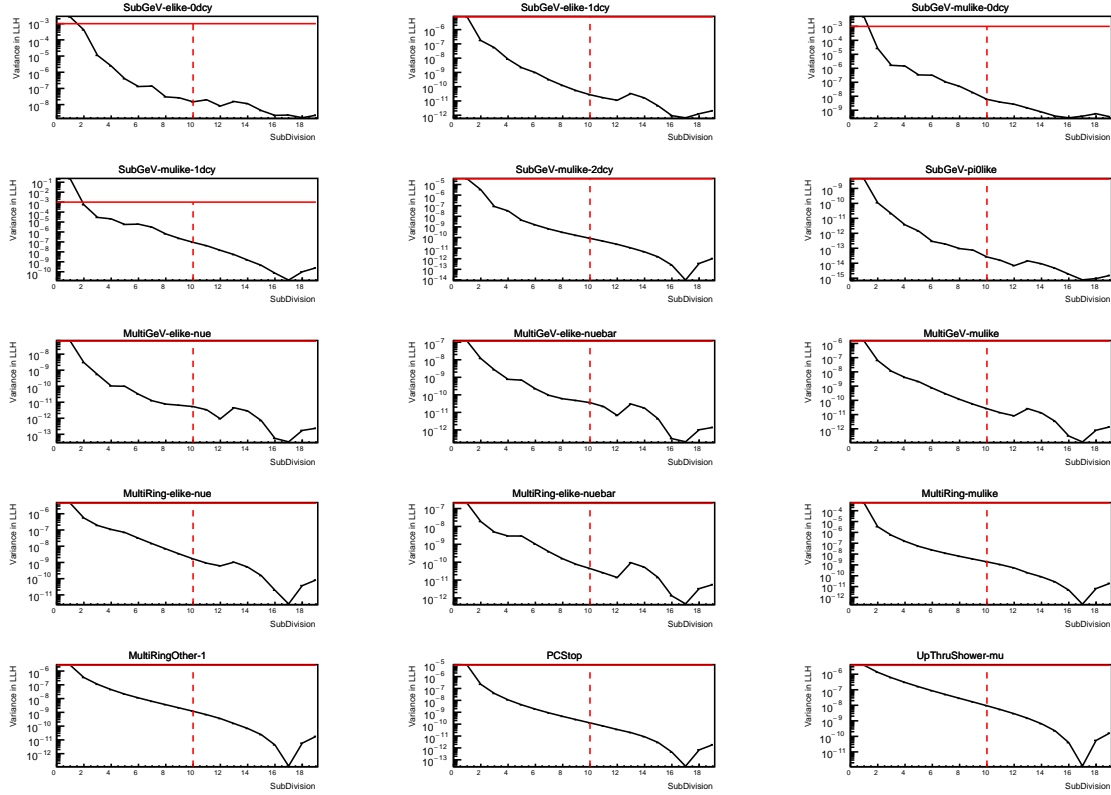


Figure 7.11: Variance of sample likelihood, when compared to ‘Asimov data’ set at Asimov A, for each atmospheric sample as a function of the number of sub-divisions per coarse bin. The solid red line indicates the 0.1% threshold and the dashed red line is a graphical indication of the variance at a sub-division $N = 10$.

1945 used for this analysis was developed with ProbGPU [195]. This is a GPU-only implemen-
 1946 tation of the prob3 engine [196]. It is primarily designed for neutrino propagation in a
 1947 beam experiment (single layer of constant density) with the atmospheric propagation
 1948 code not being used prior to the analysis in this thesis.

1949 Another engine, CUDAProb3 [197], has been implemented within the fitting frame-
 1950 work used in this analysis. It has been specifically optimised for atmospheric neutrino
 1951 oscillation calculation so does not contain the code to replace the beam oscillation
 1952 calculation. The engine utilises object-orientated techniques as compared to the func-
 1953 tional implementation of ProbGPU. This allows the energy and cosine zenith arrays to
 1954 be kept on GPU memory, rather than having to load these arrays onto GPU memory
 1955 for each calculation. General memory interfacing is one of the slowest tasks which

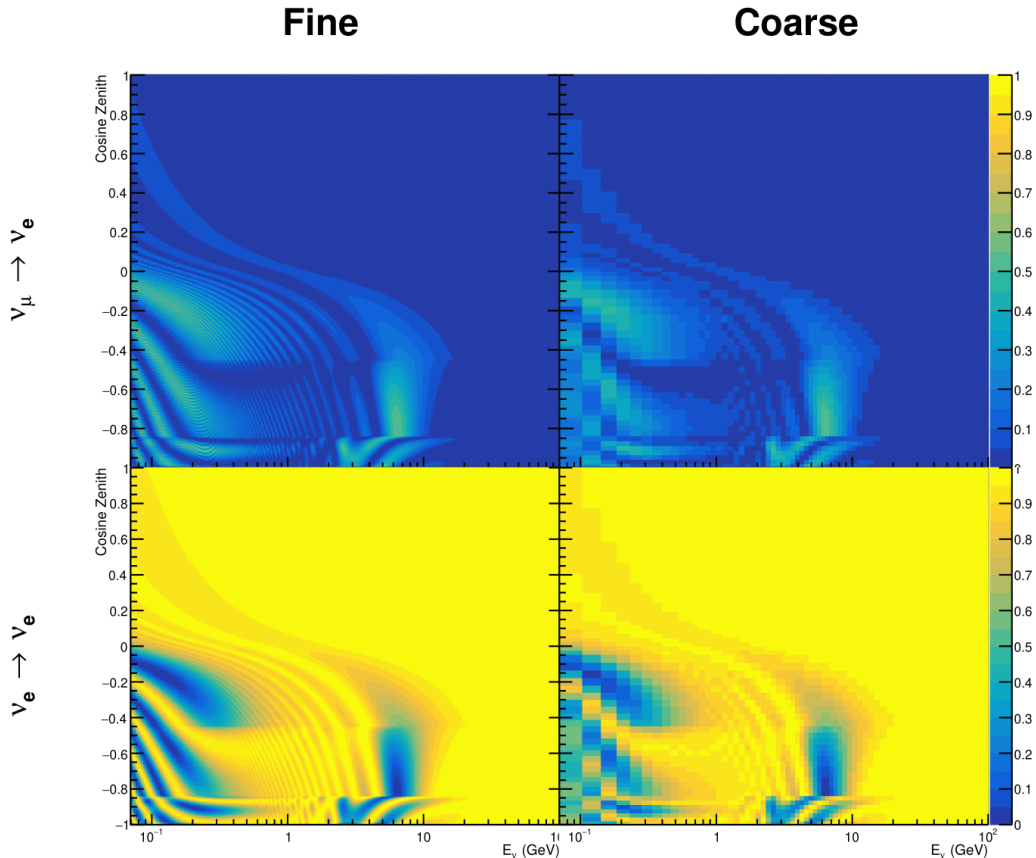


Figure 7.12: The oscillation probability, $P(\nu_\mu \rightarrow \nu_e)$ (top row) and $P(\nu_e \rightarrow \nu_e)$ (bottom row), given as a function of neutrino energy and zenith angle. The left column gives the “fine” binning used to calculate the oscillation probabilities and the right column illustrates the “coarse” binning used to reweight the Monte Carlo events. The fine binning choice is given with $N = 10$, which was determined to be below the threshold from Figure 7.10 and Figure 7.11.

1956 GPUs can do, so being able to eliminate this significantly reduces the time required
 1957 for calculation. This can be seen in Figure 7.13, where the GPU implementation of
 1958 CUDAProb3 is approximately three times faster than the ProbGPU engine.

1959 Another significant advantage of CUDAProb3 is that it contains a CPU multithreaded
 1960 implementation which is not possible with the ProbGPU or prob3 engines. This elimi-
 1961 nates the requirement for GPU resources when submitting jobs to batch systems. As
 1962 illustrated in Figure 7.13, the calculation speed depends on the number of available

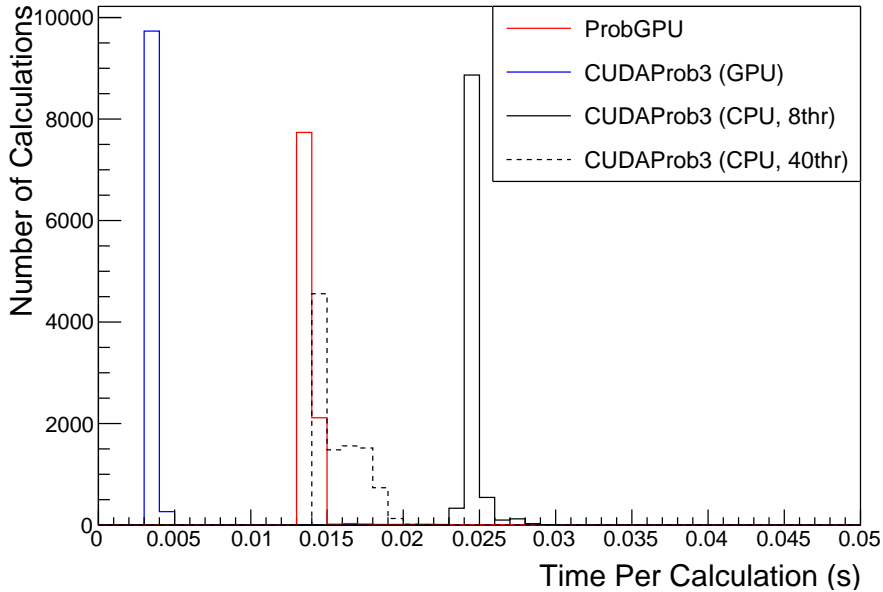


Figure 7.13: The calculation time taken to both calculate the oscillation probabilities and fill the “coarse” oscillograms, following the technique given in section 7.2, for the CUDAProb3 and ProbGPU (Red) calculation engines. CUDAProb3 has both a GPU (Blue) and CPU (Black) implementation, where the CPU implementation is multithreaded. Therefore, 8-threads (solid) and 40-threads (dashed) configurations have been tested. Prob3, which is a CPU single-thread implementation has a mean step time of 1.142s.

₁₉₆₃ threads. Using 8 threads (which is typical of the batch systems being used) is approximately twice as slow as the ProbGPU engine implementation, but would allow the fitting framework to be run on many more resources. This fact is utilised for any SK-only fits but GPU resources are required for any fits which include beam samples due to the ProbGPU requirement. Based on the benefits shown by the implementation in this section, efforts are being placed into including linear propagation for beam neutrino propagation into the engine [198].

₁₉₇₀ 7.4 Matter Density Profile

₁₉₇₁ For an experiment observing atmospheric neutrinos propagating through the Earth, a model of the Earth’s density profile is required. The model used within this analysis is

1973 the Preliminary Reference Earth Model (PREM) [193], as illustrated in Figure 7.1. As
1974 discussed in section 7.1, the propagator used within the calculation engine requires
1975 constant density layers. To follow the official SK-only analysis [192], the average
1976 density of each layer has been taken from the PREM model. Table 7.1 documents
1977 the density and radii of the layers used within this approximation. The density
1978 measurements provided in the PREM model are provided in terms of mass density,
1979 whereas neutrino oscillations are sensitive to the electron number density. This value
1980 can be computed as the product of the chemical composition, or the Z/A value, and
1981 the mass density of each layer. Currently, the only way to calculate the chemical
1982 composition value for layers close to the Earth’s core is through neutrino oscillations.
1983 The chemical composition of the upper layers of the Earth’s Mantle and the Transition
1984 zone is well known due to it being predominantly pyrolite which has a chemical
1985 composition value of 0.496 [199]. The components of the Earth’s core region are less
1986 well known. Consequently, the chemical composition dial for the core layers is set to a
1987 value of 0.468, as calculated in [200]. This value is assigned a Gaussian error with a
1988 standard deviation equivalent to the difference in chemical composition in core and
1989 mantle layers. Figure 7.14 illustrates the effect of moving from the $Z/A = 0.5$ method
1990 which is used in the official SK-only analysis [192] to these more precise values.

1991 The beam oscillation probability in this thesis uses a baseline of 295km, density
1992 2.6g/cm^3 , and chemical composition 0.5 as is done by the official T2K-only analysis
1993 [201].

1994 Whilst the propagator requires a fixed density layer model of the Earth, the density
1995 only has to be fixed for a specific $E_\nu \times \cos(\theta_Z)$ bin in a given layer. As the density is a
1996 function of radius, which is a function of the direction in which a neutrino propagates,
1997 a better approximation of the PREM model can be made if a $\cos(\theta_Z)$ -specific density is
1998 calculated.

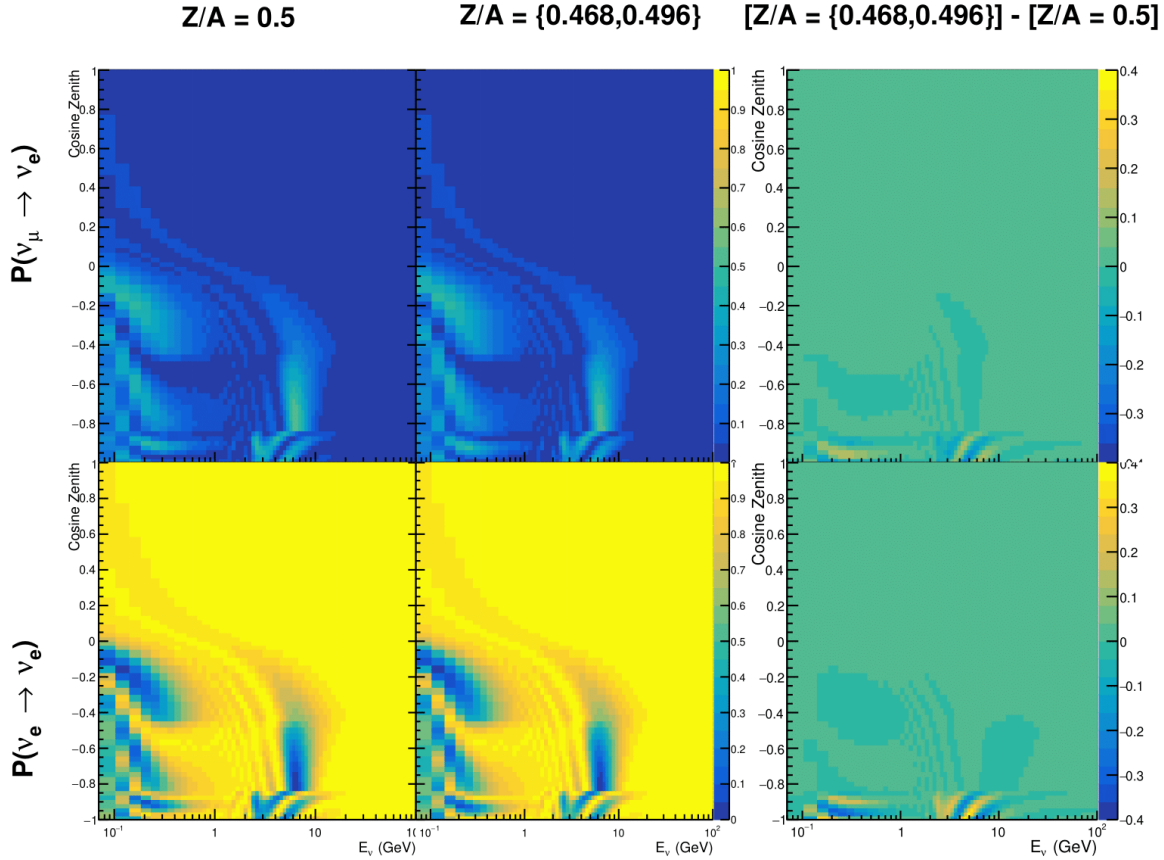


Figure 7.14: The oscillation probability, $P(\nu_\mu \rightarrow \nu_e)$ (top row) and $P(\nu_e \rightarrow \nu_e)$ (bottom row), given as a function of neutrino energy and zenith angle. The left column gives probabilities where the constant $Z/A = 0.5$ approximation which is used in the official SK-only analysis. The middle column gives the probabilities where $Z/A = [0.468, 0.498]$ values are used, as given in Table 7.1. The right column illustrates the difference in oscillation probability between the two different techniques.

1999 To achieve this, the average density, $\langle \rho \rangle_i$, in the i^{th} layer, is calculated as the density,

2000 $\rho(t)$, integrated over the track a given $\cos(\theta_Z)$,

$$\langle \rho \rangle_i = \frac{1}{t_{i+1} - t_i} \int_{t_i}^{t_{i+1}} \rho(t) dt \quad (7.6)$$

2001 where t_i are the intersection points between each layer and t is the path length of
 2002 the trajectory across the layer.

2003 The oscillation probability calculation speed is approximately linear in the number
 2004 of layers invoked within the Earth model. Therefore a four-layer model is still utilized
 2005 with the only difference to the official SK-only analysis being that the four-layer model
 2006 used for each value of $\cos(\theta_Z)$ is different. Following the method outlined in [202],
 2007 a four-layer piecewise quadratic polynomial is fit to the PREM model for the four
 2008 layers defined in Table 7.1. This fit was not performed by the author of the thesis
 2009 and is documented in [194]. The coefficients of the quadratic fit to each layer are
 2010 given in Table 7.2 with the final distribution illustrated in Figure 7.15. The quadratic
 2011 approximation is clearly much closer to the PREM model as compared to the constant
 2012 density approximation.

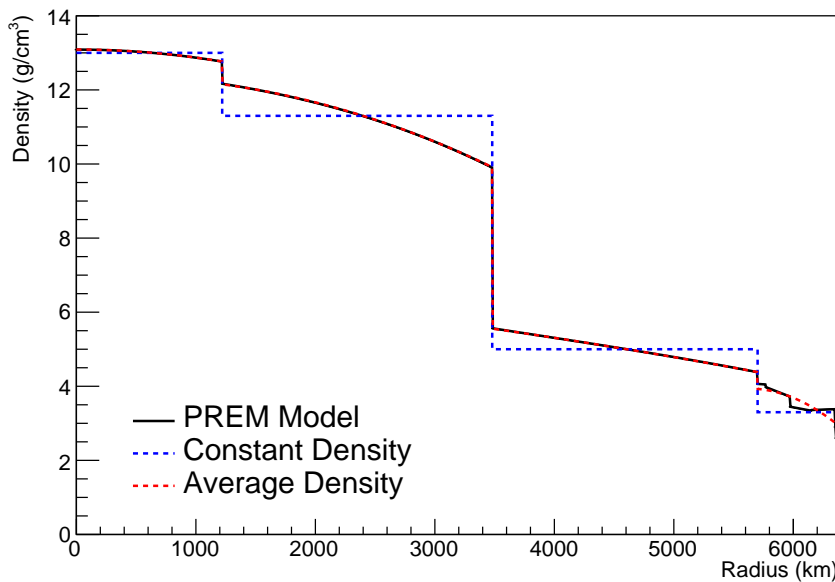


Figure 7.15: The density of the Earth given as a function of the radius, as given by the PREM model (Black), the constant density four-layer approximation (Blue), as used in the official SK-only analysis, and the quadratic approximation of the PREM model (Red).

Layer	Outer Radius [km]	Density [g/cm ³]
Inner Core	1220	$13.09 - 8.84x^2$
Outer Core	3480	$12.31 + 1.09x - 10.02x^2$
Lower Mantle	5701	$6.78 - 1.56x - 1.25x^2$
Transition Zone	6371	$-50.42 + 123.33x - 69.95x^2$

Table 7.2: The quadratic polynomial fits to the PREM model for four assumed layers of the PREM model. The fit to calculate the coefficients is given in [194], where $x = R/R_{Earth}$.

2013 The effect of using the quadratic density per $\cos(\theta_Z)$ model is highlighted in
 2014 Figure 7.16. The slight discontinuity in the oscillation probability around $\cos(\theta_Z) \sim -$
 2015 0.45 in the fixed density model, which is due to the transition to mantle layer boundary,
 2016 has been reduced. This is expected as the difference in the density across this boundary
 2017 is significantly smaller in the quadratic density model as compared to the constant
 2018 density model. Whilst the difference in density across the other layer transitions
 2019 is reduced, there is still a significant difference. This means the discontinuities in
 2020 the oscillation probabilities remain but are significantly reduced. However, as the
 2021 quadratic density approximation matches the PREM model well in this region, these
 2022 discontinuities are due to the Earth model rather than an artifact of the oscillation
 2023 calculation.

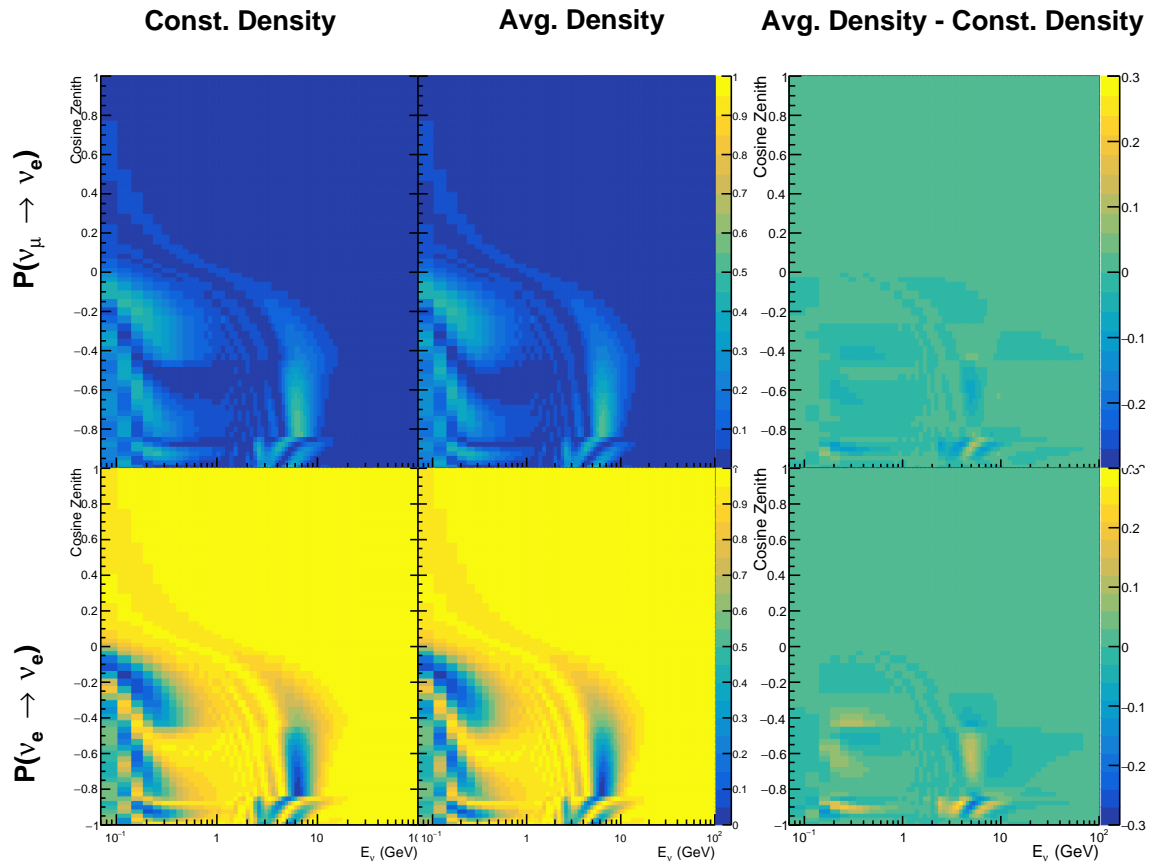


Figure 7.16: The oscillation probability, $P(\nu_\mu \rightarrow \nu_e)$ (top row) and $P(\nu_e \rightarrow \nu_\mu)$ (bottom row), given as a function of neutrino energy and zenith angle. The left column gives probabilities where the four-layer constant density approximation is used. The middle column gives the probabilities where the density is integrated over the trajectory, using the quadratic PREM approximation, for each $\cos(\theta_Z)$ is used. The right column illustrates the difference in oscillation probability between the two different techniques.

2024 7.5 Production Height Averaging

2025 As discussed in section 7.1, the height at which the cosmic ray flux interacts in the
 2026 atmosphere is not known on an event-by-event basis. The production height can vary
 2027 from the Earth’s surface to $\sim 50\text{km}$ above that. The SK-only analysis methodology
 2028 (described in section 7.2) for including the uncertainty on the production height is
 2029 to include variations from the Honda model when pre-calculating the oscillation
 2030 probabilities prior to the fit. This technique is not possible for this analysis which
 2031 uses continuous oscillation parameters that can not be known prior to the fit. Conse-
 2032 quently, an analytical averaging technique was developed in [194]. The author of this
 2033 thesis was not responsible for the derivation of the technique but has performed the
 2034 implementation and validation of the technique for this analysis alone.

2035 Using the 20 production heights per Monte Carlo neutrino event, provided as 5%
 2036 percentiles from the Honda flux model, a production height distribution $p_j(h|E_\nu, \cos \theta_Z)$
 2037 is built for each neutrino flavour $j = \nu_e, \bar{\nu}_e, \nu_\mu, \bar{\nu}_\mu$. In practice, a histogram is filled with
 2038 20 evenly spaced bins in production height h between 0 and 50km. The neutrino energy
 2039 and cosine zenith binning of the histogram is the same as that provided in section 7.2.
 2040 The average production height, $\bar{h} = \int dh \frac{1}{4} \sum_j p_j(h|E_\nu, \cos(\theta_Z))$, is calculated. The
 2041 production height binning of this histogram is then translated into $\delta t(h) = t(\bar{h}) - t(h)$,
 2042 where $t(h)$ is the distance travelled along the trajectory.

2043 For the i^{th} traversed layer, the transition amplitude, $D_i(t_{i+1}, t_i)$, is computed. The
 2044 time-ordered product of these is then used as the overall transition amplitude via

$$A(t_{n+1}, t_0) = D_n(t_{n+1}, t_n) \dots D_1(t_2, t_1) D_0(t_1, t_0), \quad (7.7)$$

2045

where,

$$\begin{aligned} D_n(t_{n+1}, t_n) &= \exp[-iH_n(t_{n+1} - t_n)] \\ &= \sum_{k=1}^3 C_k \exp[ia_k(t_{n+1} - t_n)] \end{aligned} \quad (7.8)$$

2046

is expressed as a diagonalised time-dependent solution to the Schrodinger equation.

2047

The 0^{th} layer is the propagation through the atmosphere and is the only term that depends on the production height. Using the substitution $t_0 = t(\bar{h}) - \delta t(h)$, it can be shown that

2050

Thus Equation 7.7 becomes

$$\begin{aligned} A(t_{n+1}, t_0) &= D_n(t_{n+1}, t_n) \dots D_1(t_2, t_1) D_0(t_1, \bar{h}) D(\delta t) \\ &= A(t_{n+1}, \bar{h}) \sum_{k=1}^3 C_k \exp[ia_k \delta t], \\ &= \sum_{k=1}^3 B_k \exp[ia_k \delta t]. \end{aligned} \quad (7.10)$$

2051

The oscillation probability averaged over production height is then calculated as

$$\begin{aligned}
 \bar{P}(\nu_j \rightarrow \nu_i) &= \int d(\delta t) p_j(\delta t | E_\nu, \cos \theta_Z) P(\nu_j \rightarrow \nu_i) \\
 &= \int d(\delta t) p_j(\delta t | E_\nu, \cos \theta_Z) A(t_{n+1}, t_0) A^*(t_{n+1}, t_0) \\
 &= \sum_{km} (B_k)_{ij} (B_m)_{ij}^* \int d(\delta t) p_j(\delta t | E_\nu, \cos \theta_Z) \exp[i(a_k - a_m)\delta t]
 \end{aligned} \tag{7.11}$$

2052 In practice, implementation in CUDAProb3 [197] is relatively straightforward as
 2053 the majority of these terms are already calculated in the standard oscillation calculation.
 2054 Figure 7.17 illustrates the results of the production height averaging. As expected,
 2055 the main effect is observed in the low-energy downward-going and horizontal-going
 2056 events. Upward-going events have to travel the radius of the Earth, $R_E = 6371\text{km}$,
 2057 where the production height uncertainty is a small fraction of the total path length.

2058

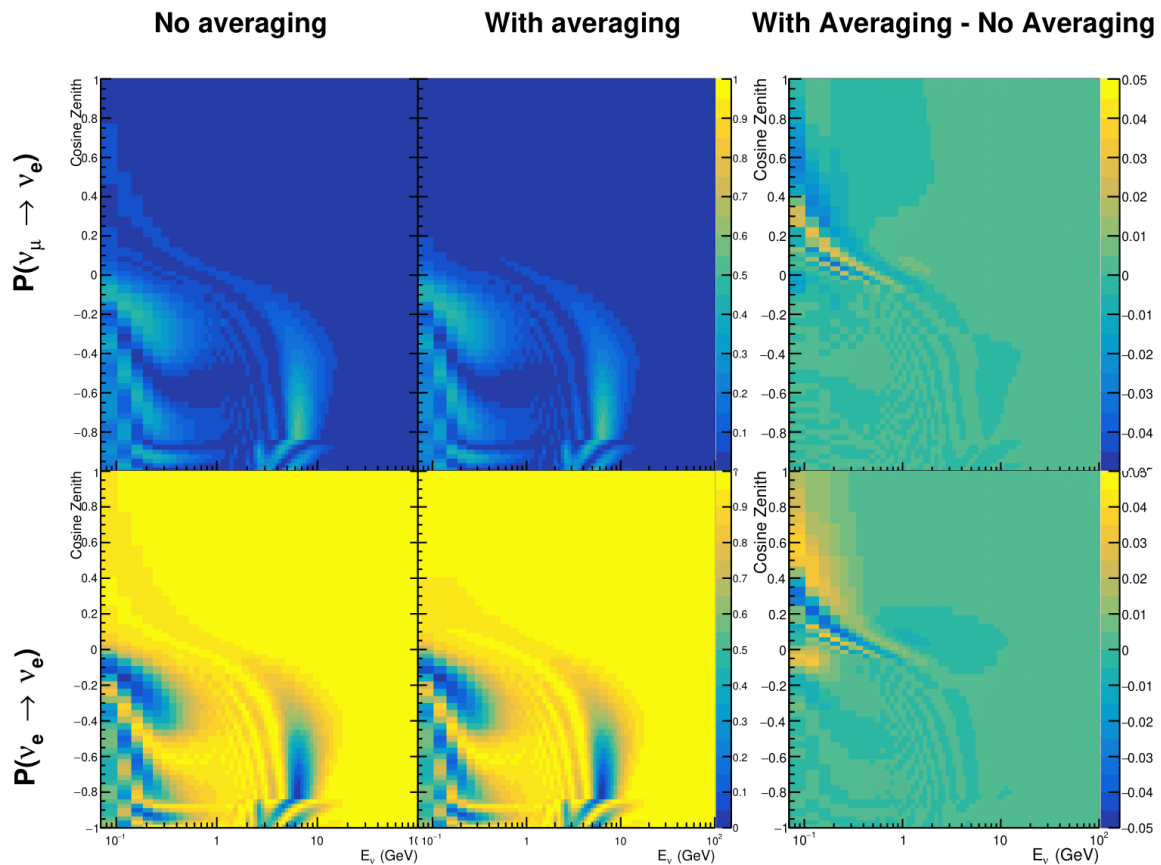


Figure 7.17: The oscillation probability, $P(\nu_\mu \rightarrow \nu_e)$ (top row) and $P(\nu_e \rightarrow \nu_\mu)$ (bottom row), given as a function of neutrino energy and zenith angle. The left column gives probabilities where a fixed production height of 25km is used. The middle column gives the probabilities where the production height is analytically averaged. The right column illustrates the difference in oscillation probability between the two different techniques.

2059 **Bibliography**

- 2060 [1] J. Chadwick, Verhandl. Dtsc. Phys. Ges. **16**, 383 (1914).
- 2061 [2] C. D. Ellis and W. A. Wooster, Proc. R. Soc. Lond. A Math. Phys. Sci. **117**, 109
2062 (1927).
- 2063 [3] W. Pauli, Phys. Today **31N9**, 27 (1978).
- 2064 [4] E. Fermi, Z. Phys. **88**, 161 (1934).
- 2065 [5] F. Reines and C. L. Cowan, Phys. Rev. **92**, 830 (1953).
- 2066 [6] C. L. Cowan, F. Reines, F. B. Harrison, H. W. Kruse, and A. D. McGuire, Science
2067 **124**, 103 (1956), <http://science.sciencemag.org/content/124/3212/103.full.pdf>.
- 2068 [7] G. Danby *et al.*, Phys. Rev. Lett. **9**, 36 (1962).
- 2069 [8] K. Kodama *et al.*, Physics Letters B **504**, 218 (2001).
- 2070 [9] LSND, A. Aguilar-Arevalo *et al.*, Phys. Rev. **D64**, 112007 (2001), hep-ex/0104049.
- 2071 [10] MiniBooNE Collaboration, A. A. Aguilar-Arevalo *et al.*, Phys. Rev. Lett. **110**,
2072 161801 (2013).
- 2073 [11] Planck Collaboration *et al.*, aap **641** (2020).
- 2074 [12] The ALEPH Collaboration, The Delphi Collaboration, The L3 Collaboration, The
2075 SLD Collaboration, The LEP Electroweak Working Group, The SLD Electroweak
2076 and Heavy Flavour Groups, J. A. Bagger *et al.*, Physics Reports **427**, 257 (2006).
- 2077 [13] B. Pontecorvo, Sov. Phys. JETP **26**, 984 (1968), [Zh. Eksp. Teor. Fiz. 53, 1717 (1967)].
- 2078 [14] B. Pontecorvo, Sov. Phys. JETP **7**, 172 (1958), [Zh. Eksp. Teor. Fiz. 34, 247 (1957)].
- 2079 [15] M. Kobayashi and T. Maskawa, Progress of Theoretical Physics **49**, 652 (1973).
- 2080 [16] N. Cabibbo, Phys. Rev. Lett. **10**, 531 (1963).
- 2081 [17] A. M. and, Journal of Physics: Conference Series **587**, 012030 (2015).
- 2082 [18] A. Y. Smirnov, (2003).
- 2083 [19] S. Mikheyev and A. Smirnov, Soviet Journal of Nuclear Physics **42**, 913 (1985).

- 2084 [20] L. Wolfenstein, Phys. Rev. D **17**, 2369 (1978).
- 2085 [21] V. D. Barger, K. Whisnant, S. Pakvasa, and R. J. N. Phillips, Phys. Rev. D **22**, 2718
2086 (1980).
- 2087 [22] The Super-Kamiokande Collaboration, Y. Ashie *et al.*, Phys. Rev. Lett. **93**, 101801
2088 (2004).
- 2089 [23] SNO Collaboration, Q. R. Ahmad *et al.*, Phys. Rev. Lett. **89**, 011301 (2002).
- 2090 [24] 2015 Nobel prize in Physics as listed by Nobelprize.org, [https://www.](https://www.nobelprize.org/nobel_prizes/physics/laureates/2015/)
2091 [nobelprize.org/nobel_prizes/physics/laureates/2015/](https://www.nobelprize.org/nobel_prizes/physics/laureates/2015/), Accessed: 22-06-
2092 2022.
- 2093 [25] J. A. Formaggio and G. P. Zeller, Rev. Mod. Phys. **84**, 1307 (2012), 1305.7513.
- 2094 [26] A. Bellerive, Int. J. Mod. Phys. A **19**, 1167 (2004).
- 2095 [27] R. Davis, D. S. Harmer, and K. C. Hoffman, Phys. Rev. Lett. **20**, 1205 (1968).
- 2096 [28] N. Vinyoles *et al.*, Astrophys. J. **835**, 202 (2017).
- 2097 [29] V. Gribov and B. Pontecorvo, Phys. Lett. B **28**, 493 (1969).
- 2098 [30] K. S. Hirata *et al.*, Phys. Rev. Lett. **63**, 16 (1989).
- 2099 [31] W. Hampel *et al.*, Phys. Lett. B **447**, 127 (1999).
- 2100 [32] SAGE Collaboration, J. N. Abdurashitov *et al.*, Phys. Rev. C **60**, 055801 (1999).
- 2101 [33] Q. R. Ahmad *et al.*, Phys. Rev. Lett. **89** (2002).
- 2102 [34] Borexino Collaboration, Nature **562**, 505 (2018).
- 2103 [35] B. Aharmim *et al.*, Astrophys. J. **653**, 1545 (2006).
- 2104 [36] M. Agostini *et al.*, (2020).
- 2105 [37] S. Andringa *et al.*, Adv. High Energy Phys. **2016**, 1 (2016).
- 2106 [38] J. F. Beacom *et al.*, Chin. phys. C **41**, 023002 (2017).
- 2107 [39] F. An *et al.*, J. Phys. G Nucl. Part. Phys. **43**, 030401 (2016).
- 2108 [40] J. Aalbers *et al.*, (2020), 2006.03114.
- 2109 [41] T. K. Gaisser and M. Honda, (2002).

- 2110 [42] G. D. Barr, T. K. Gaisser, P. Lipari, S. Robbins, and T. Stanev, Physical Review D
2111 **70** (2004).
- 2112 [43] M. Honda, T. Kajita, K. Kasahara, S. Midorikawa, and T. Sanuki, Physical Review
2113 D **75** (2007).
- 2114 [44] M. Honda, T. Kajita, K. Kasahara, and S. Midorikawa, Phys. Rev. D **70**, 043008
2115 (2004).
- 2116 [45] M. Honda, T. Kajita, K. Kasahara, and S. Midorikawa, Phys. Rev. D **83**, 123001
2117 (2011).
- 2118 [46] A. Fasso, A. Ferrari, P. R. Sala, and J. Ranft, (2001).
- 2119 [47] Y. Ashie *et al.*, Physical Review D **71** (2005).
- 2120 [48] F. Reines *et al.*, Phys. Rev. Lett. **15**, 429 (1965).
- 2121 [49] D. Casper *et al.*, Phys. Rev. Lett. **66**, 2561 (1991).
- 2122 [50] K. S. Hirata *et al.*, Phys. Lett. B **280**, 146 (1992).
- 2123 [51] Z. Li *et al.*, Physical Review D **98** (2018).
- 2124 [52] Kamiokande Collaboration *et al.*, (2017).
- 2125 [53] T2K Collaboration, Nature **580**, 339 (2020).
- 2126 [54] M. A. Acero *et al.*, Phys. Rev. Lett. **123**, 151803 (2019).
- 2127 [55] M. G. Aartsen *et al.*, Phys. Rev. Lett. **120** (2018).
- 2128 [56] P. Adamson *et al.*, Phys. Rev. Lett. **112** (2014).
- 2129 [57] M. S. Athar *et al.*, Progress in Particle and Nuclear Physics **124**, 103947 (2022).
- 2130 [58] G. Danby *et al.*, Phys. Rev. Lett. **9**, 36 (1962).
- 2131 [59] K. Abe *et al.*, Physical Review D **87** (2013).
- 2132 [60] MINOS Collaboration, D. G. Michael *et al.*, Phys. Rev. Lett. **97**, 191801 (2006).
- 2133 [61] G. Danby *et al.*, Phys. Rev. Lett. **9**, 36 (1962).
- 2134 [62] NOvA Collaboration, M. A. Acero *et al.*, Phys. Rev. Lett. **123**, 151803 (2019).
- 2135 [63] B. Abi, R. Acciarri, M. A. Acero, and G. e. a. Adamov, Eur. Phys. J. C Part. Fields

- 2136 **80** (2020).
- 2137 [64] Hyper-Kamiokande Proto-Collaboration *et al.*, Prog. Theor. Exp. Phys. **2015**,
2138 53C02 (2015).
- 2139 [65] C. Blanco, D. Hooper, and P. Machado, Physical Review D **101** (2020).
- 2140 [66] MicroBooNE Collaboration *et al.*, Search for an Excess of Electron Neutrino
2141 Interactions in MicroBooNE Using Multiple Final State Topologies, 2021.
- 2142 [67] KARMEN Collaboration, B. Armbruster *et al.*, Phys. Rev. D **65**, 112001 (2002).
- 2143 [68] S.-B. Kim, T. Lasserre, and Y. Wang, Adv. High Energy Phys. **2013**, 1 (2013).
- 2144 [69] M. Sajjad Athar *et al.*, Prog. Part. Nucl. Phys. **124**, 103947 (2022), 2111.07586.
- 2145 [70] K. Abe *et al.*, Nucl. Instrum. Methods Phys. Res. A **1027**, 166248 (2022).
- 2146 [71] F. P. An *et al.*, Phys. Rev. Lett. **108**, 171803 (2012).
- 2147 [72] RENO Collaboration, J. K. Ahn *et al.*, Phys. Rev. Lett. **108**, 191802 (2012).
- 2148 [73] Double Chooz Collaboration, Y. Abe *et al.*, Phys. Rev. Lett. **108**, 131801 (2012).
- 2149 [74] J. Collaboration *et al.*, TAO Conceptual Design Report: A Precision Measurement
2150 of the Reactor Antineutrino Spectrum with Sub-percent Energy Resolution, 2020,
2151 2005.08745.
- 2152 [75] for the RENO Collaboration, New results from RENO and the 5 MeV excess,
2153 AIP Publishing LLC, 2015.
- 2154 [76] Y. Abe *et al.*, Journal of High Energy Physics **2014** (2014).
- 2155 [77] Daya Bay Collaboration, D. Adey *et al.*, Phys. Rev. Lett. **123**, 111801 (2019).
- 2156 [78] M. P. Decowski, Nucl. Phys. B. **908**, 52 (2016).
- 2157 [79] The KamLAND Collaboration, A. Gando *et al.*, Phys. Rev. D **83**, 052002 (2011).
- 2158 [80] P. Dunne, Latest Neutrino oscillation results from T2K, 2020.
- 2159 [81] M. Tanabashi *et al.*, Phys. Rev. D. **98** (2018).
- 2160 [82] Particle Data Group, R. L. Workman and Others, PTEP **2022**, 083C01 (2022).
- 2161 [83] T2K Collaboration, K. Abe *et al.*, Phys. Rev. Lett. **112**, 181801 (2014).

- [84] Y. Fukuda *et al.*, Phys. Rev. Lett. **81**, 1562 (1998).
- [85] Linyan Wan, (2022).
- [86] K. Abe *et al.*, Nuclear Instruments and Methods in Physics Research Section A: Accelerators, Spectrometers, Detectors and Associated Equipment **737**, 253 (2014).
- [87] S. Fukuda *et al.*, Nucl. Instrum. Methods Phys. Res. A **501**, 418 (2003).
- [88] Y. Itow *et al.*, (2001).
- [89] M. Jiang *et al.*, Prog. Theor. Exp. Phys. **2019** (2019).
- [90] S. Fukuda *et al.*, Nuclear Instruments and Methods in Physics Research Section A: Accelerators, Spectrometers, Detectors and Associated Equipment **501**, 418 (2003), <http://www.sciencedirect.com/science/article/pii/S016890020300425X>.
- [91] Y. Nakano *et al.*, Nucl. Instrum. Methods Phys. Res. A **977**, 164297 (2020).
- [92] Hamamatsu, Hamamatsu Photonics Photomultiplier Tubes Handbook.
- [93] K. Abe *et al.*, Nucl. Instrum. Methods Phys. Res. A **1027**, 166248 (2022).
- [94] J. F. Beacom and M. R. Vagins, Phys. Rev. Lett. **93**, 171101 (2004).
- [95] L. Marti *et al.*, Nucl. Instrum. Methods Phys. Res. A **959**, 163549 (2020).
- [96] L. Marti *et al.*, (2019).
- [97] M. Vagins, Solar/DSNB Neutrino_SK-Gd, 2022.
- [98] J. Focht, PhD thesis, Massachusetts Institute of Technology, 2004.
- [99] T. Tanimori *et al.*, IEEE Transactions on Nuclear Science **36**, 497 (1989).
- [100] Super-Kamiokande Collaboration, J. Hosaka *et al.*, Phys. Rev. D **73**, 112001 (2006).
- [101] H. Nishino *et al.*, Nucl. Instrum. Methods Phys. Res. A **610**, 710 (2009).
- [102] S. Yamada *et al.*, IEEE Transactions on Nuclear Science **57**, 428 (2010).
- [103] S. Yamada, Y. Hayato, Y. Obayashi, and M. Shiozawa, New online system without hardware trigger for the Super-Kamiokande experiment, in *2007 IEEE Nuclear Science Symposium Conference Record*, IEEE, 2007.

- 2189 [104] G. Carminati, Phys. Procedia **61**, 666 (2015).
- 2190 [105] P. A. Čerenkov, Phys. Rev. **52**, 378 (1937).
- 2191 [106] I. Frank and I. Tamm, Coherent visible radiation of fast electrons passing
2192 through matter, in *Selected Papers*, pp. 29–35, Springer Berlin Heidelberg, Berlin,
2193 Heidelberg, 1991.
- 2194 [107] The T2K Collaboration, KEK Proposal (2001),
2195 <http://neutrino.kek.jp/jhfnu/loi/loi.v2.030528.pdf>.
- 2196 [108] Y. Itow *et al.*, (2001), hep-ex/0106019.
- 2197 [109] The K2K Collaboration and S. H. Ahn, (2001), hep-ex/0103001.
- 2198 [110] The T2K Collaboration, KEK Proposal (2006), http://j-parc.jp/researcher/Hadron/en/pac_0606/pdf/p11-Nishikawa.pdf.
- 2200 [111] C. Bronner, Accelerator Neutrino I_Recent results from T2K, 2022.
- 2201 [112] T2K Collaboration, K. Abe *et al.*, Phys. Rev. Lett. **112**, 061802 (2014),
2202 <https://link.aps.org/doi/10.1103/PhysRevLett.112.061802>.
- 2203 [113] NINJA Collaboration, T. Fukuda *et al.*, Proposal for precise measurement of
2204 neutrino-water cross-section in NINJA physics run, Proposal for J-PARC and
2205 KEK, 2017.
- 2206 [114] T. Ovsiannikova *et al.*, Physics of Particles and Nuclei **48**, 1014 (2017),
2207 <https://doi.org/10.1134/S1063779617060478>.
- 2208 [115] M. Antonova *et al.*, Journal of Instrumentation **12**, C07028 (2017),
2209 <http://stacks.iop.org/1748-0221/12/i=07/a=C07028>.
- 2210 [116] The T2K Collaboration, K. Abe *et al.*, Phys. Rev. D **102**, 012007 (2020).
- 2211 [117] K. Abe *et al.*, Progress of Theoretical and Experimental Physics **2021** (2021).
- 2212 [118] The T2K Collaboration, K. Abe *et al.*, Nuclear Instruments
2213 and Methods in Physics Research Section A: Accelerators, Spectrometers,
2214 Detectors and Associated Equipment **659**, 106 (2011),
2215 <http://www.sciencedirect.com/science/article/pii/S0168900211011910>.
- 2216 [119] K. Matsuoka *et al.*, Nuclear Instruments and Methods in Physics Research Section
2217 A: Accelerators, Spectrometers, Detectors and Associated Equipment **624**, 591

- 2218 (2010), <http://www.sciencedirect.com/science/article/pii/S016890021002098X>.
- 2219 [120] K. Abe *et al.*, Phys. Rev. D. **103** (2021).
- 2220 [121] T. Vladisavljevic, *Predicting the T2K neutrino flux and measuring oscillation parameters* Springer theses, 1 ed. (Springer Nature, Cham, Switzerland, 2020).
- 2221
- 2222 [122] D. Beavis, A. Carroll, and I. Chiang, (1995).
- 2223 [123] P.-A. Amaudruz *et al.*, Nuclear Instruments and Methods in Physics Research
2224 Section A: Accelerators, Spectrometers, Detectors and Associated Equipment
2225 **696**, 1 (2012).
- 2226 [124] N. Abgrall *et al.*, Nuclear Instruments and Methods in Physics Research Section
2227 A: Accelerators, Spectrometers, Detectors and Associated Equipment **637**, 25
2228 (2011).
- 2229 [125] S. Assylbekov *et al.*, Nuclear Instruments and Methods in Physics Research
2230 Section A: Accelerators, Spectrometers, Detectors and Associated Equipment
2231 **686**, 48 (2012).
- 2232 [126] D. Allan *et al.*, Journal of Instrumentation **8**, P10019 (2013).
- 2233 [127] F. Vannucci, Advances in High Energy Physics **2014**, 1 (2014).
- 2234 [128] UA1 magnet sets off for a second new life, 2022.
- 2235 [129] S. Aoki *et al.*, Nuclear Instruments and Methods in Physics Research Section
2236 A: Accelerators, Spectrometers, Detectors and Associated Equipment **698**, 135
2237 (2013).
- 2238 [130] K. Suzuki *et al.*, Progress of Theoretical and Experimental Physics **2015**, 53C01
2239 (2015).
- 2240 [131] S. Brooks, A. Gelman, G. L. Jones, and X.-L. Meng, *Handbook of Markov Chain
Monte Carlo* (CRC Press, 2011).
- 2241
- 2242 [132] W. R. Gilks, S. Richardson, and D. J. Spiegelhalter, *Markov Chain Monte Carlo in
Practice* (Chapman & Hall/CRC Interdisciplinary Statistics, 1995).
- 2243
- 2244 [133] C. Wret, *Minimising systematic uncertainties in the T2K experiment using near-
detector and external data*, PhD thesis, Imperial College London, 2018.
- 2245
- 2246 [134] K. E. Duffy, *Measurement of the Neutrino Oscillation Parameters $\sin^2 \theta_{23}$, Δm_{32}^2 ,*

- 2247 $\sin^2 \theta_{13}$, and δ_{CP} in Neutrino and Antineutrino Oscillation at T2K, PhD thesis, Oriel
2248 College, University of Oxford, 2016.
- 2249 [135] T. Bayes, Rev. Phil. Trans. Roy. Soc. Lond. **53**, 370 (1764).
- 2250 [136] N. Metropolis, A. W. Rosenbluth, M. N. Rosenbluth, A. H. Teller, and E. Teller,
2251 Journal of Chemical Physics **21** (1970).
- 2252 [137] W. K. Hastings, Biometrika **57** (1970).
- 2253 [138] J. Dunkley, M. Bucher, P. G. Ferreira, K. Moodley, and C. Skordis, Mon. Not. R.
2254 Astron. Soc. **356**, 925 (2005).
- 2255 [139] Particle Data Group *et al.*, Prog. Theor. Exp. Phys. **2020** (2020).
- 2256 [140] H. Jeffreys, *The Theory of Probability* Oxford Classic Texts in the Physical Sciences
2257 (, 1939).
- 2258 [141] R. E. Kass and A. E. Raftery, J. Am. Stat. Assoc. **90**, 773 (1995).
- 2259 [142] T. Böhlen *et al.*, Nuclear Data Sheets **120**, 211 (2014),
2260 <http://www.sciencedirect.com/science/article/pii/S0090375214005018>.
- 2261 [143] R. Brun *et al.*, GEANT: Detector Description and Simulation Tool; Oct 1994 CERN
2262 Program Library (CERN, Geneva, 1993), <http://cds.cern.ch/record/1082634>,
2263 Long Writeup W5013.
- 2264 [144] T2K Collaboration, K. Abe *et al.*, Phys. Rev. D **87**, 012001 (2013).
- 2265 [145] C. Zeitnitz and T. Gabriel, Nuclear Instruments and Methods in Physics Research Section A: Accelerators, Spectrometers, Detectors and Associated Equipment **349**, 106 (1994),
2266 <http://www.sciencedirect.com/science/article/pii/0168900294906130>.
- 2269 [146] A. Fiorentini *et al.*, T2K Technical Note **217** (2017).
- 2270 [147] N. Abgrall *et al.*, Physical Review C **84** (2011).
- 2271 [148] N. Abgrall *et al.*, Physical Review C **85** (2012).
- 2272 [149] N. Abgrall *et al.*, Nuclear Instruments and Methods in Physics Research Section
2273 A: Accelerators, Spectrometers, Detectors and Associated Equipment **701**, 99
2274 (2013), <http://www.sciencedirect.com/science/article/pii/S016890021201234X>.

- 2275 [150] HARP Collaboration, M. Apollonio *et al.*, Phys. Rev. C **80**, 035208 (2009),
2276 <https://link.aps.org/doi/10.1103/PhysRevC.80.035208>.
- 2277 [151] B. Blau *et al.*, Nuclear Physics B - Proceedings Supplements **113**, 125 (2002).
- 2278 [152] S. Haino *et al.*, Physics Letters B **594**, 35 (2004).
- 2279 [153] NASA, U.S. Standard Atmosphere, 1976, 1976.
- 2280 [154] S. Roesler, R. Engel, and J. Ranft, The Monte Carlo Event Generator DPMJET-III,
2281 in *Advanced Monte Carlo for Radiation Physics, Particle Transport Simulation and*
2282 *Applications*, pp. 1033–1038, Springer Berlin Heidelberg, 2001.
- 2283 [155] K. Niita *et al.*, Radiation Measurements **41**, 1080 (2006).
- 2284 [156] T. Sanuki *et al.*, Physics Letters B **541**, 234 (2002).
- 2285 [157] P. Achard *et al.*, Physics Letters B **598**, 15 (2004).
- 2286 [158] K. Sato, Atmospheric Neutrino_Reviews on neutrino fluxes (low E atm nu),
2287 2022.
- 2288 [159] Y. Hayato and L. Pickering, The European Physical Journal Special Topics **230**,
2289 4469 (2021).
- 2290 [160] Y. Hayato, Acta Physica Polonica B **40** (2009).
- 2291 [161] C. L. Smith, Physics Reports **3**, 261 (1972),
2292 <http://www.sciencedirect.com/science/article/pii/0370157372900105>.
- 2293 [162] O. Benhar, A. Fabrocini, and S. Fantoni, Nuclear Physics A **497**, 423 (1989).
- 2294 [163] R. Bradford, A. Bodek, H. Budd, and J. Arrington, Nuclear Physics B - Proceedings Supplements **159**, 127 (2006),
2295 <http://www.sciencedirect.com/science/article/pii/S0920563206005184>,
2296 Proceedings of the 4th International Workshop on Neutrino-Nucleus Interac-
2297 tions in the Few-GeV Region.
- 2298 [164] A. A. Aguilar-Arevalo *et al.*, Physical Review D **81** (2010).
- 2299 [165] R. Gran, J. Nieves, F. Sanchez, and M. J. V. Vacas, Phys. Rev. D **88**, 113007 (2013),
2300 <https://link.aps.org/doi/10.1103/PhysRevD.88.113007>.
- 2301 [166] C. Berger and L. M. Sehgal, Phys. Rev. D **76**, 113004 (2007).

- 2303 [167] C. Berger and L. M. Sehgal, Phys. Rev. D **79**, 053003 (2009),
2304 <https://link.aps.org/doi/10.1103/PhysRevD.79.053003>.
- 2305 [168] T. Sjöstrand, Computer Physics Communications **82**, 74 (1994).
- 2306 [169] C. Bronner and M. Hartz, Tuning of the Charged Hadrons Multiplicities for Deep
2307 Inelastic Interactions in NEUT, in *Proceedings of the 10th International Workshop on*
2308 *Neutrino-Nucleus Interactions in Few-GeV Region (NuInt15)*, Journal of the Physical
2309 Society of Japan, 2016.
- 2310 [170] M. Glück, E. Reya, and A. Vogt, The European Physical Journal C **5**, 461 (1998).
- 2311 [171] A. Bodek and U.-k. Yang, Axial and Vector Structure Functions for Electron- and
2312 Neutrino- Nucleon Scattering Cross Sections at all Q^2 using Effective Leading
2313 order Parton Distribution Functions, 2010.
- 2314 [172] A. Bodek and U.-K. Yang, (2010).
- 2315 [173] S. Gollapinni, (2016).
- 2316 [174] E. S. P. Guerra *et al.*, Phys. Rev. D **99**, 052007 (2019).
- 2317 [175] GEANT4, S. Agostinelli *et al.*, Nucl. Instrum. Meth. **A506**, 250 (2003).
- 2318 [176] R. Brun, F. Bruyant, M. Maire, A. C. McPherson, and P. Zanarini, (1987).
- 2319 [177] K. Abe *et al.*, Physical Review Letters **121** (2018).
- 2320 [178] K. Abe *et al.*, Physical Review D **91** (2015).
- 2321 [179] R. Patterson *et al.*, Nuclear Instruments and Methods in Physics Research Section
2322 A: Accelerators, Spectrometers, Detectors and Associated Equipment **608**, 206
2323 (2009).
- 2324 [180] e. a. S. Berkman, T2K Technical Note **146** (2013).
- 2325 [181] e. a. A. Himmel, T2K Technical Note **219** (2015).
- 2326 [182] F. a. James, (1998), CERN Program Library Long Writeups.
- 2327 [183] e. a. D. Barrow, T2K Technical Note **326** (2020).
- 2328 [184] A. Maghrabi, A. Aldosari, and M. Almutairi, Advances in Space Research **68**,
2329 2941 (2021).

- 2330 [185] Super-Kamiokande Collaboration, K. Abe *et al.*, Phys. Rev. D **97**, 072001 (2018),
2331 <https://link.aps.org/doi/10.1103/PhysRevD.97.072001>.
- 2332 [186] Particle Data Group, J. Beringer *et al.*, Phys. Rev. D **86**, 010001 (2012).
- 2333 [187] Y. N. and, Journal of Physics: Conference Series **888**, 012191 (2017).
- 2334 [188] M. Jiang, *Study of the neutrino mass hierarchy with the atmospheric neutrino data*
2335 *collected in Super-Kamiokande IV*, PhD thesis, Kyoto University, 2019.
- 2336 [189] S. N. K. Iyogi and Y. Obayashi., T2K Technical Note **027** (2011).
- 2337 [190] e. a. Tomislav Vladisavljevic, T2K Technical Note **354** (2020).
- 2338 [191] G. Ambrosini *et al.*, Phys. Lett. B **420**, 225 (1998).
- 2339 [192] R. Wendell, *Three Flavor Oscillation Analysis of Atmospheric Neutrinos in Super-*
2340 *Kamiokande*, PhD thesis, University of North Carolina, 2008.
- 2341 [193] A. M. Dziewonski and D. L. Anderson, Phys. Earth Planet. Inter. **25**, 297 (1981).
- 2342 [194] e. a. D. Barrow, T2K Technical Note **425** (2022).
- 2343 [195] R. G. Calland, A. C. Kaboth, and D. Payne, **9**, P04016 (2014).
- 2344 [196] R. Wendell, <http://www.phy.duke.edu/raw22/public/Prob3++/>.
- 2345 [197] F. Kallenborn, C. Hundt, S. Böser, and B. Schmidt, Computer Physics Communi-
2346 *cations* **234**, 235 (2019).
- 2347 [198] L. Warsame, MaCh3 Analysis Progress.
- 2348 [199] S. Bourret, J. A. B. Coelho, and V. V. E. and, Journal of Physics: Conference Series
2349 **888**, 012114 (2017).
- 2350 [200] C. Rott, A. Taketa, and D. Bose, Scientific Reports **5** (2015).
- 2351 [201] K. Hagiwara, N. Okamura, and K. ichi Senda, Journal of High Energy Physics
2352 **2011** (2011).
- 2353 [202] D. Typinski, Earth Gravity, <http://www.typnet.net/Essays/EarthGravGraphics/EarthGrav.pdf>, Accessed: 24-06-2022.
2354

²³⁵⁵ List of Figures

²³⁵⁶	2.1	The cross-section of neutrinos from various natural and man-made sources as a function of neutrino energy. Taken from [25]	11
²³⁵⁷			
²³⁵⁸	2.2	The solar neutrino flux as a function of neutrino energy for various fusion reactions and decay chains as predicted by the Standard Solar Model. Taken from [26].	12
²³⁵⁹			
²³⁶⁰			
²³⁶¹	2.3	Left panel: The atmospheric neutrino flux for different neutrino flavours as a function of neutrino energy as predicted by the 2007 Honda model (“This work”) [43], the 2004 Honda model (“HKKM04”) [44], the Bartol model [42] and the FLUKA model [46]. Right panel: The ratio of the muon to electron neutrino flux as predicted by all the quoted models. Both figures taken from [43].	14
²³⁶²			
²³⁶³			
²³⁶⁴			
²³⁶⁵			
²³⁶⁶			
²³⁶⁷	2.4	A diagram illustrating the definition of zenith angle as used in the Super Kamiokande experiment [47].	15
²³⁶⁸			
²³⁶⁹	2.5	Prediction of $\nu_e, \bar{\nu}_e, \nu_\mu, \bar{\nu}_\mu$ fluxes as a function of zenith angle as calculated by the HKKM model [45]. The left, middle and right panels represent three values of neutrino energy, 0.32GeV, 1.0GeV and 3.2GeV respectively. Predictions for other models including Bartol [42], Honda [43] and FLUKA [46] are given in [47].	15
²³⁷⁰			
²³⁷¹			
²³⁷²			
²³⁷³			
²³⁷⁴	2.6	Constraints on the atmospheric oscillation parameters, $\sin^2(\theta_{23})$ and Δm_{23}^2 , from atmospheric and long baseline experiments: SK [52], T2K [53], NO ν A [54], IceCube [55] and MINOS [56]. Figure taken from [57].	16
²³⁷⁵			
²³⁷⁶			
²³⁷⁷	2.7	Reactor electron antineutrino fluxes for ^{235}U (Black), ^{238}U (Green), ^{239}Pu (Purple), and ^{241}Pu (Orange) isotopes. The inverse β -decay cross-section (Blue) and corresponding measurable neutrino spectrum (Red) are also given. Top panel: Schematic of Inverse β -decay interaction including the eventual capture of the emitted neutron. This capture emits a γ -ray which provides a second signal of the event. Taken from [69].	19
²³⁷⁸			
²³⁷⁹			
²³⁸⁰			
²³⁸¹			
²³⁸²			
²³⁸³	3.1	A schematic diagram of the Super-Kamiokande Detector. Taken from [88].	26

2384 3.2	The location of “standard PMTs” (red) inside the SK detector. Taken 2385 from [86].	30
2386 3.3	Schematic view of the data flow through the data acquisition and online 2387 system. Taken from [102].	34
2388 3.4	The cross-section view of the Tokai to Kamioka experiment illustrating 2389 the beam generation facility at J-PARC, the near detector situated at 2390 a baseline of 280m and the Super Kamiokande far detector situated 2391 295km from the beam target.	37
2392 3.5	The near detector suite for the T2K experiment showing the ND280 and 2393 INGRID detectors. The distance between the detectors and the beam 2394 target is 280m.	38
2395 3.6	Top panel: Bird’s eye view of the most relevant part of primary and sec- 2396 ondary beamline used within the T2K experiment. The primary beam- 2397 line is the main-ring proton synchrotron, kicker magnet, and graphite 2398 target. The secondary beamline consists of the three focusing horns, 2399 decay volume, and beam dump. Figure taken from [118]. Bottom panel: 2400 The side-view of the secondary beamline including the focusing horns, 2401 beam dump and neutrino detectors. Figure taken from [119].	39
2402 3.7	The Monte Carlo prediction of the energy spectrum for each flavour of 2403 neutrino (ν_e , $\bar{\nu}_e$, ν_μ and $\bar{\nu}_\mu$) in the neutrino dominated beam FHC mode 2404 (Left) and antineutrino dominated beam RHC mode (Right) expected at 2405 SK. Taken from [120].	41
2406 3.8	Top panel: T2K muon neutrino disappearance probability as a function 2407 of neutrino energy. Middle panel: T2K electron neutrino appearance 2408 probability as a function of neutrino energy. Bottom panel: The neutrino 2409 flux distribution for three different off-axis angles (Arbitrary units) as a 2410 function of neutrino energy.	42
2411 3.9	The components of the ND280 detector. The neutrino beam travels from 2412 left to right. Taken from [118].	43
2413 3.10	Comparison of data to Monte Carlo prediction of integrated deposited 2414 energy as a function of track length for particles that stopped in FGD1. 2415 Taken from [123].	45

2416	3.11 Schematic design of a Time Projection Chamber detector. Taken from [124].	46
2417	3.12 The distribution of energy loss as a function of reconstructed momentum for charged particles passing through the TPC, comparing data to Monte Carlo prediction. Taken from [124].	47
2418		
2419		
2420	3.13 A schematic of the P0D side-view. Taken from [125].	48
2421	3.14 Left panel: The Interactive Neutrino GRID on-axis Detector. 14 modules are arranged in a cross-shape configuration, with the center modules being directly aligned with the on-axis beam. Right panel: The layout of a single module of the INGRID detector. Both figures are recreated from [118].	51
2422		
2423		
2424		
2425		
2426	4.1 Example of using Monte Carlo techniques to find the area under the blue line. The gradient and intercept of the line are 0.4 and 1.0 respectively. The area found to be under the curve using one thousand samples is 29.9 units.	56
2427		
2428		
2429		
2430	4.2 The area under a line of gradient 0.4 and intercept 1.0 for the range $0 \leq x \leq 10$ as calculated using Monte Carlo techniques as a function of the number of samples used in each repetition. The analytical solution to the area is 30 units as given by the red line.	57
2431		
2432		
2433		
2434	4.3 Three MCMC chains, each with a stationary distribution equal to a Gaussian centered at 0 and width 1 (As indicated by the black dotted lines). All of the chains use a Gaussian proposal function but have different widths (or ‘step size σ ’). The top panel has $\sigma = 0.1$, middle panel has $\sigma = 0.5$ and the bottom panel has $\sigma = 5.0$.	62
2435		
2436		
2437		
2438		
2439	4.4 The log-likelihood from the fit detailed in DB: Link to AsimovA Sensitivity Section as a function of the number of steps accumulated in each fit. Many independent MCMC chains were run in parallel and overlaid on this plot. The red line indicates the 1×10^5 step burn-in period after which the log-likelihood becomes stable.	63
2440		
2441		
2442		
2443		

2444	4.5 Left: The two dimensional probability distribution for two correlated parameters x and y . The red distribution shows the two dimensional probability distribution when $0 \leq x \leq 5$. Right: The marginalised probability distribution for the y parameter found when requiring the x to be bound between $-5 \leq x \leq 5$ and $0 \leq x \leq 5$ for the black and red distribution, respectively.	66
2450	5.1 The NEUT prediction of the ν_μ -H ₂ O cross-section overlaid on the T2K ν_μ flux. The charged current (black, solid) and neutral current (black, dashed) inclusive, charged current quasi-elastic (blue, solid), charged current 2p2h (blue, dashed), charged current single pion production (pink), and charged current multi- π and DIS (Purple) cross-sections are illustrated. Figure taken from [159].	74
2456	5.2 Illustration of the various processes which a pion can undergo before exiting the nucleus. Taken from [173].	75
2458	5.3 Event displays from Super Kamiokande illustrating the “crisp” ring from a muon and the typically “fuzzier” electron ring. Each pixel represents a PMT and the color scheme denotes the accumulated charge deposited on that PMT. Figures taken from [181].	78
2462	5.4 The electron/muon PID separation parameter for all sub-GeV single-ring events in SK-IV. The charged current (CC) component is broken down in four flavours of neutrino (ν_μ , $\bar{\nu}_\mu$, ν_e and $\bar{\nu}_e$). Events with positive values of the parameter are determined to be electron-like. . .	82
2466	5.5 The variation of the measured dark rate as a function of date, broken down by PMT type. The SK-IV and SK-V periods span September 2008 to May 2018 and January 2019 to July 2020, respectively. The break in measurement in 2018 corresponds to the period of tank repair and refurbishment. Figure adapted from [183].	84
2471	5.6 Comparison of the measured raw charge deposited per event from the stopping muon data samples between SK-IV (Blue) and SK-V (Red), split by the primary muon subevent and the associated decay electron subevent.	85

2475 5.7	The distribution of the reconstructed momentum from the muon ring divided by the distance between the reconstructed muon and decay electron vertices as found in the stopping muon data sets of SK-IV (Black) and SK-IV (Red). Only events with one tagged decay electron are considered. A Gaussian fit is considered in the range [2.0, 2.4] MeV/cm and illustrated as the solid curve.	86
2481 5.8	The χ^2 difference between the SK-IV and SK-V reconstructed muon momentum divided by range when the SK-V is modified by the scaling parameter α . Both additive (Blue) and multiplicative (Black) scaling factors have been considered. In practice, the additive scaling factor actually uses the value of $(\alpha - 1.0)$ but is illustrated like this so the results can be shown on the same axis range.	87
2487 5.9	A depiction of the topology patterns for fully-contained (FC), partially- contained (PC) and up-going muon (Up- μ) samples included in this analysis.	88
2490 5.10	The predicted neutrino flux of the fully contained (FC) sub-GeV and multi-GeV, partially contained (PC), and upward-going muon (Up- μ) events. The prediction is broken down by the $\nu_x \rightarrow \nu_e$ prediction (top left), $\nu_x \rightarrow \nu_\mu$ prediction (top right) and $\nu_x \rightarrow \nu_\tau$ prediction (bottom). All systematic dials are set to their nominal values and the Asimov A oscillation parameters are assumed.	90
2496 6.1	The total uncertainty evaluated on the near detector ν_μ flux prediction constrained by the replica-target data, illustrated as a function of neutrino energy. The solid(dashed) line indicates the uncertainty used within this analysis(the T2K 2018 analysis). The solid histogram indicates the neutrino flux as a function of energy. Figure taken from [190].	93
2501 7.1	The density of the Earth given as a function of the radius, as given by the PREM model (Black), and the constant density four-layer approximation (Blue), as used in the official SK-only analysis.	100

2504	7.2	An “oscillogram” that depicts the $P(\nu_\mu \rightarrow \nu_e)$ oscillation probability as 2505 a function of neutrino energy and cosine of the zenith angle. The zenith 2506 angle is defined such that $\cos(\theta_Z) = 1.0$ represents neutrinos that travel 2507 from directly above the detector. The four-layer constant density PREM 2508 model approximation is used and Asimov A oscillation parameters are 2509 assumed (Table 2.2).	100
2510	7.3	The effect of δ_{CP} for atmospheric neutrinos given in terms of the 2511 neutrino energy and zenith angle. This oscillogram compares the 2512 $P(\nu_\mu \rightarrow \nu_e)$ oscillation probability for a CP conserving ($\delta_{CP} = 0.0$) 2513 and a CP violating ($\delta_{CP} = -1.601$) value taken from the Asimov A 2514 parameter set. The other oscillation parameters assume the Asimov A 2515 oscillation parameter set given in Table 2.2.	102
2516	7.4	An illustration of the matter-induced effects on the oscillation probabil- 2517 ity, given as a function of neutrino energy and zenith angle. The top row 2518 of panels gives the $P(\nu_e \rightarrow \nu_e)$ oscillation probability and the bottom 2519 row illustrates the $P(\bar{\nu}_e \rightarrow \bar{\nu}_e)$ oscillation probability. The left column 2520 highlights the oscillation probability in a vacuum, whereas the middle 2521 and right column represents the oscillation probabilities when the four- 2522 layer fixed density PREM model is assumed. All oscillation probabilities 2523 assume the “Asimov A” set given in Table 2.2, but importantly, the right 2524 column sets an inverted mass hierarchy. The “matter resonance” effects 2525 at $E_\nu \sim 5\text{GeV}$ can be seen in the $P(\nu_e \rightarrow \nu_e)$ for normal mass hierarchy 2526 and $P(\bar{\nu}_e \rightarrow \bar{\nu}_e)$ for inverted hierarchy.	103
2527	7.5	The oscillation probability for beam neutrino events given as a function 2528 of neutrino energy. All oscillation parameters assume the “Asimov A” 2529 set given in Table 2.2 unless otherwise stated. Each panel represents a 2530 change in one of the oscillation parameters whilst keeping the remaining 2531 parameters fixed.	104
2532	7.6	The number of electron-like events in the FHC and RHC operating 2533 mode of the beam, as a function of the oscillation probabilities. Both 2534 normal hierarchy (Solid)) and inverse hierarchy (Dashed) values of 2535 Δm_{23}^2 are given.	105

2536	7.7	The oscillation probability $P(\nu_\mu \rightarrow \nu_e)$, given as a function of neutrino energy and zenith angle, which highlights an example of the “fast” oscillations in the sub-GeV upgoing region.	107
2537			
2538			
2539	7.8	Illustration of the averaging procedure for $N = 2$. The oscillation probabilities calculated on the finer left binning are averaged to obtain the oscillation probabilities in the coarser right binning. These averaged oscillation probabilities with the coarser binning are then applied to each event during the fit.	109
2540			
2541			
2542			
2543			
2544	7.9	Event rate of the SubGeV_elike_0dcy sample as a function of the number of sub-divisions per coarse bin. Each subplot represents the event rate of the sample at a different oscillation parameter set thrown from the PDG priors detailed in Table 2.1. The red line in each subplot represents the mean of the event rate over the different values of sub-divisions for that particular oscillation parameter throw.	111
2545			
2546			
2547			
2548			
2549			
2550	7.10	Variance of event rate for each atmospheric sample as a function of the number of sub-divisions per coarse bin. The solid red line indicates the 0.1% threshold and the dashed red line indicates the variance at a sub-division $N = 10$	112
2551			
2552			
2553			
2554	7.11	Variance of sample likelihood, when compared to ‘Asimov data’ set at Asimov A, for each atmospheric sample as a function of the number of sub-divisions per coarse bin. The solid red line indicates the 0.1% threshold and the dashed red line is a graphical indication of the variance at a sub-division $N = 10$	113
2555			
2556			
2557			
2558			
2559	7.12	The oscillation probability, $P(\nu_\mu \rightarrow \nu_e)$ (top row) and $P(\nu_e \rightarrow \nu_e)$ (bottom row), given as a function of neutrino energy and zenith angle. The left column gives the “fine” binning used to calculate the oscillation probabilities and the right column illustrates the “coarse” binning used to reweight the Monte Carlo events. The fine binning choice is given with $N = 10$, which was determined to be below the threshold from Figure 7.10 and Figure 7.11.	114
2560			
2561			
2562			
2563			
2564			
2565			

2566	7.13 The calculation time taken to both calculate the oscillation probabilities 2567 and fill the “coarse” oscillograms, following the technique given in 2568 section 7.2, for the CUDAProb3 and ProbGPU (Red) calculation engines. 2569 CUDAProb3 has both a GPU (Blue) and CPU (Black) implementation, 2570 where the CPU implementation is multithreaded. Therefore, 8-threads 2571 (solid) and 40-threads (dashed) configurations have been tested. Prob3, 2572 which is a CPU single-thread implementation has a mean step time of 2573 1.142s.	115
2574	7.14 The oscillation probability, $P(\nu_\mu \rightarrow \nu_e)$ (top row) and $P(\nu_e \rightarrow \nu_e)$ (bot- 2575 tom row), given as a function of neutrino energy and zenith angle. The 2576 left column gives probabilities where the constant $Z/A = 0.5$ approx- 2577 imation which is used in the official SK-only analysis. The middle 2578 column gives the probabilities where $Z/A = [0.468, 0.498]$ values are 2579 used, as given in Table 7.1. The right column illustrates the difference 2580 in oscillation probability between the two different techniques.	117
2581	7.15 The density of the Earth given as a function of the radius, as given by 2582 the PREM model (Black), the constant density four-layer approxima- 2583 tion (Blue), as used in the official SK-only analysis, and the quadratic 2584 approximation of the PREM model (Red).	118
2585	7.16 The oscillation probability, $P(\nu_\mu \rightarrow \nu_e)$ (top row) and $P(\nu_e \rightarrow \nu_e)$ (bot- 2586 tom row), given as a function of neutrino energy and zenith angle. The 2587 left column gives probabilities where the four-layer constant density ap- 2588 proximation is used. The middle column gives the probabilities where 2589 the density is integrated over the trajectory, using the quadratic PREM 2590 approximation, for each $\cos(\theta_Z)$ is used. The right column illustrates the 2591 difference in oscillation probability between the two different techniques.	120
2592	7.17 The oscillation probability, $P(\nu_\mu \rightarrow \nu_e)$ (top row) and $P(\nu_e \rightarrow \nu_e)$ (bot- 2593 tom row), given as a function of neutrino energy and zenith angle. The 2594 left column gives probabilities where a fixed production height of 25km 2595 is used. The middle column gives the probabilities where the produc- 2596 tion height is analytically averaged. The right column illustrates the 2597 difference in oscillation probability between the two different techniques.	124

List of Tables

2599	2.1	The 2018 Particle Data Group constraints of the oscillation parameters taken from [81]. The value of Δm_{23}^2 is given for both normal hierarchy (N.H.) and inverted hierarchy (I.H.) and $\sin^2(\theta_{23})$ is broken down by whether its value is below (Q1) or above (Q2) 0.5.	21
2600			
2601			
2602			
2603	2.2	Reference values of the neutrino oscillation parameters for two different oscillation parameter sets.	23
2604			
2605	3.1	The various SK periods and respective live-time. The SK-VI live-time is calculated until 1 st April 2022. SK-VII started during the writing of this thesis.	25
2606			
2607			
2608	3.2	The trigger thresholds and extended time windows saved around an event which were utilised throughout the SK-IV period. The exact thresholds can change and the values listed here represent the thresholds at the start and end of the SK-IV period.	34
2609			
2610			
2611			
2612	3.3	The threshold momentum and energy for a particle to generate Cherenkov light in ultrapure water, as calculated in Equation 3.2 in ultrapure water which has refractive index $n = 1.33$	36
2613			
2614			
2615	4.1	Jeffreys scale for strength of preference for two models A and B as a function of the calculated Bayes factor ($B_{AB} = B(A/B)$) between the two models [140]. The original scale is given in terms of $\log_{10}(B(A/B))$ but converted to linear scale for easy comparison throughout this thesis.	68
2616			
2617			
2618			
2619	6.1	The neutrino energy binning for the different neutrino flavours. “Right” sign indicates neutrinos in the FHC beam and antineutrinos in the RHC beam mode. “Wrong” sign indicates antineutrinos in the FHC beam and neutrinos in the RHC beam mode. The binning of the detector response is identical for the FHC and RHC modes as well as at ND280 and SK.	94
2620			
2621			
2622			
2623			
2624			

2625	7.1	Description of the four layers of the Earth invoked within the constant density approximation of the PREM model [193].	99
2626	7.2	The quadratic polynomial fits to the PREM model for four assumed layers of the PREM model. The fit to calculate the coefficients is given in [194], where $x = R/R_{Earth}$	119
2627			
2628			
2629			